Winter 2002

Resonant wave-ion interactions in the heliosphere: I. Interplanetary traveling shocks, II. Ion heating and acceleration in the extended corona

Bruce Edward Gordon
University of New Hampshire, Durham

INFORMATION TO USERS

This manuscript has been reproduced from the microfilm master. UMI films the text directly from the original or copy submitted. Thus, some thesis and dissertation copies are in typewriter face, while others may be from any type of computer printer.

The quality of this reproduction is dependent upon the quality of the copy submitted. Broken or indistinct print, colored or poor quality illustrations and photographs, print bleedthrough, substandard margins, and improper alignment can adversely affect reproduction.

In the unlikely event that the author did not send UMI a complete manuscript and there are missing pages, these will be noted. Also, if unauthorized copyright material had to be removed, a note will indicate the deletion.

Oversize materials (e.g., maps, drawings, charts) are reproduced by sectioning the original, beginning at the upper left-hand corner and continuing from left to right in equal sections with small overlaps.

ProQuest Information and Learning
300 North Zeeb Road, Ann Arbor, MI 48106-1346 USA
800-521-0600

RESONANT WAVE-ION INTERACTIONS IN THE HELIOSPHERE: I. INTERPLANETARY TRAVELING SHOCKS II. ION HEATING AND ACCELERATION IN THE EXTENDED CORONA

BY

BRUCE E. GORDON

B.S., Physics, UMASS-Lowell, 1979

M.S., Physics, University of New Hampshire, 1981

DISSERTATION

Submitted to the University of New Hampshire

in Partial Fulfillment of

the Requirements for the Degree of

Doctor of Philosophy

in

Physics

December, 2002

ProQuest Information and Learning Company
300 North Zeeb Road
P.O. Box 1346
Ann Arbor, MI 48106-1346

This dissertation has been examined and approved.

Martin A. Lee

Dissertation Director, Dr. Martin A. Lee, Professor of Physics

Joseph V. Hollweg

Dr. Joseph V. Hollweg, Professor of Physics

Dr. Philip A. Isenberg, Research Professor of Physics

James M. Ryan

Dr. James Ryan, Professor of Physics

Harvey Shepard

Dr. Harvey K. Shepard, Professor of Physics

October 25 2002

Date

ACKNOWLEDGMENTS

I want to thank my advisor, Dr. Martin A. Lee, for his support, guidance, unwavering insistence on producing quality work, and patience with me for these many years. I want to thank the other members of my thesis committee (Dr. Joseph Hollweg, Dr. Phillip Isenberg, Dr. James Ryan, and Dr. Harvey Shepard) for their time spent helping me, and reading this dissertation. I also want to thank Dr. Terry Forbes for help with Mathematica and assorted computer-related matters. I thank my colleagues at the New Hampshire Community Technical College at Claremont for their support. Many of my colleagues listened patiently while I whined about my frustrations and the difficulty of simultaneously working at the college and doing my research. Last, but definitely not least, I thank my wife Andrea and two children, Grant and Rachel, for their constant support and for never losing faith that I would eventually finish.

The work resulting in Part I was supported by the NASA Sun-Earth Connections Theory Program grant NAG5-1479, NASA grant NAS5-30302, and NSF grant ATM-96333666. Part I was published in the *Journal of Geophysical Research, Space Physics*, Volume 104, pp. 28263 - 28277, December 1, 1999.

The work resulting in Part II was supported by NSF grant ATM-0091527.

FOREWORD

This dissertation is composed of two parts. In part one, we consider diffusive shock acceleration of protons and the associated generation of hydromagnetic waves at planar stationary shocks. The second part is an effort to provide insights into the preferential resonant heating and differential streaming speeds of ions in the extended corona.

There are obvious differences between these two problems, but there are fundamental physical principles that link them. The resonant ion ion-cyclotron wave interaction, which causes ions to diffuse in pitch-angle in the wave frame, is the primary physical mechanism common to both parts. Ions can diffuse back and forth across a shock many times and for each round-trip traversal of the shock they gain energy. Ions are scattered in pitch angle upstream and downstream of a shock front due to interactions with waves in the solar wind, possibly modified by the ions and magnetic turbulence associated with the shock. The wave energy can grow at the expense of the ion energy, while ions gain energy due to multiple encounters with the shock. In part two, we assume that wave energy at the cyclotron resonant frequencies is always available and that ions only gain energy from the waves. Resonant ions scatter to uniformity in pitch-angle while conserving kinetic energy in the frame moving with the waves.

In both parts, the ion distribution function is calculated from an energetic particle transport equation, although the forms of the transport equation used in each part are significantly different, reflecting the different physical phenomena. In Part I, the wave

intensity is determined from a wave kinetic equation; the ion distribution function and wave intensity are calculated self-consistently. In Part II, the cold, electron-proton plasma dispersion relation is used to determine the maximum speed of an ion species resonant with anti-sunward propagating, left hand circularly polarized waves; whereas, in part I we assume ions interact with parallel propagating waves traveling in both directions. In shock acceleration, ions are energized by multiple traversals of a shock, possibly mirroring from gradients in the magnetic field in the vicinity of the shock front. In contrast, in Part II, ion radial acceleration is achieved through magnetic mirroring of the transversely-heated ions in the radially diverging solar magnetic field.

TABLE OF CONTENTS

LIST OF FIGURES

ABSTRACT

RESONANT WAVE-ION INTERACTIONS IN THE HELIOSPHERE:

I. INTERPLANETARY TRAVELING SHOCKS

II. ION HEATING AND ACCELERATION IN THE EXTENDED CORONA

By

Bruce E. Gordon

University of New Hampshire, December, 2002

In Part I we present a revised version of the self-consistent theory of ion diffusive shock acceleration and associated generation of hydromagnetic waves at a planar stationary shock. Coupled wave kinetic and energetic particle transport equations are solved numerically and compared with an analytical approximation similar to that derived by *Lee* [1982, 1983]. The analytical approximation provides an accurate representation of both the proton distribution and the wave intensity. Excellent agreement between the predicted wave magnetic power spectral density adjacent to the shock as a function of frequency and the wave spectrum measured by ISEE 3 at the November 11 - 12, 1978, interplanetary traveling shock is achieved. A comparison is also made between the predicted total wave energy density and that observed upstream of Earth's bow shock by the AMPTE/IRM satellite for a statistical study of approximately 400 near-to-nose events from late 1984 and 1985. The correlation between the observed wave power and the prediction is very good with a correlation coefficient of 0.92. However, the average observed wave magnetic energy density is approximately 63% of that predicted, suggesting possible wave dissipation, which is not included in the theory.

In Part II we present a semi-analytical solution of the gyrophase-averaged ion transport equation for ion distribution functions in the extended corona. We adopt the essential features of the kinetic shell model [*Isenberg*, 1997; 2001a, b, c; *Isenberg et al.*, 2000, 2001] and thus, we describe the ion distribution as comprised of cyclotron-resonant and nonresonant parts. We include gravity, the ambipolar electric field, adiabatic deceleration, and magnetic mirroring, but keep the solar wind and wave phase speeds constant. The cold, electron-proton plasma dispersion relation is used to determine the wave-ion resonance condition. The actual, analytical forms of the ion distribution functions obtained are clearly not Maxwellian or bi-Maxwellian. Our solutions describe some of the non-thermal phenomena frequently observed in the extended corona: anisotropic temperature distributions, and differential streaming between protons and minor ion species. However, we fail to model the observed radial temperature dependence of protons and O^{5+} ions.

PART I

COUPLED HYDROMAGNETIC WAVE EXCITATION AND ION ACCELERATION AT INTERPLANETARY TRAVELING SHOCKS AND EARTH'S BOW SHOCK REVISITED

CHAPTER 1.1

INTRODUCTION

We revisit the phenomenon of diffusive shock acceleration of solar wind ions and the accompanying growth of hydromagnetic waves. Ions can diffuse back and forth across a shock many times, and for each round-trip traversal of the shock they gain energy. Ions are pitch-angle scattered upstream and downstream of the shock front due to interactions with waves in the solar wind, possibly modified by the ions themselves, and magnetic turbulence associated with the shock. The ions couple to the waves via ion-cyclotron resonance. Scattering of the ions by the waves provides the diffusion mechanism. The wave energy can grow at the expense of the ion energy while ions gain energy due to multiple encounters with the shock.

The evidence for high energy ions resulting from interactions with interplanetary traveling shocks and planetary bow shocks has its origins in the 60's. Observations made by the Vela satellite [*Asbridge et al.*, 1968] showed that a small fraction of the incoming solar wind ions were reflected by Earth's bow shock with an energy increase of about a factor of five. An analysis by *Sonnerup* [1969] based on ion reflection from the shock front predicted an increase in energy consistent with these observations. Using ISEE 1 data, *Bame et al.* [1980] showed that the solar wind is slowed and deflected away from Earth's bow shock. Their observations suggested that the solar wind deceleration is the

result of momentum transfer from the reflected bow shock ions to the solar wind via an interaction with long period (tens of seconds) waves.

Armstrong et al. [1970] examined several interplanetary shock events, and paid particular attention to the event of 20 February 1968. Their results showed a close temporal correlation between the enhancement of ion fluxes and the passing of a shock front. Acceleration of protons by repeated crossings of the front of a nearly perpendicular shock was deduced by *Sarris and Van Allen* [1974] from Explorer 33 and 35 data. They observed energization of protons up to about 1 MeV after encountering the shock. Ion distribution functions were determined by *Gosling et al.* [1981] based on ISEE 2 and 3 data. They found a power law distribution in velocity for ion energies up to about 40 keV and an exponential dependence on velocity for ion energies greater than about 200 keV. *Scholer et al.* [1983] examined ISEE 3 data for three interplanetary shocks and concluded that multiple ion-shock encounters are required to account for the observations. They also deduced a power law phase-space distribution function with a spectral index of about 4 for the 11-12 November 1978 shock. *Tan et al.* [1986] used IMP 8 and ISEE 3 data to show that ions with energies of a few keV are the seed population for the 40 keV energetic ions, but that higher energy ions, presumably from flares or coronal mass ejections, are required to seed the ions with energies greater than 200 keV.

Concurrently with the observations of energetic ions, enhanced hydromagnetic waves were observed upstream of Earth's bow shock. *Greenstadt et al.* [1968], using Vela 3A

data, reported magnetic oscillations with amplitudes up to about 12 nT (1 nT = 10^{-9} Tesla) and periods of between 4 and 30 seconds. Other early evidence for upstream waves came from *Fairfield* [1969] who, using Explorer 34 data, reported waves with amplitudes comparable with the background magnetic field of a few nT and periods in the 20 to 100 s range. *Fairfield* [1969] also showed that the wave amplitude decreased by only a factor of about two from the bow shock to a distance upstream of about 15 R_E (R_E = Earth Radius ≈ 6400km). ISEE 3 data provided a good correlation between the existence of 35 keV to 1600 keV upstream ions and 30 s period upstream waves [*Sanderson et al.*, 1983]. They observed that in the absence of waves the ions had beam-like anisotropies, but with waves present the pitch-angle distributions broadened. Wave growth was accompanied by progressive broadening of the ion pitch-angle distribution. Their observations of upstream ions with pitch angles near 90° is evidence that significant pitch-angle scattering is taking place, since ions with pitch angles near 90° do not propagate upstream. *Hoppe et al.* [1981] observed that the upstream waves often steepen and can form shocklets [*Hada et al.*, 1987], which often break into whistler mode wave packets.

A survey of interplanetary shocks observed by ISEE 3 from August 1978 to March 1980 was made by *Tsurutani et al.* [1983]. They found that enhanced wave intensities were detected for almost all of the interplanetary shocks examined. Long period waves, around 20 s, were found up to 10R_E from the shock. These waves propagated within a cone of about 15° around the ambient magnetic field, substantiating our assumption in Chapter 1.2 of nearly parallel (or anti-parallel) propagation. *Kennel et al.* [1986] also

reported nearly parallel wave propagation for the 11-12 November 1978 shock event. *Kennel et al.* [1986] deduced that these upstream waves must have been produced by 1-10 keV upstream ions which were observed flowing away from the shock. These ion energies and wave frequencies are consistent with those required by ion-cyclotron resonance.

In an early theoretical model of diffusive shock acceleration, *Fisk* [1971] applied the energetic particle transport equation [*Parker*, 1965] to shock-associated ion enhancements by assuming a power-law dependence in velocity. He suggested that low energy ions are scattered to higher energies by magnetic irregularities converging at the shock front. *Scholer and Morfill* [1975] used a Monte Carlo technique to model the propagation of solar flare ions including the effect of an interplanetary shock. Theoretical work by *Axford et al.* [1977], *Krymskii* [1977], *Blandford and Ostriker* [1978], and *Bell* [1978] showed that multiple traversals of a shock by ions lead naturally to ion distributions with a power-law dependence on momentum. A comprehensive review of diffusive shock acceleration can be found in *Jones and Ellison* [1991].

Early theoretical work by *Barnes* [1970] showed that streaming energized ions generate waves through ion-cyclotron resonance and that the instability is "quenched by pitch-angle scattering." *Bell* [1978] developed a self-consistent description of ion acceleration and wave generation for the case of a negligible background wave spectrum. *Lee* [1982, 1983], following the work of *Skilling* [1975] and *Bell* [1978], produced a self-consistent theory to describe the diffusive acceleration of ions and the accompanying

amplification of hydromagnetic waves at the Earth's bow shock and at interplanetary traveling shocks, respectively. Quasi-linear theory was employed to calculate the coupled ion acceleration and wave growth. A finite shock size with a lateral free escape boundary was assumed for the bow shock, but an infinite planar shock was used to model the traveling shock. The theory, incorporating a finite connection time to the shock, was later applied to Jupiter's foreshock by *Smith and Lee* [1986].

Although the predictions of *Lee* [1982, 1983] generally agreed with observations at both Earth's bow shock and interplanetary traveling shocks, a comparison between the theory and specific observed events was not performed. However, an extensive test of *Lee's* self-consistent theory was performed by *Kennel et al.* [1986] for the interplanetary traveling shock event of 11-12 November 1978. *Kennel et al.* [1986] extracted 13 separate predictions of *Lee's* 1983 theory. For most of the predictions there was generally good agreement between the theory and the observations, but there were two exceptions. Firstly, the theory of *Lee* [1983] predicts wave enhancements with zero average helicity, but *Kennel et al.* [1986] observed waves of definite helicity. *Kennel et al.* [1986] attributed the prediction of equal growth of left and right-hand circularly polarized waves, resulting in no net helicity, to the assumption by *Lee* [1982, 1983] of a linear dependence of the anisotropic part of the distribution function on $\mu = \cos\theta$, where θ is the ion pitch angle. Secondly, the observed wave power spectrum presented by *Kennel et al.* [1986] peaks and then decreases as frequency decreases. This low-frequency behavior was not predicted by the self-consistent theory of *Lee* [1982, 1983].

In another test of the theory, *Tan et al.* [1989] compared the inferred diffusion tensor component parallel to the ambient magnetic field for several interplanetary traveling shock events to that predicted by *Lee* [1983] and found an almost one-to-one correspondence. Also, *Trattner et al.* [1994] compared observed enhanced wave energy densities upstream of Earth's bow shock with the prediction based on the energetic particle energy densities, and found a positive correlation and fair agreement. However, this result used the wave intensities predicted by *Lee* [1982] which were based on the restrictive form of the ion anisotropy.

There are four main objectives of this paper: (i) *Lee* [1982, 1983] assumed a linear dependence of the anisotropic part of the distribution function on μ, as in an earlier work by *Jokipii* [1971], in order to obtain an expression for the ion anisotropy. This assumption is not valid for arbitrary wave intensity. Here, we obtain the correct dependence of the distribution function on μ by solving the pitch-angle diffusion equation under the assumption of effective scattering. This correction changes quantitatively but not qualitatively the analytical theory of *Lee* [1982, 1983] for the wave intensity and the ion distribution function. For the planar geometry appropriate to traveling shocks, we present the revised analytical theory of *Lee*. We also show that the total wave magnetic energy density derived through quasi-linear theory agrees with the result of the fluid theory of *McKenzie and Völk* [1982]. (ii) For the planar geometry, we solve the coupled wave kinetic equation and proton transport equation numerically and compare the results with the analytical approximation. The numerical solution also depicts the higher frequency behavior of the wave intensity, inaccessible with the

analytical approximation. (iii) In Chapter 1.3 we compare the predicted magnetic power spectral density adjacent to the shock with the results of *Kennel et al.* [1986] for the 11-12 November 1978 interplanetary traveling shock. (iv) Also, in Chapter 1.3, we compare the new prediction for the enhanced wave magnetic energy densities upstream of Earth's bow shock with the observed enhancements for the statistical survey of *Trattner et al.* [1994]. In both comparisons very good agreement between theory and the observations is found. A detailed discussion is presented in Chapter 1.4.

Ion acceleration at Earth's bow shock is more complicated than at interplanetary traveling shocks where ion acceleration at a stationary planar shock is a reasonable approximation at the lower ion energies which dominate wave excitation. Ion acceleration at Earth's bow shock is affected by short connection time of magnetic field lines to the shock, ion drift across the small lateral extent of the shock, and ion diffusion across field lines to the weak flanks of the shock or to regions disconnected from the shock. These loss processes dominate the form of the energetic ion energy spectrum which is observed to be exponential in energy [*Ipavich et al.*, 1979, 1981] rather than the standard power law dependence of stationary planar shock acceleration. In addition, the unstable waves at Earth's bow shock are those propagating sunward so that these must be included with the predominantly antisunward propagating ambient waves. Also near its nose the bow shock is a strong shock, so that ion injection processes at the shock front may require a range of injection energies [*Scholer et al.*, 1992].

For these reasons we present the basic coupled theory for ion acceleration and wave excitation only for stationary planar shocks with waves propagating in the antisunward direction, which applies only to interplanetary traveling shocks and ion energies up to ~ 100 keV/nucleon. However, one interesting and important result for the wave excitation is the predicted ratio of the local enhanced wave magnetic energy density and the energetic particle energy density [*McKenzie and Völk, 1982*], which emphasizes the direct coupling of ion streaming and wave growth, and is independent of the detailed structure of the ion distribution function and ion loss mechanisms. As long as the enhanced wave spectrum dominates the ambient wave spectrum, then this result may be applied to the diffuse ions and enhanced wave intensities observed in Earth's foreshock.

CHAPTER 1.2

BASIC THEORY

1.2.1 Derivation of the Pitch-Angle Distribution Function and the Spatial Diffusion Coefficient

The theory describing the nonrelativistic energetic ion distribution function follows closely the derivation of *Lee* [1982, 1983], but incorporates the change described in the Introduction. We consider an infinite, planar shock with upstream normal in the $\hat{e}_z$ direction. In the shock frame, the z-component of the upstream solar wind velocity is $-V$. The upstream ambient magnetic field is $\mathbf{B}_0 = B_0 \hat{e}_b$, where $\hat{e}_b \bullet \hat{e}_z = \cos\psi > 0$, and B_0 may be positive or negative.

We assume that the ion phase-space distribution function in the upstream plasma frame is approximately gyrotropic and given by

$$f(t,v,l,\mu) = f_o(t,v,l) + g(t,v,l,\mu). \tag{1}$$

Here, t is time, l is arc length along $\hat{e}_b$, v is ion speed, $v\mu = \mathbf{v} \bullet \hat{e}_b$, the omnidirectional distribution function is given by

$$f_0(t,v,l) = \frac{1}{2}\int_{-1}^{1} f(t,v,l,\mu)\,d\mu, \tag{2}$$

and $g(t,v,l,\mu)$ is the non-gyrotropic part of the ion velocity distribution.

We also assume that scattering is sufficiently strong that $|g(t,v,l,\mu)| << f_0(t,v,l)$. We will address the validity of this assumption in Chapter 1.3.

The distribution function, $f(t,v,l,\mu)$, satisfies the pitch-angle diffusion equation

$$v\mu\frac{\partial f}{\partial l} = \frac{\partial}{\partial \mu}(1-\mu^2)D_{\mu\mu}\frac{\partial f}{\partial \mu}, \tag{3}$$

where we neglect $\partial f/\partial t$, since for strong scattering $|\partial f/\partial t| << |v\mu\partial f/\partial l|$. We also neglect gradients in $\mathbf{B}_0$. Assuming wave propagation parallel or antiparallel to $\mathbf{B}_0$, the pitch angle diffusion coefficient $D_{\mu\mu}$ is given by *Jokipii* [1971] and *Lee* [1971, 1982, 1983] as

$$D_{\mu\mu} = \frac{\pi q^2}{2m^2c^2|\mu|v}(1-\mu^2)I\left(\frac{\Omega}{\mu v}\right), \tag{4}$$

where $\Omega(=qB_0/mc)$ is the nonrelativistic gyrofrequency, and q and m are the ion charge and mass, respectively. In evaluating the argument of the wave intensity, $I(k)$, in equation (4), we neglect the wave frequency, ω, with respect to Ω in the cyclotron resonance condition, $\omega - \Omega - k\mu v \cong 0$. This is equivalent to neglecting the Alfvén speed, $V_A = \omega/k$, with respect to the particle speed. Energetic ion speeds are greater than the solar wind speed, which at 1 AU is about an order of magnitude larger than V_A.

The wave intensity, $I(k) = I_+(k) + I_-(k)$, is proportional to the energy density per unit wavenumber, k, in the magnetic field fluctuations

$$\int_{-\infty}^{\infty} I dk = \langle \delta B \bullet \delta B \rangle. \tag{5}$$

$I_+(k)$ is the intensity in waves propagating in the $+\hat{e}_b$ direction with $k>0$ ($k<0$) corresponding to right (left)-hand circularly polarized waves for $B_o>0$ and the reverse polarizations for $B_o<0$. $I_-(k)$ is the intensity in waves propagating in the $-\hat{e}_b$ direction with $k>0$ ($k<0$) corresponding to left (right)-hand circularly polarized waves for $B_o>0$ and the reverse polarizations for $B_o<0$ [*Lee*, 1983].

Substituting equation (1) into equation (3) and performing the μ-integration gives

$$v\frac{\mu}{2}\frac{\partial f_0}{\partial l} = (1-\mu^2)D_{\mu\mu}\frac{\partial g}{\partial \mu} - C(v,l), \tag{6}$$

where we have neglected $|\partial g/\partial l|$ with respect to $|\partial f_0/\partial l|$, and $C(v,l)$ is a constant of integration. Setting μ equal to ± 1, we obtain $C(v,l) = \frac{1}{2}v\partial f_0/\partial l$, which yields

$$\frac{\partial g}{\partial \mu} = -\frac{v}{2}\frac{\partial f_0}{\partial l}\frac{1}{D_{\mu\mu}}. \tag{7}$$

Equation (7) will be required in section 1.2.2 to derive the wave growth or decay rate. Integrating equation (7) yields

$$g(l,v,l,\mu) = -\frac{1}{2}v\frac{\partial f_0}{\partial l}\int_0^{\mu}\frac{1}{D_{\mu\mu}}d\mu', \tag{8}$$

where we have set the constant of integration to zero since $\int_{-1}^{1} g(\mu)d\mu = 0$. This form for the distribution function is less restrictive than the linear dependence of g on μ assumed by *Lee* [1982, 1983].

Next, we write the expression for the parallel streaming, or differential flux, S, and its relation in the diffusive limit to the parallel spatial diffusion coefficient K as

$$S = \frac{1}{2}\int_{-1}^{1} d\mu v\mu g(\mu) = -K\frac{\partial f_0}{\partial z}. \tag{9}$$

Substituting equation (8) into equation (9), rearranging terms, and integrating by parts yields [*Earl*, 1974]

$$K = \frac{1}{8}v^2\int_{-1}^{1} d\mu \frac{1-\mu^2}{D_{\mu\mu}}. \tag{10}$$

1.2.2 Derivation of the Wave Growth Rate and Solution for the Wave Intensity

The equation for the growth or damping rate of waves propagating in the $\pm\hat{e}_b$ direction due to the energetic ion distribution is given by *Lee* [1982] as

$$\gamma_\pm = \mp\frac{2\pi^3}{|k|}\frac{V_A}{c^2}\frac{q^2}{m}\int_0^\infty dv v^2\int_{-1}^{1} d\mu(1-\mu^2)\delta(\mu-\frac{\Omega}{kv})\frac{\partial f}{\partial \mu} \tag{11}$$

under the assumption $|\gamma_\pm| << |\omega| << |\Omega|$, and that the waves are non-dispersive. Generally the wave growth rate is maximized for parallel propagation [*Gary et al.*, 1981; *Hada et al.*, 1987], which also supports our consideration of parallel-propagating waves only. Substituting equation (7) into equation (11) and performing the μ-integration yields

$$\gamma_\pm = \mp\frac{V \mp V_A\cos\psi}{2I(k)}\frac{\partial A_\pm}{\partial z} \tag{12}$$

where

$$A_\pm(k,z) \equiv \frac{4\pi^2}{k^2}\frac{V_A}{V\mp V_A\cos\psi}|\Omega|m\cos\psi\int_{|\Omega/k|}^{\infty} dv v^3(1-\frac{\Omega^2}{k^2v^2})f_0(v,z), \tag{13}$$

where we have used $\partial z/\partial l = \cos\psi$, appropriate to the geometry upstream of the shock.

The wave kinetic equation upstream of the shock is [*Lee*, 1983]

$$-(V \mp V_A \cos\psi)\frac{\partial I_\pm}{\partial z} = 2\gamma_\pm I_\pm \,. \tag{14}$$

Substituting equation (12) for the growth rate into equation (14) yields

$$\frac{\partial I_\pm}{\partial z} = \mp\frac{I_\pm}{I}\frac{\partial A_\pm}{\partial z} \,. \tag{15}$$

Defining $\chi \equiv (V - V_A \cos\psi)/(V + V_A \cos\psi)$ equations (15) may be solved implicitly for I_+ and I_- as

$$\chi I_+ - I_-^0 (I_-^0/I_+)^\chi = \chi A_+ + \chi I_+^0 - I_-^0 \tag{16a}$$

$$I_- = I_-^0 (I_-^0/I_+)^\chi \,. \tag{16b}$$

where $I_\pm(k, z \to \infty) = I_\pm^0(k)$.

We now simplify equation (16a) with an approximation appropriate for interplanetary traveling shocks. Interplanetary hydromagnetic waves at relevant frequencies of 10^{-2}-10^{-1} Hz in the vicinity of 1 AU are observed to propagate predominantly away from the Sun [*Matthaeus and Goldstein*, 1982; *Tu and Marsch*, 1991], which is also the $\hat{e}_z$ (or $\hat{e}_b$) direction for an outwardly propagating traveling shock. Examining equations (12) and (13) and using the fact that $\partial f_0/\partial z < 0$, it can be seen that upstream waves propagating away from the shock front in the solar wind frame are unstable and waves propagating toward the shock are stable. Since the unstable waves also dominate the ambient wave

spectrum, we may take $I_-(k,z) \approx 0$. With this simplification equation (16b) vanishes and χ factors out of equation (16a) which reduces to

$$I(k,z) \approx I_+(k,z) \approx A_+(k,z) + I_+^0(k). \tag{17}$$

1.2.3 Comparison With Fluid Theory

We will now show that equations (13) and (16a) yield an expression for the enhanced wave energy density consistent with a fluid theory for the wave-particle interaction. The solution for the wave intensity in the limit of large enhancement, $A_+ >> I_+^0, I_-^0$, is

$$I(k,z) = A_+(k,z) = \frac{4\pi^2}{k^2}\frac{V_A}{V - V_A\cos\psi}|\Omega|m\cos\psi\int_{|\omega/k|}^{\infty} dv v^3\left(1 - \frac{\Omega^2}{k^2v^2}\right) f_0(v,z), \tag{18}$$

where we continue to take $-\hat{e}_0$ to be the unstable direction. Noting that $I(k,z)$ is an even function of k, we substitute equation (18) into equation (5) to obtain

$$\langle \delta B \bullet \delta B\rangle = 2\frac{4\pi^2 V_A|\Omega|m}{V - V_A\cos\psi}\cos\psi\int_0^{\infty}\frac{dk}{k^2}\int_{|\omega/k|}^{\infty} dv v^3\left(1 - \frac{\Omega^2}{k^2v^2}\right) f_0(v,z). \tag{19}$$

Changing the integration variable to $x = 1/k$, and noting that the wave magnetic energy density is $W_B = \langle \delta B \bullet \delta B\rangle(8\pi)^{-1}$, equation (19) becomes

$$W_B = \frac{\pi V_A|\Omega|m}{V - V_A\cos\psi}\cos\psi\int_0^{\infty} dx\int_{|\omega x|}^{\infty} dv v^3\left(1 - \frac{\Omega^2x^2}{v^2}\right) f_0(v,z) \tag{20}$$

Performing two integrations by parts on equation (20), and noting that $f_0(v\to\infty,z) = 0$, we obtain

$$W_B = \frac{2\pi V_A m}{3(V - V_A\cos\psi)}\cos\psi\int_0^{\infty} dv v^4 f_0(v) = \frac{1}{3}\frac{V_A}{V - V_A\cos\psi}W_p\cos\psi, \tag{21}$$

where W_p is the energy density of the energetic particles.

The same result is obtained from the fluid theory of *McKenzie and Völk* [1982]. For the case of a steady-state plasma with no source term, supporting waves propagating in the one unstable direction and generalizing their expression to arbitrary ψ, their wave energy equation (B.8) from the appendix is

$$\frac{\partial}{\partial z}\left[p_w\left(3U - 2V_A\cos\psi\right)\right] = U\frac{\partial p_w}{\partial z} + V_A\frac{\partial p_c}{\partial z}\cos\psi . \tag{22}$$

where p_c is the pressure of the energetic particles, p_w is the wave magnetic pressure, and U is the magnitude of the z-component of the plasma velocity. The left side of equation (22) is the divergence of the wave energy flux, which is the sum of the wave Poynting flux and the kinetic energy flux. The two terms on the right side are the rate of work done by the background plasma on the Alfvén waves and the rate of production of Alfvén wave energy due to the cosmic-ray streaming instability, respectively. Integrating equation (22) gives

$$2p_w(U - V_A\cos\psi) = V_A p_c\cos\psi . \tag{23}$$

The relation between pressure and energy density for nonrelativistic ions is

$$p_c = \tfrac{1}{3}W_p . \tag{24}$$

Combining equations (23) and (24), noting that $p_w = W_B$ and replacing U by V, immediately yields equation (21).

1.2.4 Solution of the Ion Transport Equation

We now examine ion acceleration at interplanetary traveling shocks with the wave intensity restricted to equation (17). The omnidirectional distribution function, f_0, of the shock accelerated ions is found by solving the nonrelativistic, time-independent, one-dimensional transport equation [*Parker*, 1965]

$$V_z \frac{\partial f_0}{\partial z} - \frac{\partial}{\partial z}\left(K \frac{\partial f_0}{\partial z}\right) - \frac{1}{3}\frac{\partial V_z}{\partial z} v \frac{\partial f_0}{\partial v} = N \frac{\delta(v - v_0)}{4\pi v_0^2}\delta(z). \qquad (25)$$

Equation (25) is valid in the frame of the shock under the conditions that $v >> V_z$ and that the particle distribution is nearly isotropic. The right side of equation (25) is the ion source term with ions injected at the shock with speed v_0, where N is the ion injection rate (ions $cm^{-2}s^{-1}$), and $\delta(z)$ is the Dirac delta function. The first two terms on the left are the convective derivative and the diffusion term, respectively. The last term on the left side is the adiabatic acceleration term due to the convergence of the flowing plasma. $V_z(z)$ is the average wave-frame velocity component in the z-direction where, $V_z(z < 0) = -V_d$ and $V_z(z > 0) = -(V - V_1 \cos\psi) \equiv -V'$. We take the upstream wave frame to be that of the unstable waves, and the downstream wave frame to be the plasma frame. We assume that the flow velocity changes discontinuously at the shock so that $\partial V_z / \partial z = -(V' - V_d)\delta(z)$. Here, K is the spatial diffusion tensor component in the z-direction

$$K = K_1 \cos^2\psi + K_\perp \sin^2\psi . \qquad (26)$$

We neglect diffusion perpendicular to the magnetic field ($K_{\perp}$) compared to parallel diffusion ($K_{\parallel}$), which is given by equation (10).

The wave intensity appears explicitly in equation (4) for $D_{\mu\mu}$, and so is implicit in equation (10) for $K_{\parallel}$. Equations (10), (17), and (25) constitute a set of complicated integro-differential equations for the wave intensity and the omnidirectional distribution function. Obtaining a closed form approximate expression for $K_{\parallel}$ simplifies the solution of this set of equations. To perform the integral in equation (10), following *Lee* [1982, 1983], we simply replace $I(\Omega/\mu v)$ by $I(\Omega|\mu| \mu v)$ in equation (4). The cyclotron resonance condition is $k = \Omega/v\mu$. Replacing k by $\Omega|\mu|/v\mu$ is equivalent to evaluating the wave intensity at the smallest wavenumber resonant with the given ion energy. We expect the wave intensity to be largest at small wavenumber. A given ion is actually resonant with waves for a range of wavenumbers about $k = \Omega/v\mu$ due to nonlinear resonance broadening [*Völk*, 1973; *Jones et al.*, 1973; *Goldstein*, 1976] and the scattering rate is dominated by the maximum intensity in this range. Thus, our replacement represents approximate inclusion of very effective resonance broadening in the scattering process. With this simplification, equation (10) yields

$$K_{\parallel} = m^2c^2v^3(8\pi q^2)^{-1} I_{\perp}(\Omega/v, z), \qquad (27)$$

where we have used $I_{\perp}^{o}(k,z) = I_{\perp}^{o}(-k,z)$ [*Matthaeus and Goldstein*, 1982; *Tu and Marsch*, 1991].

We define a new variable, ζ

$$\zeta(\Omega/v,z) = \int_0^z I_+(\Omega/v,z')dz' \tag{28}$$

and write equation (25) for $z > 0$ as

$$K_0 \frac{\partial^2 f_0}{\partial \zeta^2} + V'' \frac{\partial f_0}{\partial \zeta} = 0, \tag{29}$$

where

$$K_0 = m^2 c^2 v^3 \cos^2 \psi / 8\pi q^2. \tag{30}$$

The general solution to equation (29) is

$$f_0(\zeta(z),v) = A(v) + B(v)\exp[-V''K_0^{-1}(v)\zeta] \tag{31}$$

with a similar solution, with V_d replacing V'', for $z < 0$. To ensure that $f_0(\zeta(z \to \infty),v) \to 0$ we set $A(v) = 0$. To ensure a finite distribution for $z < 0$ we set $f_0(\zeta(z < 0),v) = C(v)$. To evaluate $B(v)$ and $C(v)$ we integrate equation (25) with respect to z across $z = 0$ and impose continuity of the distribution function at $z = 0$. We then obtain

$$f_0(\zeta(z),v) = \frac{\beta N}{4\pi v_0^3 V''} \left(\frac{v}{v_0}\right)^{-\beta} \exp[-V''K_0^{-1}(v)\zeta] S(v - v_0). \tag{32}$$

The step function, $S(v-v_0)$, has been explicitly included to ensure that the distribution function is zero for velocities less than the injection velocity. The power law spectral index is $\beta = 3r/(r-1)$, where $r = V''/V_d$ is the wave frame compression ratio across the shock.

We may solve for the wave intensity at the shock, $\zeta(0) = 0$, by substituting equation (32) into equation (13), and then using equation (17) to give:

$$I(|k| < |\Omega|/v_o, 0) = \frac{2\beta\pi|\Omega|mNV_A v_0^{\beta-3}\cos\psi}{(\beta-4)(\beta-2)V'^2}\frac{1}{k^2}\left|\frac{\Omega}{k}\right|^{4-\beta} + I_+^0(k) \qquad (33)$$

$$I(|k| > |\Omega|/v_o, 0) = \frac{\beta\pi|\Omega|mNV_A\cos\psi}{v_o V'^2}\frac{1}{k^2}\left\{\frac{v_o^2}{\beta-4} - \frac{\Omega^2/k^2}{\beta-2}\right\} + I_+^0(k). \qquad (34)$$

A finite result for the integration in equation (13) is obtained only for $\beta > 4$, which corresponds to a plasma compression ratio less than 4 (neglecting wave frame corrections), consistent with the upper limit for a nonrelativistic ($C_p - C_t = 5/3$) shock. A comparison between the predicted wave intensities, equations (33) and (34), and the observed wave intensities from *Kennel et al.* [1986] for the 11-12 November 1978 shock is presented in Chapter 1.3.

1.2.5 Approximate Analytical Solution for the Wave Intensity and Omnidirectional Distribution Function

In this section we determine closed form expressions for the wave intensity and omnidirectional distribution function at a traveling shock using the revised approximate analytical scheme of *Lee* [1983]. We check the success of this approximation against the numerical solutions in Chapter 1.3. From here on we consider only protons since they dominate the excitation of waves.

Following *Lee* [1983], we make the following simplification inside the integral in equation (13)

$$f_0(\zeta, v) \approx f_0\left(\zeta, |\Omega/k|\right)\left|\frac{vk}{\Omega}\right|^{-\beta}. \qquad (35)$$

This replacement is based on the assumed rapid decrease of $f_0(\zeta,v)$ with increasing v so that the integral is dominated by the integrand evaluated near the lower limit of integration: the specific velocity dependence of $f_0(\zeta,v)$ is less crucial. The z-dependence of $A_-(\zeta,v)$ is now determined by $f_0(\zeta(z),|\Omega/k|)$. Substituting the right hand side of equation (35) into equation (13) yields

$$A_-(k,\zeta) = \frac{4\pi^2 V_A^2 |\Omega| m\cos\psi}{V''} \frac{1}{k^2}\frac{\Omega}{k}\Big|^{\beta} f_0(\zeta,|\frac{\Omega}{k}|) \int_{\Omega/k}^{\infty} dv v^3 (1-\frac{\Omega^2}{k^2 v^2}) v^{-\beta}. \quad (36)$$

where the lower limit of integration satisfies $|\Omega/k| \geq v_a$. The approximation is appropriate only for this range of k. The integral in equation (36) can now be performed explicitly and gives

$$A_-(k,\zeta) = \frac{8\pi^2 V_A^2 |\Omega| m\cos\psi}{(\beta-4)(\beta-2)V''} \frac{1}{k^2}\left|\frac{\Omega}{k}\right|^4 f_0(\zeta,|\Omega/k|). \quad (37)$$

Combining equations (17), (32), and (37) allows the wave intensity to be written as

$$I_-(k,\zeta(z)) = \eta(k)\exp[-V'' K_0^{-1}(|\frac{\Omega}{k}|)\zeta] + I_-^0(k). \quad (38)$$

$$\eta(k) \equiv \frac{2\pi\beta\cos\psi}{(\beta-4)(\beta-2)} \frac{V_A^2}{V''^2} \frac{v_0^{\beta-3} Nm}{|\Omega|}\left|\frac{\Omega}{k}\right|^{6-\beta}. \quad (39)$$

Substituting equation (38) into the differential form of equation (28), $d\zeta/dz = I_-$, and integrating we find

$$V'' K_0^{-1}\zeta = \ln\left[(\eta + I_-^0)\exp(I_-^0 V'' K_0^{-1} z) - \eta\right] - \ln(I_-^0). \quad (40)$$

Substituting equation (40) into equation (38) yields

$$I_-(k,z) = \frac{I_-^0(\eta + I_-^0)}{\eta + I_-^0 - \eta\exp[-I_-^0 V'' K_0^{-1}(|\frac{\Omega}{k}|)z]}. \quad (41)$$

As $z \to 0$ we recover equation (33) for the wave intensity at the shock. As $z \to \infty$ equation (41) reduces to $I_- = I_-^0$.

Substituting equation (40) into equation (32) we obtain the omnidirectional distribution function

$$f_0(v,z) = \frac{\frac{\beta N}{4\pi v_0^3 V''}\left(\frac{v}{v_0}\right)^{-\beta} I_-^0(\Omega/v)}{[\eta(\Omega/v) - I_-^0(\Omega/v)]\exp[I_-^0(\Omega/v)V''K_0^{-1}(v)z] - \eta(\Omega/v)} S(v - v_0). \quad (42)$$

Equation (42) exhibits the correct limiting behaviors: $f_0(v,0)$ yields the standard power law in velocity for diffusive shock acceleration, and $f_0(v, z \to \infty) \to 0$. Equations (41) and (42) have the same form as derived by *Lee* [1983], but with a modified form of $\eta(k)$.

The ratio of equation (39) to the function from *Lee* [1983] corresponding to $\eta(k)$ is given by $(8/3)\beta/(\beta - 4)$. This ratio approaches 8/3 in the limit of large β and is of order 10 for typical interplanetary traveling shocks at 1 AU and therefore represents a substantial quantitative correction to *Lee's* results.

CHAPTER 1.3

NUMERICAL CALCULATIONS AND COMPARISON OF PREDICTIONS TO OBSERVATIONS

1.3.1 Numerical Solution for the Wave Intensity and the Ion Omnidirectional Distribution Function

We now describe the method used to solve numerically for the wave intensity and the omnidirectional distribution function. Combining equations (13), (17), and (32) produces an integral equation for the wave intensity

$$I_+(k,z) = \frac{\pi V_A |\Omega| m \beta N \cos\psi}{k^2 v_0^3 V''^2} \int_{v_r}^{v_0} dv v^2 \left(1 - \frac{\Omega^2}{k^2 v^2}\right) \left(\frac{v}{v_0}\right)^{-\alpha} \exp\left[-V'' K \int_z^{z'} I_+(\frac{\Omega}{v}, z')dz'\right] + I_+^0(k). \quad (43)$$

where $v_r = Max(v_0, |\Omega/k|)$. Defining the following dimensionless variables.

$$u = v_0 / v, \quad s = |v_0 k / \Omega|, \quad x = z |\Omega / V''|.$$

$$\bar{I}(s,x) = I(k,z) |\Omega| V''^2 / \pi V_A m v_0^3 \beta N \cos\psi.$$

$$M = 4\pi^{1/2} q N \beta / c |\Omega| \sqrt{nm} \cos\psi \quad (44)$$

enables equation (43) to be written as

$$\bar{I}(s,x) = \frac{1}{s^2} \int_0^{U_0} du u^{\beta-5} \left(1 - \frac{u^2}{s^2}\right) \exp\left[-Mu^3 \int_0^x \bar{I}(u,x')dx'\right] + \bar{I}_+^0(s). \quad (45)$$

In equations (44) and (45), m is the proton mass, $q = e$ is the proton charge, n is the proton density of the ambient plasma, and $U_0 = Min(s,1)$. The analytical approximation

for the wave intensity, equation (41), is at best valid for $s = 1$, but the numerical solution is valid for $s > 1$.

We assume the following form for $I_-^0(k)$ in order to carry out the solution of equation (45)

$$I_-^0(|k| < k_0) = I_0 \tag{46a}$$

$$I_-^0(|k| > k_0) = I_0 (|k|/k_0)^{-\gamma}. \tag{46b}$$

where $L_c = 2\pi/k_0$ corresponds to the correlation length of the turbulence. Setting the total integrated power equal to αB_0^2 we obtain

$$I_0 = \frac{\alpha B_0^2}{5k_0}. \tag{47}$$

The wave intensity for $x = 0$ is known exactly from equations (33) and (34). Also, the wave enhancement, $A_-(s,x) \to 0$, for $s \to 0$ since few high energy protons are available to excite waves at small s. These boundary conditions provide the starting values used to evaluate both integrals in equation (45). The integrals in equation (45) are approximated by summations employing a simple rectangular rule. A two-dimensional array of wave intensities, $\bar{I}_{ij} = \bar{I}(i\Delta s, j\Delta x)$, is constructed, where $\Delta s = 0.01$ and $\Delta x = 1$. Once intensities are computed for $s = 10$, x is set to the next larger value, and the process of stepping over s begins again. The upper limit for s of 10 was chosen because the limits of validity of the theory will determine a maximum acceptable value of s between 1 and 10 as we discuss later. At every step of the calculation, intensities at all previous (i.e. lesser) values of s and x are known. These previous values of intensity are used in the

summations to calculate the intensity at the current values of s and x. The sensitivity of the calculation to the size of Δs and Δx was investigated and it was found that finer increments did not improve the results. In the process of calculating the wave intensities, the omnidirectional distribution function, equation (32), is also calculated at corresponding discrete values of v.

Figures 1.1 through 1.9 display calculations using the following common set of parameters appropriate to the solar wind at 1 AU: $B_0 = 5nT$, $n = 4\,cm^{-3}$, $\alpha = 1$, $L_0 = 0.1$ AU. For these values $V_A \approx 55$ km/s. We assume that 1% of the incident protons in the solar wind are injected with $v_0 = V$ at the shock, which we take to be parallel ($\psi = 0$). We take $C_s = 50$ km/s as a reasonable representative value for the sound speed in the solar wind. A value of $V = 140$ km/s satisfies the Rankine-Hugoniot conditions for a parallel shock with $\beta = 7$, implying a wave-frame compression ratio of r = 7/4. This shock is above the Mach number range of the "switch-on" shock [*Priest*, 1982]. We have chosen parameters which give a large value of β in order to emphasize the wave enhancement relative to the background wave intensity.

Figure 1.1 depicts dimensionless wave intensities plotted versus $s = |v_0 k / \Omega|$ for several values of x. According to equation (44), the wave intensities are normalized to $\pi V_A m v_0^3 \beta N \cos\psi / |\Omega| V^2 = 0.0089 erg/cm^2$. The wave intensity spectra converge to the background wave intensity far from the shock and for very small s as mentioned above, because few protons are accelerated to sufficiently high energies to excite waves at small

s. The results are only valid in the MHD regime, $|\omega| << |\Omega|$. The vertical dotted line in Figure 1.1 at $|v_o k/\Omega| = 2$ indicates a high-s limit, beyond which the results are not expected to be valid. The limiting value of 2 was determined by taking $|\omega/\Omega| = 1/2$ as an upper limit, setting $\omega \cong kV_A$, and noting that $v_0 / V_A \approx 4$ for this set of parameters. The choice of $|\omega/\Omega| = 1/2$ is consistent with the assumption that the wave phase speed is approximately equal to the Alfvén speed, which may be verified from the dispersion relation for ion-cyclotron waves. As can be seen from equation (45), when the enhancement dominates and s is large, the leading factor s^{-2} determines the dependence of $\bar{I}(s,x)$ on s as indicated by the dashed line.

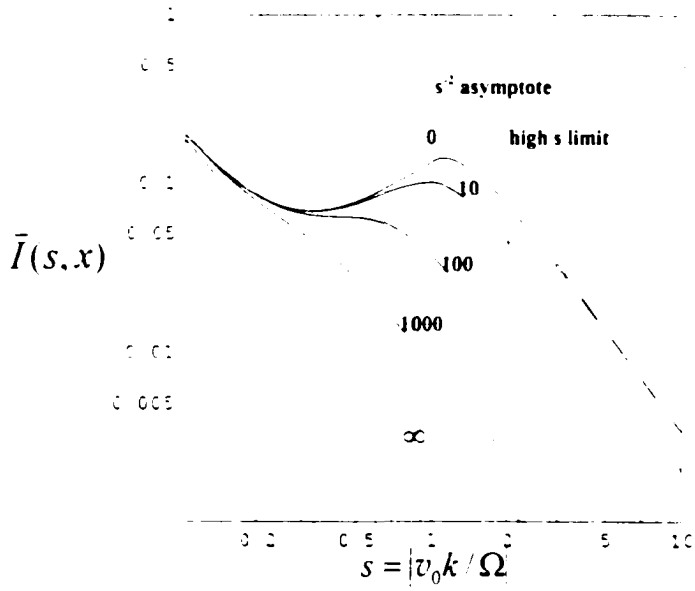

Figure 1.1 Dimensionless wave intensities (numerical solution) versus $s = |v_0 k/\Omega|$ at the indicated scaled distances from the shock ($x = x|\Omega/V_A|$).

In Figure 1.2 we present a plot of the analytical solution, equation (41). We restrict the domain of the wave intensity to $s \leq 1$ because the analytical approximation is certainly not valid for $|\Omega/k| < v_o$. The curves are qualitatively similar to those in Figure

1.1. For $\eta(k) >> I >> I_*^o$, the analytical expression for the enhanced wave intensity may be approximated by

$$I(k,z) \approx B_0^2 \cos^2 \psi |\Omega_p| (8\pi V' z)^{-1} |k|^{-1}. \quad (48)$$

This simple functional dependence on k is evident in the x = 10, 100, and 1000 scale-length curves in Figure 1.2.

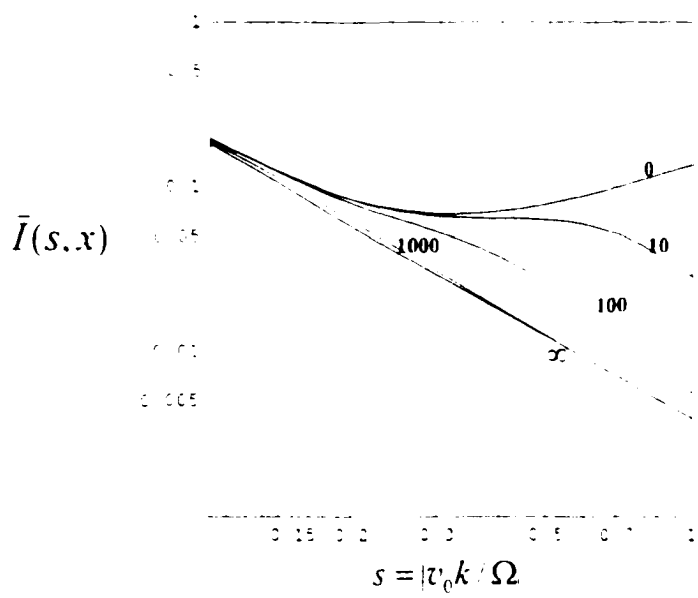

Figure 1.2 Dimensionless wave intensities (analytical solution) versus $s = |v_0 k / \Omega|$ at the indicated scaled distances from the shock.

To investigate the validity of the approximation described in Chapter 1.2 and used by *Lee* [1982, 1983] to obtain closed form expressions for the wave intensity and omnidirectional distribution function, we compare in Figures 1.3 and 1.4 plots of the wave intensity calculated numerically and analytically at distances from the shock of x = 10 and x = 100, respectively. Since the analytical approximation [*Lee*, 1982, 1983] is valid up to at most s = 1, it is not surprising to see the worst agreement at larger s. The numerically calculated wave intensities are greater than those determined using the

analytical approximation at large s for all values of x. The larger the value of x, the larger the difference as $s \to 1$. This is reasonable behavior since the approximation in equation (35) relies on f_0 decreasing for velocities larger than the lower limit of integration. We shall see that precisely where the agreement is poor this condition is not satisfied.

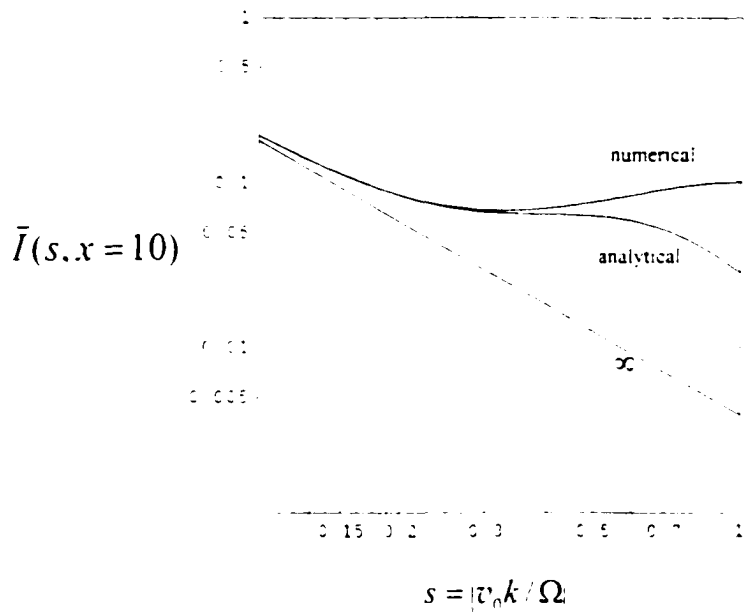

Figure 1.3 Numerically and analytically calculated wave intensity at a distance from the shock of x = 10.

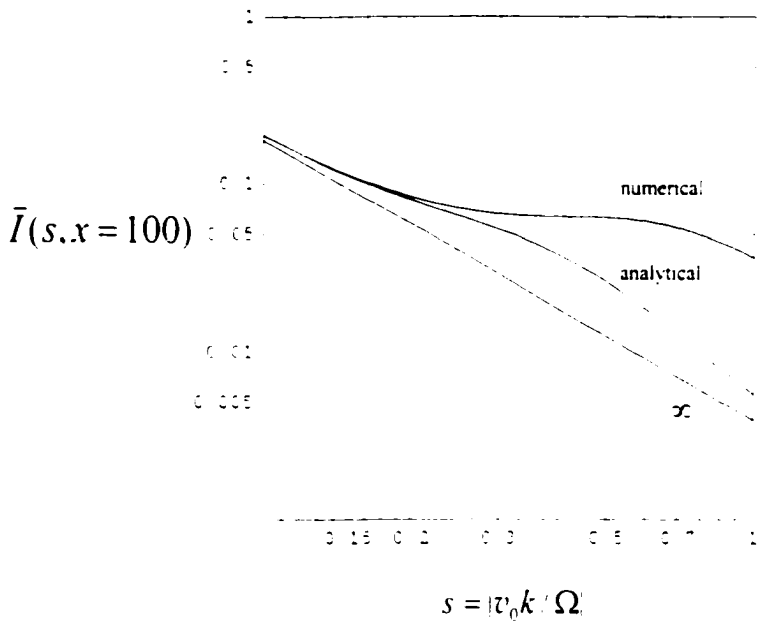

Figure 1.4 Numerically and analytically calculated wave intensity at a distance from the shock of $x = 100$.

Figures 1.5 and 1.6 depict the proton omnidirectional distribution function, normalized by $\beta N(4\pi v_0^3 V)^{-1} = 1.34 \cdot 10^{-23} s^3 cm^{-6}$, at the indicated distances from the shock based on the numerical calculation and the analytical approximation, equation (42), respectively. The power law dependence of $f_0(v)$ on v is evident at $x = 0$. The rapid downturn in the numerically calculated f_0 as $v \to v_0$ is reasonable since the low energy proton diffusion coefficients are small, resulting in larger spatial gradients and few low energy protons at large distances from the shock. As mentioned above, the analytical approximation depends on the integral in equation (13) being dominated by the integrand near the lower limit of integration. This is equivalent to requiring that f_0 decrease with increasing velocity. It can be seen in Figure 1.5 that at large x and small v this approximation breaks down, so that large discrepancies exist between the analytical and

numerical solutions. The dotted vertical line in Figures 1.5 - 1.7 indicates a lower limit for the validity of our theory of diffusive ion transport. We return to its determination later.

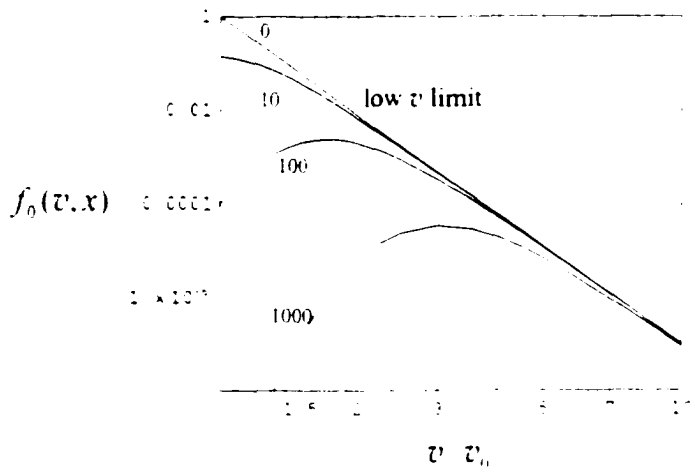

Figure 1.5 Dimensionless omnidirectional distribution function (numerical solution) versus v / v_0 at the indicated scaled distances from the shock.

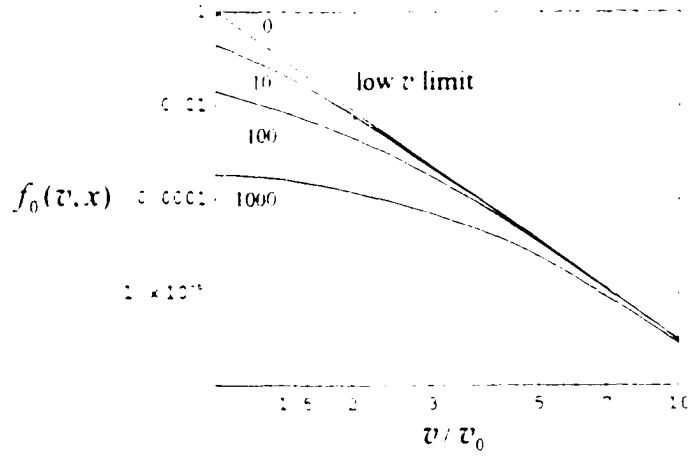

Figure 1.6 Dimensionless omnidirectional distribution function (analytical approximation) versus v / v_0 at the indicated scaled distances from the shock.

Figure 1.7 compares the omnidirectional distribution function calculated numerically to that determined by the analytical approximation at $x = 100$. There is excellent agreement for $v \geq 2v_o$ and worsening agreement for smaller values of v. This behavior is

consistent with that exhibited in Figure 1.4 for the wave intensity comparison at x = 100. Since protons and waves are coupled through the cyclotron resonance condition, the breakdown in the analytical approximation of the wave intensity above $|k| \approx 0.5|\Omega| \cdot v_0$ corresponds to the breakdown in the approximation of the proton distribution below $v \approx 2v_0$. This restriction of $v \geq 2v_0$ for the validity of the analytical approximation at x = 100 is coincidentally the same as the fundamental restriction for diffusive ion transport indicated by the vertical dotted line.

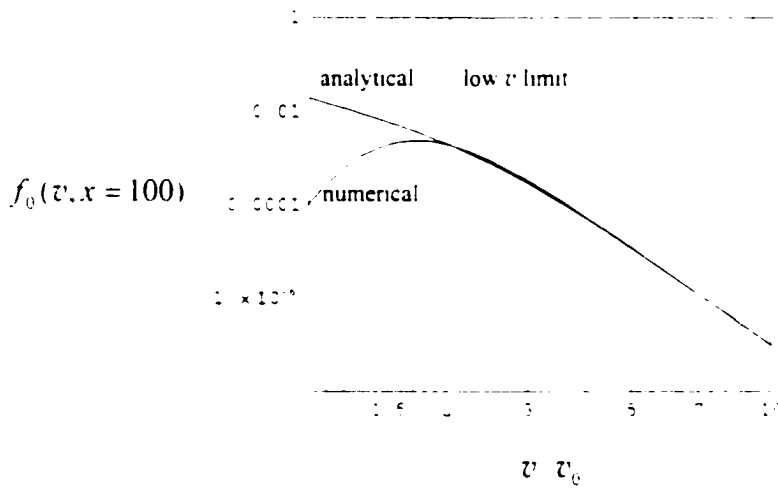

Figure 1.7 Analytically and numerically calculated distribution functions at a distance from the shock of x = 100.

One of the basic assumptions used to simplify the solution of the pitch-angle diffusion equation and legitimately apply equation (25) is that $|g(v,z,\mu)| << f_0(v,z)$. We determine g at the shock by combining equations (4), (8), (41), and (42). We may use equations (41) and (42) since the analytical approximation is exact at the shock. For simplicity we compare $g(v,z = 0,\mu)$ to $f_0(v,z = 0)$ first as a function of μ for v/v_0 = 5 (Figure 1.8), then as a function of v for μ = 1 (Figure 1.9). In Figure 1.8 we plot

$g(v, z = 0, \mu)$ for $\mu \geq 0$ only, but note that it is an odd function of μ. Figure 1.8 shows that at the shock $g(v, z = 0, \mu)$ is not a linear function of μ as assumed by *Lee* [1982, 1983] but still maximizes at $\mu = 1$. Equation (25) requires that the ion distribution is nearly isotropic ($|g| << f_0$). We note from Figure 1.9 that $v / v_0 \geq 2$ is required to satisfy $|g| \leq f_0$. This fundamental limitation of the theory is indicated by the dotted vertical line in Figures 1.5-1.7.

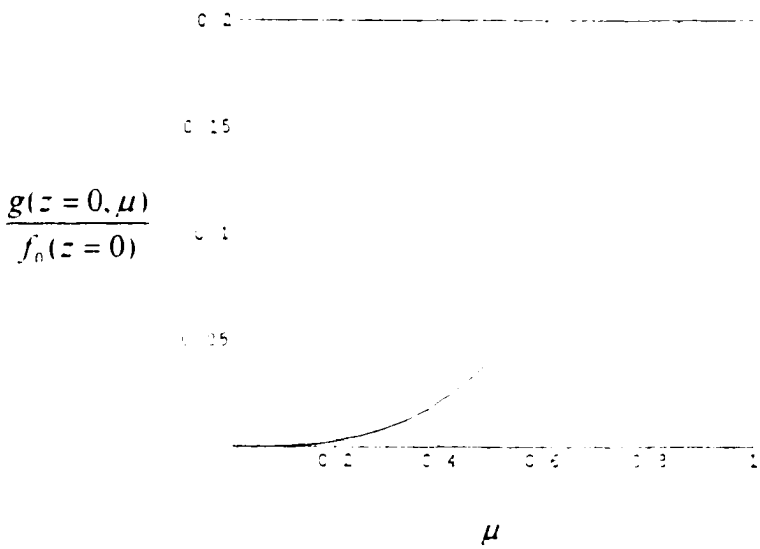

Figure 1.8 Ratio of the anisotropic part of the proton phase-space distribution, g, to the omnidirectional distribution function, f_0, at $v/v_0 = 5$ as a function of μ.

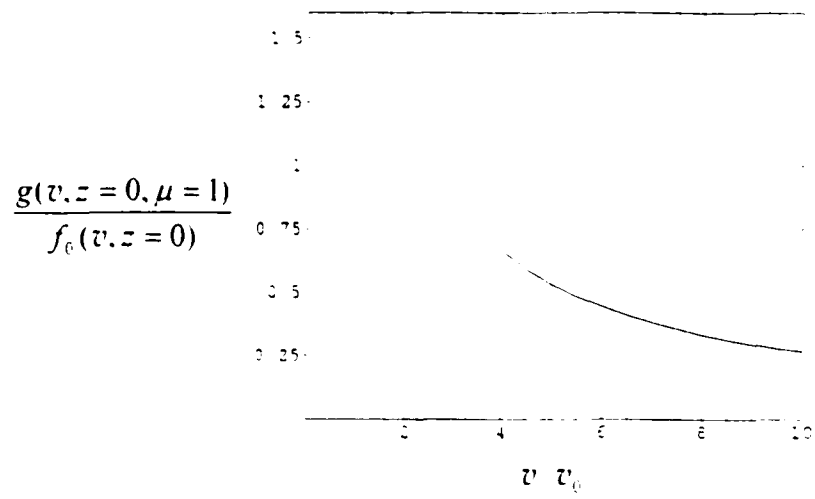

Figure 1.9 Ratio of the anisotropic part of the proton phase-space distribution, g, to the omnidirectional distribution function, f_0, at $\mu = 1$ as a function of $v\ v_0$.

1.3.2 Wave Intensity at the 11-12 November 1978 Shock

We now compare the predicted wave intensity spectrum to the wave observations by ISEE-3 at the 11-12 November 1978 shock as presented by *Kennel et al.* [1986]. Wave spectra are usually measured in units of $(nT^2\ Hz)$ as functions of wave frequency in the spacecraft frame. Therefore, in order to make a meaningful comparison we rewrite equations (33) and (34) as functions of frequency using the Doppler condition

$$2\pi f = |\mathbf{k} \bullet \mathbf{V}_{sw}|, \tag{49}$$

where we have neglected $|\omega|$ compared with $|\mathbf{k} \bullet \mathbf{V}_{sw}|$. The angle between $\mathbf{B}_0$, or $\mathbf{k}$, and $\mathbf{V}_{sw}$ is about 25° [*Tsurutani et al.*, 1983; *Kennel et al.*, 1984]. We make the transformation from intensity to power spectral density, P, through $Pdf = 2 \cdot 10^{10} Idk$. The factor of two arises because f includes both signs of k and the factor 10^{10} accomplishes the conversion of G^2 to nT^2.

We determine the ion injection rate, N, from

$$f_0(0,v) = \frac{\beta N}{4\pi v_0^3 V''}\left(\frac{v}{v_0}\right)^{-\beta}. \qquad (50)$$

with $f_0(0, 1800km\ s) = 2\cdot 10^{-28} s^3 cm^{-6}$ as specified by *Kennel et al.* [1986]. We use the following parameter values specified by *Kennel et al.* [1986]: $B_0 = 6.85nT$, $V = 238km\ s$, $\beta = 4.3$, $n = 4\ cm^{-3}$, and $\psi = 41^0$. We also take $v_0 = V$.

Figure 1.10 shows the comparison between the predicted wave power and ISEE-3 data reproduced from Figure 1.9 of *Kennel et al.* [1986]. The observed wave power was obtained during the time segment 00:25:40-00:28:15 UT on 12 November 1978, a period of 155 s which ended one second before the shock passed over ISEE-3. The prediction involves no free parameters.

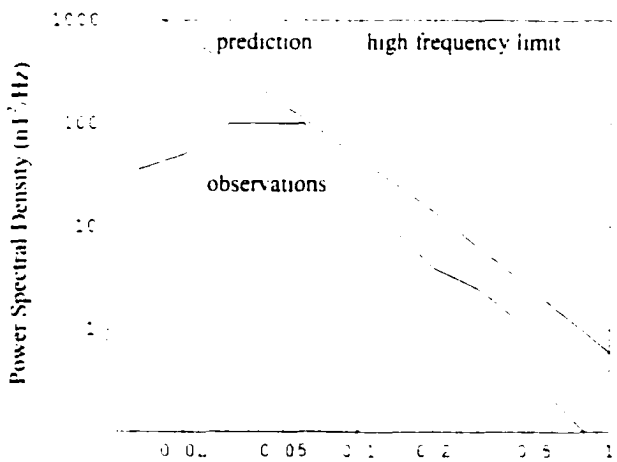

Figure 1.10 Predicted wave power spectral density at the shock compared to observations. The measured wave power spectral density is from Figure 1.9 of *Kennel et al.* [1986].

There is fairly good agreement between the predicted wave intensity and the observations in the frequency range between about 0.03 Hz and 0.3 Hz. There is roughly an order of magnitude discrepancy between the predicted and observed intensity at low frequencies. The power-law form of the prediction follows from the power-law dependence of the proton velocity distribution at the shock. The frequency of observed peak intensity corresponds to proton energies of about 10 keV. A drop in wave power at lower frequencies would have to correspond to a cutoff in the proton distribution above the resonant energy. However, the proton distribution at the shock is observed to be a power law in velocity out to at least 200 keV [*Scholer et al.*, 1983] corresponding to a resonant frequency of about $6 \cdot 10^{-3}$ Hz. We suspect that the observed decrease at low frequencies is due to Fourier transforming the data recorded over a period of time too short to contain all the low frequency power. *Tsurutani et al.* [1983] present the power spectral density for the 11-12 November 1978 shock event averaged over a 25 minute interval prior to shock passage and do not find a dramatic decrease in power at low frequency, although it is lower overall than our prediction which is the maximum power (determined at the shock).

At the beginning of the time interval of 155 s used by *Kennel et al.* [1986] with a shock speed of about 600 km/s the shock front was about 250 L_s from ISEE-3. Upstream waves at that distance from the shock are predicted to be significantly lower in power than waves at the shock. To account for this variation, we average the predicted wave spectra from 250 L_s up to the shock and compare this average power spectral density to the observations in Figure 1.11. The wave magnetic power was determined numerically

at every position except at the shock. The fit, which involves no free parameters, now predicts an average power spectral density lower than that observed, but is much better between 0.03 and 0.3 Hz, indicating that the theory may even be valid at frequencies beyond our rather liberal upper limit, indicated by the dotted vertical line.

Regardless of whether we use the predicted power at the shock, or power averaged over the observation period for comparison with observations, there is also a significant discrepancy between the predicted and observed spectra at frequencies above approximately 0.5 Hz. Since we restrict $\tau \geq 2\tau_0$, the theory is not valid at frequencies higher than about 0.1 Hz, indicated by the dotted vertical line in Figures 1.10 and 1.11. Therefore, we don't expect good agreement at high frequencies.

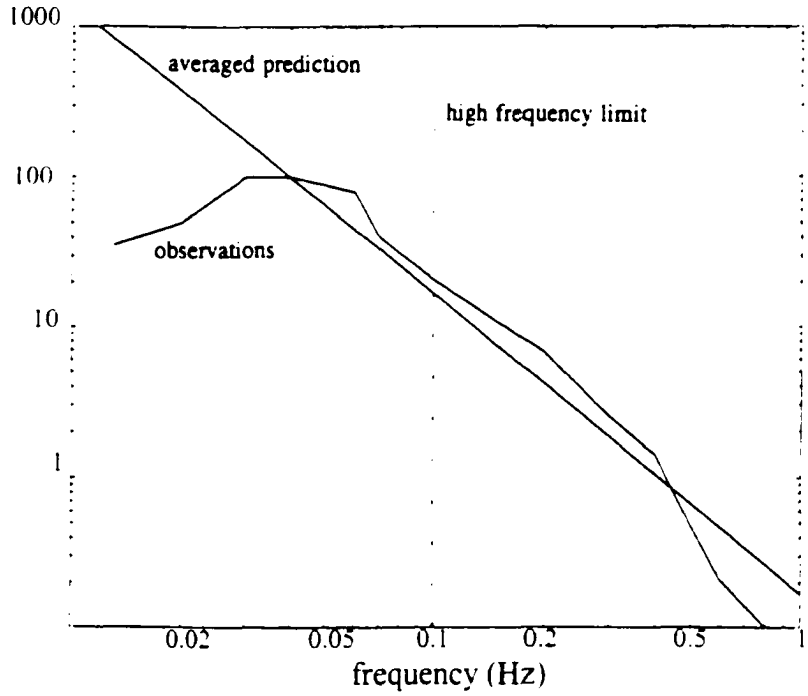

Figure 1.11 Average predicted wave power spectral density compared to observations for the November 11 – 12, 1978, shock.

1.3.3 Wave Enhancements Upstream of Earth's Bow Shock

A statistical study of 620 magnetic fluctuation enhancements associated with diffuse ion events upstream of Earth's bow shock was performed by *Trattner et al.* [1994] using data recorded by the AMPTE/IRM (Active Magnetospheric Particle Tracer Explorers/Ion Release Module) satellite. The study was based on two periods from September 1984 to December 1984, and from September 1985 to December 1985. These time periods were selected because they corresponded to times when the highly elliptical orbit of AMPTE/IRM brought the satellite upstream of Earth's bow shock. Designation of an upstream event required that the proton flux at 40 keV had reached a plateau for at least 10 minutes. A wide range of the region upstream of Earth's bow shock was sampled to produce the data set. Figure 1.4 of *Trattner et al.* [1994] provides information about the satellite's location during the two four-month periods.

For each event, the diffuse proton energy density was computed by integrating the differential energy spectrum from 8.4 keV to 230 keV. Ion energies per charge were determined by the SULEICA (Suprathermal Energy Ionic Charge Analyzer) instrument built by the Max-Plank-Institut für extraterrestrische Physik and the University of Maryland. Solar wind speed and ion number density were measured by the 3-D plasma instrument. The Alfvén speed was inferred from the background magnetic field and ion number density measurement. Magnetic field measurements were made with the tri-axial fluxgate magnetometer built by the Technical University Braunschweig [*Lühr et al.*, 1985]. The magnetic field sampling rate was 32 s^{-1} and the wave power spectral density was derived by performing a Fast Fourier Transform on the time domain data. Total

magnetic fluctuation energy density was calculated separately for each event by integrating the spectrum from the high frequency end down to the low frequency minimum, determined as the point where the wave intensity drops to the background level. The shock normal direction at the intersection of the bow shock with the magnetic field line at the spacecraft was determined using a 10 minute average of magnetic field direction with an assumed bow shock geometry modeled by a paraboloid of revolution [*Fairfield*, 1971].

Trattner et al. [1994] compared the measured field fluctuation energy density for each of the 620 events with that predicted by *Lee* [1982] based on the observed energy density of the diffuse protons. That prediction was flawed by the assumption that $g(v,\mu) \propto \mu$. Equation (21) is appropriately general concerning the form of $g(v,\mu)$, but is based on large wave enhancements ($A_z >> I_z^+$) and a planar shock geometry. The condition $A_z >> I_z^+$ is appropriate at Earth's bow shock particularly near the nose where it is strongest. The planar shock geometry would appear to be inappropriate. However, the generalization of wave kinetic equation (14) involves $(\mathbf{V}_{sw} - V_A\hat{e}_b)\bullet\nabla I \propto -\hat{e}_b \bullet \nabla f_o$ for the unstable wave intensity. Since the waves are excited by the diffuse protons, it is reasonable to assume that ∇I and ∇f_o are parallel. Then we have $(V_{sw}\hat{e}_z - V_A\hat{e}_b)\bullet\hat{e}_g|\nabla I| \propto (\hat{e}_b \bullet \hat{e}_g)|\nabla f_o|$. where $\hat{e}_z$ here is the unit vector in the sunward direction and $-\hat{e}_g$ is the unit vector in the direction of the gradient. This expression is identical in form to equation (14) or (15) and may be integrated to yield expressions

analogous to equation (18) and (21). The form of equation (21) generalized to the bow shock is

$$W_B = \frac{1}{3}\frac{V_A(\hat{e}_b \bullet \hat{e}_g)}{V_{sw}(\hat{e}_z \bullet \hat{e}_g) - V_A(\hat{e}_b \bullet \hat{e}_g)} W_{\perp} \qquad (51)$$

Note that this integral of the wave kinetic equation is independent of the functional form of f_0, which does depend crucially on the 3-D structure of Earth's bow shock.

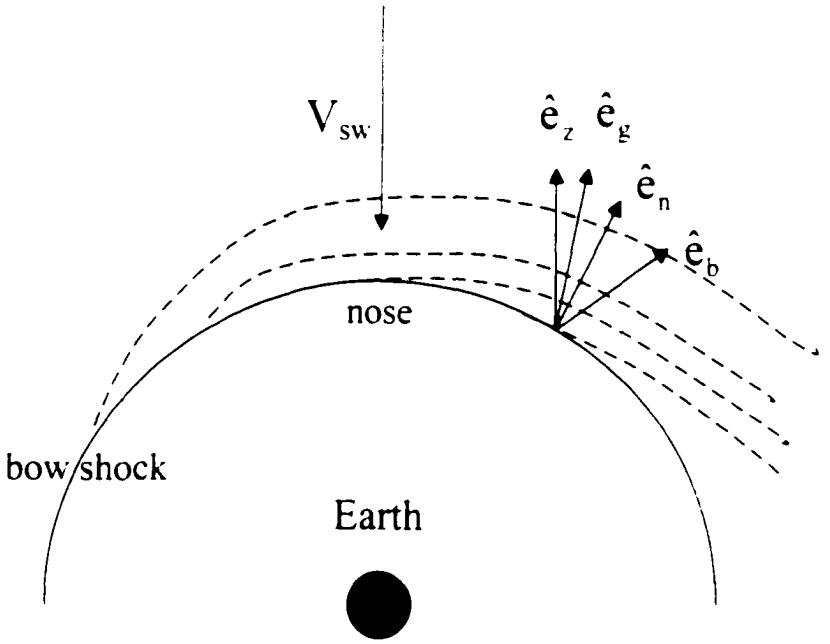

Figure 1.12 Schematic diagram of Earth's bow shock with the approximate directions of the solar wind, shock normal, magnetic field and energetic particle spatial gradient at a specific point on the shock. The dashed lines are energetic particle contours.

The unit vectors in equation (51) are depicted in a schematic diagram of the bow shock in Figure 1.12. Although $\hat{e}_g$ is unknown, it is likely to lie between $\hat{e}_z$ and $\hat{e}_n$, the outward unit vector normal to the shock surface. The fact that the waves and ions decrease in intensity with distance from the shock would appear to imply that $\hat{e}_g$ and $\hat{e}_n$

are parallel. However, as a flux tube and its accelerating ions is advected across the shock from the point where the field is tangent to the shock surface, the diffuse ion and excited wave intensity builds in the flux tube and results in intensity contours shown schematically in Figure 1.12 as dashed lines. The resulting gradient on the dawn side where the ion intensities are greatest and spatially extended (also above and below the plane of Figure 1.12) then lies approximately between $\hat{e}_z$ and $\hat{e}_n$. In order to circumvent the ambiguity introduced by the uncertainty in the direction $\hat{e}_g$, we take $\hat{e}_g = \hat{e}_n$ but restrict consideration initially to those events (~400) near the nose of the bow shock with $\hat{e}_z \bullet \hat{e}_n > \cos 25^\circ$.

In Figure 1.13 we present a scatter plot for the events near the nose of the bow shock. For each event the measured W_B is plotted versus the predicted W_B based on equation (51) and the measured values of W_p, V_{sw}, V_A and $\hat{e}_n$. The correlation is clearly very good. A linear regression fit to the data produces a correlation coefficient of 0.92, which strongly supports the coupling of the waves and particles in this process. The good correlation is independent of the magnitude of the event and its location relative to the shock. The best linear fit to the data passing through the origin is shown in Figure 1.13. Its slope of 0.63 indicates that the observed W_B on average is ~63% of that predicted. We have also constructed scatter plots for near-nose events with $\hat{e}_g = \hat{e}_z$, and for all events with $\hat{e}_g = \hat{e}_n$ and $\hat{e}_g = \hat{e}_z$. They exhibit slightly lower correlation coefficients in the range 0.85 - 0.88 and similar best-fit slopes, indicating that the results are not sensitive to the uncertainty in $\hat{e}_g$, and possibly the assumption that the gradients of I and f_o are

parallel. We discuss possible explanations for the discrepancy between the observed and predicted magnetic fluctuation energy densities in the next chapter.

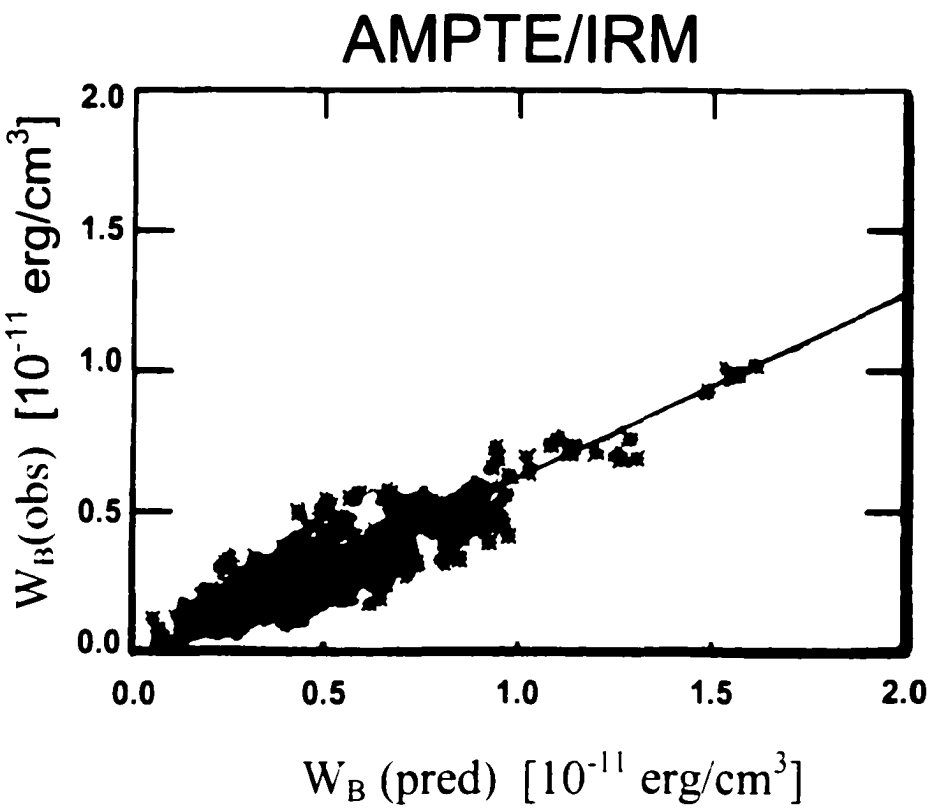

Figure 1.13 Observed magnetic energy density plotted versus the predicted magnetic energy density for a subset of the events studied in the survey of *Trattner et al.* [1994].

CHAPTER 1.4

DISCUSSION AND CONCLUSIONS

The self-consistent theory of *Lee* [1982, 1983] for the coupled ion acceleration and wave excitation at shocks assumed a distribution function that depends linearly on the cosine of the pitch-angle, μ, to describe the proton anisotropy. That *ansatz* is not necessary, nor is it in general correct as shown in Figures 1.8 and 1.9. We derived the correct μ-dependence by solving the pitch-angle diffusion equation under the assumption of strong scattering. The equivalent assumption, that the proton anisotropy is a small perturbation compared to the omnidirectional distribution function, is not correct under all conditions, but is approximately true over much of the range of speed v and μ. The resulting anisotropic part of the proton distribution determines the correct wave growth or damping rate, which in turn determines the self-consistent wave intensity $I(k,z)$, and proton omnidirectional distribution function $f_0(v,z)$. We solved the equations for these quantities numerically for representative parameters. In addition, the new approximate analytical expressions for $f_0(v,z)$ and $I(k,z)$ are qualitatively similar in form to those derived by *Lee* [1982, 1983], but quantitatively different.

The analytical approximations, given by equations (41) and (42), agree with the numerical solutions at small distances from the shock and over most of the allowed range

of k or v. The discrepancy in $I(k,z)$ between the analytical approximation and the numerical solution increases as the distance from the shock increases or as $v_0 k/\Omega \rightarrow 1$, which is the most optimistic limit of validity of the approximation. Similarly, the discrepancy in $f_0(v,z)$ between the analytical approximation and the numerical solution increases with increasing distance from the shock or as $v/v_0 \rightarrow 1$, where v_0 is the injection speed.

The basic theoretical formalism developed here is invalid in the small v, high k limit for two reasons. Firstly, the energetic particle transport equation, equation (25), formally requires $v >> V \cong v_0$. Secondly, in both the cyclotron resonance condition and the wave dispersion relation, we assumed $|\omega| << |\Omega|$. The second condition requires $v\mu >> V_A$, which is less restrictive than the first condition since $V > V_A$. Thus, we suggest optimistically that the numerical results for $f_0(v,z)$ are valid for $v \geq 2v_0$. Correspondingly, the numerical results for $I(k,z)$ are certainly valid for $|k| \leq 0.5|\Omega| \; v_0$. Given the high probability of very effective resonance broadening in the scattering process, the numerical results for $I(k,z)$ may be valid for larger values of $|k|$ as depicted in Figure 1.1.

The self-consistent theory of *Lee* [1982, 1983] and the current theoretical treatment approximate K by employing an effective resonance broadening. The replacement of $I(|\Omega|/v\mu)$ by $I(|\Omega||\mu|/v\mu)$ allows the integration of equation (10), thus providing a closed form solution for $K_{\parallel}$, and in part obviates the need for a non-linear treatment of particle

scattering by waves [*Völk*, 1973; *Jones et al.* 1973; *Goldstein*, 1976]. Excellent agreement between the measured spatial diffusion coefficients [*Tan et al.*, 1989] and those predicted by the theory of *Lee* helps support this simplification. It would be informative to re-compute spatial diffusion coefficients using the revised theory and again compare those to the observationally determined values [*Tan et al.*, 1989].

The predicted wave power spectral density at the shock (Figures 1.10 and 1.11) agrees quantitatively very well with the observations of the 11-12 November 1978 event [*Kennel et al.*, 1986] between 0.03 and 0.3 Hz. The theory predicts that the wave intensity should decrease monotonically with increasing frequency which is supported in part by the observations. The deviation at low frequency is presumably due to the short measurement period of 155 s just ahead of the shock. Figure 1.9c of *Tsurutani et al.*, [1983] is also a plot of power spectral density at the November 11-12 shock but for a measurement period of 25 minutes prior to shock passage. Their data do not exhibit a drastic rollover at low frequency, but are a little lower in overall magnitude presumably because it is an average of wave energy over a ten-fold longer time period than the *Kennel et al.* [1986] results. The observed power spectral density in Figure 1.10 is uniformly lower than that predicted, again because the observed wave energy is averaged over a 155 s time period during which time the power is increasing to the shock. Much improvement in agreement is achieved when the average predicted power spectral density is compared to the observations (Figure 1.11). The predicted wave intensity deviates from the observed intensity at high frequency, too. This is expected as the theory

formally breaks down for $|k| \geq 0.5|\Omega|/v_0$. The vertical dotted line in Figures 1.10 and 1.11 indicates this high frequency limit.

Kennel et al. [1986] and *Tsurutani et al.* [1983] identify waves of definite helicity present during the 11-12 November 1978 shock event. *Tsurutani et al.* [1983] show evidence that the waves have predominantly right-handed helicity with varying degrees of ellipticity. This behavior is supported by *Kennel et al.* [1986]. However, *Kennel et al.* [1986] also show that the "handedness" of the helicity changes with time, suggesting an average helicity close to zero. We predict vanishing average helicity due to the even functional dependence of $A_+(k,z)$ on k, evident in equation (13). The predicted lack of a net helicity is not due to the original assumption of *Lee* [1982, 1983] that $g \propto \mu$ as suggested by *Kennel et al.* [1986]. When a net helicity is observed, it may be due to non-stationarity or large anisotropies at low particle speeds, complications not addressed by the current theory.

Our prediction (21) for the wave magnetic energy density W_B in terms of the proton energy density W_p upstream of a planar stationary shock is in agreement with the fluid theory of *McKenzie and Völk* [1982]. A linear relation between these two quantities at Earth's bow shock was established by *Möbius et al.* [1987] and *Trattner et al.* [1994]. We have generalized equation (21) to incorporate approximately the spatial structure of Earth's bow shock; the result is equation (51). Equation (51) is a local relation between W_B and W_p resulting from the local energy transfer from protons to waves due to pitch-

angle scattering in the wave frame. The dominant effect of the shock spatial structure is a softer (exponential) energy spectrum, to which the form of equation (51) is insensitive.

Figure 1.13 presents a scatter plot of the observed W_B versus that predicted by equation (51) for each of the events in the statistical survey of *Trattner et al.* [1994] which was magnetically connected to the bow shock within 25° of the subsolar point (~400 events). The correlation coefficient is excellent (0.92). However, on average the observed value of W_B is 63% of the predicted value. There are two possible explanations for the discrepancy: wave damping or a measured proton energy density which is larger than the actual value.

Damping of the excited waves is not included in the theory we have presented. However, the excited wave amplitudes at Earth's bow shock are often comparable to the ambient field strength [*Hoppe et al.*, 1981] and subject to linear Landau damping, which is enhanced by wave refraction oblique to the ambient magnetic field [*Barnes*, 1966, *Hada et al.*, 1987], as well as several nonlinear processes. Nonlinear Landau damping may be important [*Lee and Völk*, 1973]. Oblique compressive modes steepen to form shocklets [*Hoppe et al.*, 1981; *Hada et al.*, 1987], which heat the solar wind plasma. Mode-mode coupling to wave modes at frequencies outside the measurement bandwidth can also occur, yielding less wave energy in the cyclotron-resonant frequency range.

In addition, it should be pointed out that the result depicted in Figure 1.13 depends on the absolute values of both W_B and W_p. Absolute calibration of instruments, especially

particle detection instruments, depends on detector efficiencies and are notoriously difficult to obtain. Based on experience, the remaining calibration uncertainties can be considered to be as high as 30%.

A significant discrepancy exists between the current theoretical expression for the wave enhancement at $z = 0$ and that derived by *Lee* [1983] (see section 1.2.5). For typical traveling shocks at 1 AU, the ratio of these wave enhancements is about 10. We might expect a similar discrepancy when comparing the current expression to the comparable earlier result for Earth's bow shock. It is then interesting to compare the numerical coefficient of W_B / W_p from the current theory, which equals 1/3, with that of *Lee* [1982, 1983]. The numerical coefficient of W_B / W_p from *Lee* [1983] for interplanetary traveling shocks is $3/8\beta(\beta - 2) << 1/3$ for any realistic value of β. However, the predicted wave magnetic energy density as derived by *Lee* [1982] for Earth's bow shock and presented in *Trattner et al.* [1994] compares quite well with the observations. This good agreement was due to a fortuitous numerical error made in evaluating the integral associated with equation (37) of *Lee* [1982]. The resulting numerical coefficient of $W_B / W_p \approx 0.36$, obtained with $\beta = 4.26$, is close to the current value of 1/3. Based on *Lee's* [1982] equation (37), *Trattner et al.* [1994] plotted the observed wave magnetic energy density versus that predicted and obtained a slope of 0.6 with a correlation coefficient of 0.89. However, if corrected, equation (37) of *Lee* [1982] would result in a prediction that would not match the observations.

The coupling of quasi-linear theory and ion shock acceleration is the theoretical foundation of part one of this dissertation, which has been used successfully to describe energetic particle energization and hydromagnetic wave generation associated with interplanetary traveling shocks and planetary bow shocks. There still remains a need for a detailed survey of the characteristics of upstream waves and particles at interplanetary traveling shocks observed over the last 20 years. Here we have considered only the event of 11-12 November 1978. Systematic comparisons should be made between theoretical predictions and observations of the ion distributions and wave enhancements for a large sample of events. A complication arising from the investigation of traveling shocks for comparison with the current theory is that they have longer scale lengths than Earth's bow shock and therefore provide even more time for wave damping. However, an ameliorating effect is that interplanetary traveling shocks are generally weaker, so that nonlinear effects should be smaller.

Other heliospheric shocks may lend themselves to a description by self-consistent quasi-linear theory. The shocks bounding corotating interaction regions (CIRs) in the solar wind are a possible example. Shocks form at CIRs where high speed solar wind overtakes slower speed wind. *Tsurutani et al.* [1982] reported enhanced MHD fluctuations upstream of CIR shocks accompanied by the acceleration of ions to energies greater than 1 MeV. *Fisk and Lee* [1980] solved the particle transport equation including adiabatic deceleration and showed that protons may be accelerated to ~1 MeV by diffusive shock acceleration at the forward and reverse shocks bounding the CIR. Their results produced distribution functions that are exponential in velocity, consistent with

observations. However, they assumed a form for the spatial diffusion coefficient proportional to ion speed and radius from the Sun which did not include a sheath of magnetic fluctuations upstream of the shocks excited by the accelerated protons.

In spite of the success of quasi-linear theory in predicting upstream wave enhancements, many examples of non-linear phenomena exist whose descriptions are inaccessible with quasi-linear theory. Using ISEE-2 data, *Spangler et al.* [1988] observed correlations between density fluctuations and the square of the magnetic field fluctuations in Earth's foreshock, suggesting a modulational instability of MHD waves in a high β plasma. In this context β = kinetic pressure magnetic pressure. *Scholer and Burgess* [1992] using a 1-D hybrid simulation of a collisionless shock showed that upstream waves could steepen sufficiently to re-form the shock provided that reflected ions were also present. *Scholer et al.* [1993] using a 2-D hybrid simulation of a quasi-parallel collisionless shock confirmed this view of shock reformation. Short large-amplitude magnetic structures (SLAMS) are observed in the quasi-parallel region of Earth's foreshock [*Mann and Lühr*, 1992; *Schwartz et al.*, 1992]. These magnetic structures possess magnetic field amplitudes up to several times the ambient field strength and left-hand polarization in the plasma frame. *Dubouloz and Scholer* [1993] performed a 1-D hybrid simulation of a hot ion beam injected into a cold background flow and observed the growth of ULF electromagnetic waves. As these waves grow in amplitude they scatter the beam ions. Beam ion clumps form that have a fraction of counterstreaming particles which de-stabilize the left hand ion beam mode. This process produces magnetic field structures resembling SLAMS. *Claßen and Mann* [1998]

performed test particle calculations of superthermal proton trajectories moving in regions of large magnetic fluctuations. They showed that these SLAMS prevent reflected protons from escaping into the region upstream of the shock and that the reflection of protons by the SLAMS increases the proton energies which then contribute to downstream heating. These interesting nonlinear wave-wave and wave-particle phenomena are beyond the scope of quasi-linear theory. However. an extension of the self-consistent theory of ion acceleration and wave excitation that includes possible wave dissipation mechanisms should be investigated.

PART II

RESONANT WAVE-ION INTERACTIONS IN THE EXTENDED CORONA: HEATING AND ACCELERATION OF PROTONS AND HEAVY ION SPECIES

CHAPTER 2.1

INTRODUCTION

Observations over nearly three decades show that ion distributions in the solar wind exhibit non-thermal features such as: preferential heating of heavy ions [*Ogilvie et al.*, 1980; *Rosenbauer et al.*, 1981; *Bochsler et al.*, 1985; *Goldstein*, 1996; *Kohl et al.*, 1997; *Cranmer et al.*, 1998, 1999a, 2000a; *Goldstein and Neugebauer*, 2001; *Neugebauer et al.*, 2001; *Reisenfeld et al.*, 2001], differential ion-proton streaming [*Ryan and Axford*, 1975; *Neugebauer et al.*, 1994, 1996, 2001; *Gomberoff and Hernandez*, 1992; *Goldstein et al.*, 1995; *Goldstein*, 1996; *Esser et al.*, 1998; *Cranmer et al.*, 1999a; *Esser and Edgar*, 2001], temperature anisotropies in the distribution cores [*Marsch et al.*, 1981, 1982a, 1982b; *Marsch and Goldstein*, 1983; *Marsch*, 1984, 1991; *Bochsler et al.*, 1985; *Astudillo et al.*, 1996; *Kohl et al.*, 1997, 1998; *Cranmer et al.*, 1999a, b, 2000a; *Ofman et al.*, 2001; *Tanabe*, 2001], and proton and heavy ion heat conduction tails and secondary beams [*Feldman et al.*, 1973; *Ogilvie et al.*, 1980, 1993; *Marsch et al.*, 1981, 1982a, b; *Neugebauer*, 1981, 1992; *Marsch and Goldstein*, 1983; *Livi and Marsch*, 1987; *Marsch*, 1991; *Gomberoff et al.*, 1995; *Hammond et al.*, 1995; *Goldstein*, 1996]; see *Marsch* [1991] for reviews. It is reasonable to suggest that these non-thermal features are caused by resonant ion-cyclotron wave interactions that enhance particle velocity components perpendicular to the ambient magnetic field and accelerate particles parallel to the field

[*Hollweg and Turner*, 1978; *Dusenbery and Hollweg*, 1981; *Marsch et al.*, 1981, 1982a, b; *Rosenbauer et al.*, 1981; *Isenberg*, 1984, 2001a, 2001b, 2001c; *Tanaka*, 1985; *Esser et al.*, 1987; *Demars and Schunk*, 1990; *Gomberoff and Elgueta*, 1991; *Gomberoff and Hernandez*, 1992; *Astudillo et al.*, 1996; *Cranmer et al.*, 1997, 1999a, 1999b; *Marsch and Tu*, 1997; *Tu and Marsch* 1997, 2001; *Leamon et al.*, 1998; *Marsch*, 1998; *Hollweg*, 1999a, 1999b, 1999c, 2000; *Hu and Habbal*, 1999; *Kaghashvili*, 1999; *Li et al.*, 1999; *Li and Habbal*, 1999; *Ventura et al.*, 1999; *Cranmer*, 2000; *Cranmer et al.*, 2000a, 2000b; *Isenberg et al.*, 2000, 2001; *Hollweg and Markovskii*, 2001; *Ofman et al.*, 2001]. Observations of increasing ion magnetic moments at distances of many solar radii [*Marsch et al.*, 1981, 1982a, 1982b; *Marsch*, 1983, 1984, 1991; *Marsch and Livi*, 1987; *Marsch and Tu*, 2001] suggest that ion-cyclotron interactions continue in the solar wind far from the collisional regime in the low corona; see also *Cranmer* [2001].

Some heavy ion species have much higher observed kinetic temperatures in the direction perpendicular to the ambient magnetic field [*Dodero et al.*, 1998; *Cranmer et al.*, 1999a; *Antonucci et al.*, 2000; *Ofman et al.*, 2001] than protons and flow outward from the Sun with bulk speeds that exceed the average proton speed [*Kohl*, 1998]. Data unambiguously demonstrating ion-proton differential streaming were obtained with the solar wind plasma experiment aboard the Ulysses spacecraft. *Neugebauer et al.* [1994, 1996] examined the dependence of $V_{ap} \equiv \mathbf{V}_\alpha - \mathbf{V}_p$ and V_{ap} / V_A on heliocentric distance, r, and heliographic latitude using data obtained while Ulysses ranged between 1.15 and 5.4 AU from the Sun. Here, V_α and V_p are alpha particle and proton bulk speeds in the

heliocentric frame, and V_A is the Alfvén speed. They show that V_{ap} decreases approximately as r^{-1} and that V_{ap} / V_A is of order unity and is approximately constant for much of the radial distance studied, suggesting that the differential alpha-proton speed is regulated by local interactions with waves. The combination of wave-ion interactions, which preferentially enhance ion velocity components perpendicular to the ambient magnetic field, with the net radial force (comprised of the electrostatic force, gravity, and the mirror force) may act to preferentially accelerate ions. Since the mirror force is proportional to ion mass and the square of the ion perpendicular velocity; if ions are more than mass proportionally hotter than protons, they will be preferentially accelerated. Moreover, the waves themselves accelerate particles along the ambient magnetic field.

Recent observations of the solar corona obtained with the UVCS (UltraViolet Coronagraph Spectrometer) and SUMER (Solar Ultraviolet Measurement of Emitted Radiation) instruments aboard SOHO (Solar and Heliospheric Observatory) [*Kohl et al.*, 1997, 1998; *Cranmer et al.*, 1999a, b] reveal compelling evidence of greater-than-mass-proportional heating of O^{5+} ions compared with protons. Oxygen, clearly, and possibly proton distributions exhibit $T_\perp > T_\parallel$ temperature anisotropies, where $\perp$ and $\parallel$ indicate directions perpendicular and parallel to the ambient magnetic field direction, respectively; see also *Dodero et al.* [1998] and *Antonucci et al.* [2000]. *Cranmer et al.* [1999a] suggest that Coulomb collisions are sufficient to couple particles and are responsible for the observed ion UV lines low in the corona, but resonant wave-particle interactions are the likely cause of anisotropic ion heating in the collisionless regions of the corona and fast solar wind. They conclude that the required high-frequency resonant waves must be

generated over distances of many solar radii since these waves damp rapidly but perpendicular heating is observed to continue. Turbulent cascades of wave energy from low frequencies to high resonant frequencies or instabilities are suggested as possible mechanisms to produce the required high frequency waves over extended distances; see also *Hollweg* [1986], *Hollweg and Johnson* [1988], *Isenberg* [1990], and *Markovskii* [2001]. *Axford and McKenzie* [1992, 1996] and *McKenzie and Axford* [2001] suggest that high frequency waves might be launched as a result of reconnection events occurring in the corona thus obviating the requirement of a turbulent cascade.

Double beams consist of a core distribution of protons traveling at essentially the solar wind speed and a secondary distribution traveling faster than the core by approximately the Alfvén speed. Using data acquired with the electrostatic analyzer aboard Imp 6, *Feldman et al.* [1973] first reported the existence of proton double beams in the solar wind and suggested they might simply be interpenetrating plasma streams having different bulk speeds. More recently, *Feldman et al.* [1993, 1997] and *Hammond et al.* [1995] speculate that double beams might form due to reconnection-driven impulsive jets. Alternatively, recent theoretical models suggest that proton double beams can result when non-resonant forces (gravity, ambipolar electric field, and magnetic mirroring) are combined with resonant interactions between ions and both inward and outward propagating Alfvén waves [*Tam and Chang*, 1999; *Isenberg*, 2001c].

Rosenbauer [1981] and *Marsch et al.* [1981, 1982a, b] present examples of proton double beams from Helios data which include examples of core temperature anisotropies

of $T_\perp > 4T_\parallel$. In a comprehensive review of the kinetic physics of solar wind particles, *Marsch* [1991] presents Helios observations of alpha particle double beams in slow (speed < 400 km/s) solar wind and proton double beams in intermediate (400 km/s < speed < 600 km/s) and fast (speed > 600 km/s) solar wind for $0.3 < r < 1$ AU. The velocity difference between secondary and core proton peaks is close in magnitude to the local Alfvén speed, with the secondary peak moving faster than the core distribution. In contrast, velocity distributions of slow solar wind, where collisions are more important, are usually isotropic and seldom show secondary proton peaks or high velocity tails [*Marsch et al.*, 1982a, b, *Marsch*, 1991; *Goldstein*, 1996]. Roughly 25% of solar wind proton distributions observed with Helios had clearly resolved secondary peaks.

Observations of proton double beams associated with the heliospheric current sheet were obtained from Ulysses data [*Hammond et al.*, 1995]. High-speed wind containing secondary proton beams also exhibited enriched helium abundances, suggesting that the beams are formed in the corona where abundances are determined, rather than interplanetary space. Speeds of secondary beams relative to core distributions of protons are not observed to exceed $2V_A$. The beam/core relative velocity is observed to decrease as r increases, as does $V_A(r)$, suggesting an on-going wave-particle interaction.

Despite the variety of non-thermal solar wind features, until fairly recently most attempts to model ion heating and solar wind acceleration have assumed a form for ion distribution functions rather than calculate them directly. Early theoretical attempts by *Hollweg and Turner* [1978] and *Dusenbury and Hollweg* [1981] integrated resonant

wave-particle interactions with non-resonant forces but assumed Maxwellian ion velocity distributions to close the fluid equations. The earlier effort considered outward-propagating, left-hand polarized (LHP), non-dispersive waves and achieved reasonable values of $|\mathbf{V}_\alpha - \mathbf{V}_p| \approx V_p$ and $|\mathbf{V}_\alpha - \mathbf{V}_p| \approx V_A$ at 1 AU, in qualitative agreement with observations. However, the alpha particles were treated as test particles, so their contribution to the energy and momentum balance was neglected. *Dusenbery and Hollweg* [1981] predicted greater-than-mass-proportional ion heating when wave dispersion was included. The first energetically self-consistent model of a three-fluid supersonic solar wind [*Isenberg and Hollweg* 1983] incorporated outward, parallel-propagating, LHP, non-dispersive waves and assumed a cascade of wave power from low non-resonant frequencies to high resonant frequencies. They achieved ion flow speeds higher than proton flow speeds at 0.3 AU, but only with the inclusion of excessively steep wave power spectra. *Isenberg* [1984] improved this model by including wave dispersion and thermally anisotropic velocity distribution functions. A steep wave power spectrum was again required for predictions to match observations, but the inclusion of an anisotropic distribution function coupled with non-dispersive waves resulted in higher alpha-proton differential speeds.

In the first paper to apply these ideas to the corona, *Hollweg* [1986] considered a self-consistent calculation of a turbulent cascade of wave power from low frequencies to high frequencies. Hollweg obtained either: a high solar wind speed and low coronal base pressure, or with different parameters, a higher coronal base pressure, but slow solar wind speed. No combination of parameters was able to provide a set of predictions in complete

agreement with observations of the time, although it now appears that the coronal base pressures are in fact quite low [*Esser et al.*, 1999; *Kohl et al.*, 1999]. *Hollweg and Johnson* [1988] again considered a turbulent cascade of wave energy and predicted hot coronal protons ($T > 3 \times 10^6$ K) near $3R_s$ (R_s = solar radius) that were not observed at the time of publication but have since been reported by *Kohl et al.* [1998] from UVCS SOHO data. *Isenberg* [1990] extended the theory of *Hollweg and Johnson* [1988] to include alpha particles in the dispersion relation, and also predicted hot coronal protons near $3R_s$. *Isenberg* [1990] was the first to show both $V_\alpha > V_p$ and $T_\alpha > 4T_p$ in the corona, thus anticipating the UVCS SOHO results.

Further improvements in fluid models were made by *Hu et al.* [1999], and *Hu et al.* [2000]. *Hu et al.* [1999] determine self-consistently the evolution of the wave spectrum and ion distribution functions for a three-fluid model consisting of electrons, protons, and alpha particles interacting with dispersive, LHP, parallel-propagating ion-cyclotron waves; see also *Hu and Habbal* [1999]. *Hu et al.* [2000] perform a similar calculation with O^{5+} as the fourth fluid and conclude that the greater the number of species in the dispersion relation the greater the preferential heating of heavy ions, but low abundance heavy ions have little effect on proton acceleration. In both works they obtain ion speeds larger than the proton bulk speed and $T_i/T_p \sim m_i/m_p$ within a few solar radii, in general agreement with observations of ion differential streaming and kinetic temperatures observed with SOHO. However, the models fail to reproduce the observed values of T_i/T_p near 1 AU.

Marsch and Tu [1997] and *Tu and Marsch* [1997], following a suggestion of *Axford and McKenzie* [1992, 1996], developed two-fluid models based on the assumption that the Sun launches a spectrum of high-frequency waves which become proton resonant in the corona. The wave spectrum is postulated to contain sufficient energy to heat coronal holes and drive the high-speed solar wind; see also *Czechowski et al.* [1998].

Most attempts to predict phenomena such as preferential acceleration and heating evoked fluid models and used either standard velocity distributions or empirically determined functions to close the fluid equations. *Hollweg* [1999a, b, c, 2000] created kinetic theory approaches that used particle proxies for the resonant and non-resonant portions of the solar wind. These models were generally successful in reproducing the observed proton effective temperatures close to the Sun [*Kohl et al.* 1998], and greater than mass-proportional heating of O^{5+}. They also, through the action of the mirror force, gave differential O^{5+}-proton streaming. However, they fail to reproduce the monotonic rise of the O^{5+} temperature throughout the entire observed range of r [*Kohl et al.*, 1998; *Cranmer et al.*, 1999b]. *Tam and Chang* [1999] developed a model of kinetic wave-particle resonant interactions in the solar wind with ions subject to an ambipolar electric field, gravity, Coulomb collisions and mirroring by the ambient magnetic field. Their model follows the evolution of the ion distribution function within an inhomogeneous magnetic field, incorporates local ion heating, and the ambipolar electric field is calculated self-consistently. They show for the first time that proton double beams can form when cyclotron interactions with both inward and outward waves are included.

Isenberg [2001a, b] and *Isenberg et al.* [2000 and 2001] obtain a numerical solution of the gyrophase-averaged guiding center equation for protons resonantly interacting with a spectrum of non-dispersive outward-propagating ion-cyclotron waves. Their calculations follow the kinetic evolution of coronal protons in response to the waves, gravity, the ambipolar electric field, and mirroring in a radially diverging magnetic field. They determine the evolution of the proton distribution function self-consistently. Strong perpendicular heating and rapid acceleration are predicted but the velocity distributions are unstable to the growth of inward-propagating waves, which are included in *Isenberg* [2001c]. The main effect of including inward propagating waves was the creation of a halo distribution of protons in the antisunward half of velocity space. *Isenberg* [2001c] showed that this halo population is necessary for the acceleration of the bulk proton distribution, but unrealistically high speed halo protons result.

Including wave dispersion, see *Isenberg and Lee* [1996]. *Isenberg* [2002] predicts ion perpendicular cooling, rather than heating, and solar wind outflow speeds slower than that observed. He suggests that preferential acceleration of alpha particles, which constitute 20% of the solar wind momentum flux, may strengthen the inertial force on the protons, thus providing the additional acceleration necessary to predict reasonable fast solar wind speeds.

To date, attempts to determine ion velocity distributions based on kinetic theory [*Tam and Chang*, 1999; *Isenberg*, 2001a, b, c; *Isenberg et al.*, 2000, 2001] have been exclusively numerical, focused on the proton distributions, and have successfully

demonstrated the non-Maxwellian nature of the distributions driven by resonant wave-ion interactions. These numerical treatments have provided insights into the reasons for observed temperature anisotropies, and some models have predicted reasonable values of fast solar wind speeds.

In this work we develop a mostly-analytical kinetic theory approach to determine the distribution function of an arbitrary ion species under the assumptions that the solar wind and wave speeds remain constant. We couple kinetic theory with the cold, electron-proton dispersion relation to determine the ion-cyclotron resonance condition and assume that ions are only resonant with outgoing waves. See also the recent reviews by *Hollweg and Isenberg* [2002] and *Cranmer et al.* [2002] for alternate discussions of the physics underlying the resonant interactions with protons and heavy ions. These assumptions, particularly the use of constant solar wind speed, are serious, but the importance of applying kinetic theory to solve the problems described herein, and the significant results achieved, we believe, justifies our approach.

Following *Isenberg et al.*, [2000, 2001], the ion distribution function is taken to consist of two functions that describe the cyclotron-resonant (f_+) and non-resonant (f_-) ions of a particular species. We use the cold, electron-proton plasma dispersion relation to determine the boundary line in velocity space that separates the resonant from the nonresonant ions. In section 2.2.2 we provide a detailed discussion of the dispersion relation and Figure 2.1 depicts schematically the division of ions into resonant and nonresonant fractions. We include the effects of gravity, the ambipolar electric field, and

magnetic mirroring. We use the fact that cyclotron resonant pitch-angle scattering conserves ion kinetic energy in the wave frame. Our most important assumption is that pitch-angle scattering distributes resonant ions uniformly and instantly along arcs in velocity space (Figure 2.1). Further, we assume that sufficient wave power [*Yoon and Zibell* 1990; *Bird et al.*, 1991; *Gomberoff et al.*, 1996; *Verma et al.*, 1996; *Leamon et al.*, 1998; *Cranmer et al.*, 1999b; *Hu et al.*, 1999; *Ventura et al.*, 1999; *Cranmer* 2000; *Ofman et al.*, 2001] to provide efficient pitch-angle scattering is always available.

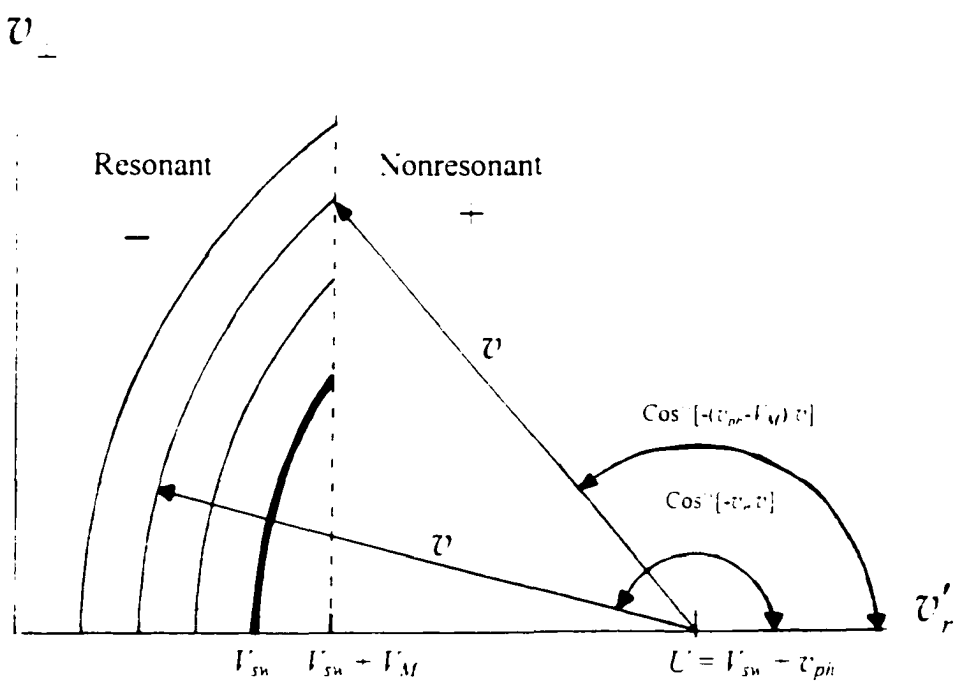

Figure 2.1 Schematic diagram of resonant ion energy shells (circular arcs centered on the wave speed U). In general, there is a continuum of energy shells, and the dark arc represents a generic delta function ion distribution. The straight arrows represent the wave-frame ion speed v, where v is constant on a given shell. The remaining velocity variables are defined in chapter 2.2.

We obtain exact analytical solutions for the distribution function of the nonresonant portion of ions and predominantly analytical solutions for the distribution function of the resonant portion of ion velocity space. We establish the approximation scheme to solve

the transport equation analytically for the resonant-ion distribution function in section 2.2.6. In chapter 2.3, we present contours of the ion distribution functions in velocity space for protons and heavy ions. These contours clearly show the non-thermal nature of the ion distributions and exhibit expected effects of the large-scale forces (gravity, ambipolar electric field, and magnetic mirroring) as radial distance increases. With the incorporation of the cold, electron-proton dispersion relation, we obtain differential ion-proton streaming and temperature differences between protons and heavy ions that favor the ions [*Kohl et al.* 1997, 1998; *Cranmer et al.*, 1999a, 2000a]. In chapter 2.4, we discuss possible future refinements. We describe in the Appendix the numerical method used to determine the resonant-ion distribution function in the small region of solution space inaccessible to an analytical solution.

The simple, analytical forms of the distribution functions presented here provide additional insights into the effects of cyclotron-resonant heating of ions compared with purely numerical calculations or calculations using assumed distribution functions.

CHAPTER 2.2

THEORY

2.2.1 Basic Equations

We begin with the stationary, gyrophase-averaged particle transport equation [*Skilling*, 1971; *Kulsrud*, 1983; *Isenberg*, 1997] assuming a radial ambient magnetic field, $\mathbf{B}(r) = B_0(r)\hat{e}_r$ (where we take $B_0 > 0$), constant radial solar wind, and constant wave speed:

$$(U + v\mu)\frac{\partial f}{\partial r} - \frac{\alpha GM}{r^2}\left[\mu\frac{\partial f}{\partial v} + \frac{(1-\mu^2)}{v}\frac{\partial f}{\partial \mu}\right] - \left[\frac{(1-\mu^2)U}{r}\right]\frac{\partial f}{\partial v}$$

$$+(1-\mu^2)\left[\frac{v+\mu U}{r}\right]\frac{\partial f}{\partial \mu} = \frac{\partial}{\partial \mu}\left[(1-\mu^2)D\frac{\partial f}{\partial \mu}\right]. \qquad (1)$$

The wave frame, in which ions scatter in pitch-angle only, has velocity $U = V_{sw} - v_{ph}$, where V_{sw} is the solar wind speed and v_{ph} is the wave phase speed. In equation (1), $f(r, v, \mu)$ is the distribution function of a particular ion species, v and μ are ion speed and cosine of pitch angle in the frame moving with speed U, D is the pitch-angle diffusion coefficient, G is the universal gravitational constant, and M is the solar mass. The terms of equation (1) from left to right describe convective transport, the deceleration of ions by an "effective" gravity (scaled by parameter α which we estimate below), adiabatic deceleration, magnetic focusing, and pitch-angle diffusion.

The effective gravitational field is a combination of the sunward gravitational field and the ambipolar electric field E_r. We may estimate the magnitude of E_r from the steady-state, spherically-symmetric momentum equations for electrons, ignoring electron mass,

$$0 = -\frac{\partial p_e}{\partial r} - en_e E_r, \tag{2a}$$

and for protons,

$$\rho V_{sw} \frac{\partial V_{sw}}{\partial r} = -\frac{\partial p_p}{\partial r} + en_p E_r - \rho \frac{GM}{r^2}. \tag{2b}$$

Here, n is number density, p is thermal pressure, ρ is proton mass density, e is the magnitude of the electron charge, and the subscripts e and p indicate electrons and protons, respectively. Since we assume a constant solar wind speed, we take the left side of equation (2b) to be zero for all r. Subtracting (2b) from (2a), and assuming electrons and protons contribute equally to the pressure, yields an electric field magnitude given by $eE_r = (1/2)GMm_p r^{-2}$, where m_p is proton mass. The r^{-2} dependence of the electric field agrees quantitatively with the self-consistent electric field calculated by *Tam and Chang* [1999]. The effective gravitational force may be written $-GMm_i r^{-2}(1 - q_i m_p / 2em_i)$, where q_i and m_i are ion charge and mass. Thus, the ambipolar electric field partially counteracts gravity and we may include its effect by taking $\alpha = (1 - q_i m_p / 2em_i)$.

2.2.2 Significance of Wave Dispersion

Despite taking v_{ph} to be constant in equation (1) for analytical simplicity, we must consider wave dispersion to establish if a given ion is resonant with outward-propagating proton-cyclotron waves. Ions diffuse in pitch-angle by scattering on waves only if they are in cyclotron resonance. We consider transverse waves propagating radially outward from the Sun which obey the approximate dispersion relation for a cold, electron-proton plasma as given by *Stix*, [1992]

$$\frac{\omega}{\Omega_p} = -\frac{1}{2}\left(kV_A/\Omega_p\right)^2 \pm \frac{1}{2}\left[\left(kV_A/\Omega_p\right)^4 + 4\left(kV_A/\Omega_p\right)^2\right]^{1/2} \qquad (3)$$

Here, ω and k are the wave frequency in the solar wind frame (taken to be the same as the average proton frame) and wavenumber, respectively. The Alfvén speed is $V_A = B_0/(4\pi\rho)^{1/2}$, $\Omega_p = eB_0/m_pc$ (here, we take $\Omega_p > 0$, see Figure 2.2) is the proton gyrofrequency, and c is the speed of light. Figure 2.2 depicts both branches of the dispersion relation for waves with $v_{ph} > 0$ [left hand circular polarization (LCP) is given by the upper sign in equation (3) and right hand circular polarization (RCP) by the lower sign]. An ion of species i with radial velocity component v_{rs} is cyclotron resonant with a wave specified by (k, ω) when

$$\omega(k) = kv_{rs} - \Omega_i \qquad (4)$$

is satisfied. Here, $\Omega_i = q_iB_0/m_ic$ is the ion cyclotron frequency, and v_{rs} is the ion radial velocity component in the solar wind frame. Equation (4) describes a family of straight

lines, where the three lines shown in Figure 2.2 are specific to He^{2+} ($\Omega_i/\Omega_p = 0.5$) as an example.

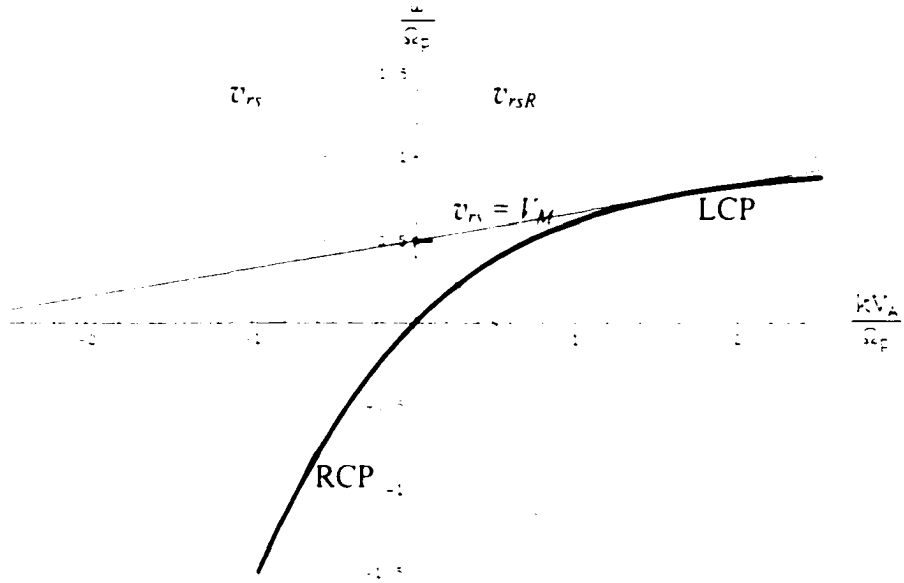

Figure 2.2 Electron-proton, cold plasma dispersion relation. An ion of a particular species with velocity component v_{rs} is cyclotron resonant with the wave specified by (k, ω) when $\omega(k) = kv_{rs} + \Omega_i$ is satisfied. This resonance condition is illustrated for He^{2+} where the maximum velocity of an ion resonant with LCP waves is designated by V_M. The minimum velocity of an ion resonant with RCP waves is given by v_{rsR}.

An ion species resonant with left-hand waves will have a maximum resonant velocity in the average proton frame, V_M, determined by the slope of the line tangent to the LCP portion of the dispersion curve as shown in Figure 2.2, and given by

$$\frac{V_M}{V_A} = -\kappa_0 + (2+\kappa_0^2)(4+\kappa_0^2)^{-1/2}, \qquad (5a)$$

where

$$\kappa_0 = \left[1/2\,\lambda(1-\lambda)^{-1}\left(4-\lambda+\left[\lambda^2+8\lambda\right]^{1/2} \right) \right]^{1/2}. \qquad (5b)$$

and $\lambda = (q_i/m_i)/(e/m_p)$. The ratio V_M/V_A is a monotonically decreasing function of increasing λ, approaching 1 for a massive ion ($\lambda \rightarrow 0$) and vanishing for protons ($\lambda = 1$). There is also a minimum resonant velocity (v'_{rsR}) for right-hand waves, determined from the steeper tangent line shown in Figure 2.2. These resonances require extremely fast ions, so we consider resonances with left hand waves only, and take V_M to be the maximum resonant velocity. Clearly, from Figure 2.2, there is no minimum resonant velocity for left-hand waves. See *Dusenbery and Hollweg* [1981], *Marsch et al.* [1982b], *Mckenzie and Marsch* [1982], *Hollweg* [1999a, b, c, 2000], *Cranmer et al.* [2002], and *Hollweg and Isenberg* [2002] for similar discussions of wave dispersion.

2.2.3 Radial Boundary Conditions on $f(r, v, \mu)$

Given the sharp distinction between resonant and nonresonant ions, we divide velocity space into two regions (Figure 2.1) designated by (+) for non-resonant ions ($D = 0$, $v'_r > V_{sw} + V_A$) and (-) for resonant ions ($D \neq 0$, $v'_r \leq V_{sw} + V_A$), where v'_r is the radial component of ion velocity in the Sun frame. This distinction requires that equation (1) be solved separately for f_+ and f_- subject to an appropriate boundary condition at $v'_r = V_{sw} + V_A$, which we consider in section 2.2.5.

Since v_{ph} is taken to be constant, resonant ions scatter in pitch-angle along circular arcs in velocity space described by [*Kennel & Engelmann, 1966*]

$$v_{\perp}^2 + v_r^2 = v^2, \tag{6}$$

where v^2 is constant. Here, v_r is the radial component of ion velocity in the wave frame and $v_{\perp}$ is the velocity component perpendicular to $\boldsymbol{B}_0$. We start the calculation at heliocentric radial distance $r = r_0$ where the ions are collisionless and have had sufficient time to scatter uniformly along the accessible arcs (which correspond to segments of spherical shells in three dimensional velocity space) shown in Figure 2.1. For $r > r_0$ we assume that the pitch-angle diffusion time scale ($\sim D^{-1}$) is much less than the wind propagation time scale ($\sim r/V_{sw}$). Thus we take $f_{\perp}$ to be independent of μ for $r > r_0$, with $f_{\perp}(r_0, v) = f_0(v)$. We consider two choices of $f_0(v)$: $f_0(v) \propto \delta(v - v_{ph})$, section 2.3.1, and a continuous extended function which we specify in section 2.3.2. The impulsive function (represented by the dark arc in Figure 2.1) has the advantage of simplicity, while the extended function is more general.

For simplicity we take $f_{\perp}(r_0) = 0$. For heavy ions with thermal velocities less than V_{sw} this choice is reasonable. For protons ($V_{sw} = 0$), this choice is formally valid only for $f_0(v) \propto \delta(v - v_{ph})$. For the extended form of $f_0(v)$, this choice is inconsistent with the formal requirement that the solar wind speed equal the average proton radial velocity. However, in equation (1) we take V_{sw} to be constant and since we neglect the inertial term which allows V_{sw} to equal the average proton velocity, V_{sw} does not remain equal to the average proton velocity even if they are equal at $r = r_0$, as in the case $f_0(v) \propto \delta(v - v_{ph})$.

Since this calculation makes a number of serious assumptions, its primary virtue in illustrating the essential behavior of the ion distributions in the solar wind frame is its simplicity. To that end we take $f_-(r_0) = 0$. Supporting this choice, we show in Chapter 2.4 that the radial evolution of f is somewhat insensitive to the condition imposed at $r = r_0$.

2.2.4 Solution for $f_-(r, v', \mu')$

Since ions with $v_r' > V_{sw} + V_A$ do not interact with waves, it is best to rewrite equation (1) in the Sun's frame and set $U = 0$. Defining a new independent variable

$$x = v_r'^2 r - 2\alpha GM, \tag{7}$$

equation (1) becomes

$$r^2 v_r' \frac{\partial f_-}{\partial r} + 2\alpha GM\left(x - \frac{1}{2}\right)\frac{\partial f_-}{\partial v_r'} - v_r' x r \frac{\partial f_-}{\partial x} = 0. \tag{8}$$

We may solve equation (8) for f_- by the method of characteristics, where the characteristic curves are specified by

$$\frac{dr}{r^2 v_r'} = \frac{dv_r'}{2\alpha GM(x - 1/2)} = \frac{dx}{-v_r' x r}. \tag{9}$$

Equation (9) yields two integrals

$$E = (1/2)v'^2 - \alpha GM r^{-1}, \tag{10a}$$

$$C = xr. \tag{10b}$$

Each integral specifies a family of surfaces in (v_r', x, r) space. The intersection of two of these surfaces specifies a characteristic curve along which E, C, and f_- are constant. E is

proportional to total ion energy and C is proportional to ion magnetic moment ($m_i v_\perp^2 / 2B_0$) since $x \propto v_\perp^2 r$ and $B_0 \propto r^{-2}$. Nonresonant ions move along these characteristic curves conserving their total energy and magnetic moment. In Figure 2.3 we plot four characteristic curves (solid lines) in $(v_\parallel', x, r)$ space and their projections onto planes $r = r_0$ (short dashes) and $v_\parallel' = V_{sw} - V_M$ (long dashes). The characteristic curves originate at $v_\parallel' = V_{sw} - V_M$ and form a family of curves for a continuum of values of $r/r_0 \geq 1$ and $x \geq 0$.

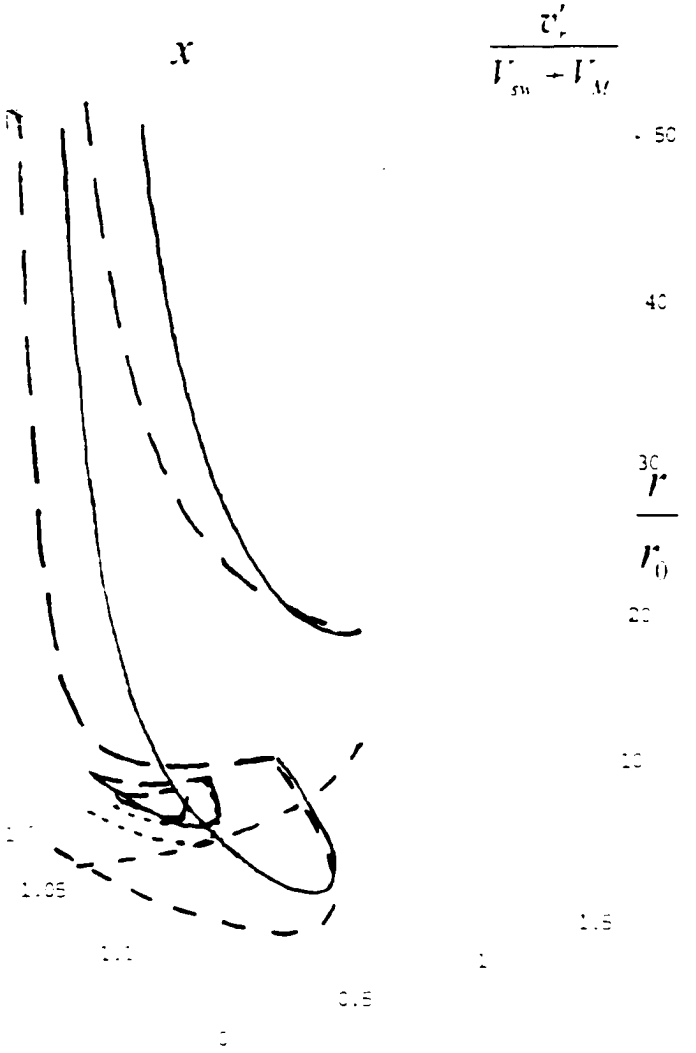

Figure 2.3 Characteristic curves of f_- in (x, v'_x, r)-space. Projections of characteristic curves into the $r = r_0$ plane are ellipse segments (short dashes) and projections of characteristic curves into the + - boundary plane (long dashes) are hyperbolae. An ion entering the (+) domain at $v'_x = V_{sw} - V_M$ and $x > 1$ never returns to the (-) domain.

Projections of characteristic curves onto the $r = r_0$ plane are ellipse segments that provide the circulation paths for nonresonant ions in velocity space as described in detail in section 2.2.5. The equation of the ellipses may be found by combining equations (7), (10a), and (10b) yielding

$$(x - 1/2)^2/b^2 + v_r'^2/a^2 = 1, \tag{11}$$

where $a^2 = 2E + v_\infty^2$, $b^2 = a^2 - 4v_\infty^2$, and $v_\infty^2 = \alpha GM/2C$. The maximum ($x'$) and minimum ($x''$) values of x on a given ellipse segment shown in Figure 2.3 are determined from equation (11) by setting $v_r' = V_{sw} + V_M$. We obtain

$$x' = 1/2 + (2v_\infty)^{-1}[2E + v_\infty^2 - (V_{sw} + V_M)^2]^{1/2}, \tag{12a}$$

$$x'' = 1/2 - (2v_\infty)^{-1}[2E + v_\infty^2 - (V_{sw} + V_M)^2]^{1/2}. \tag{12b}$$

Clearly, from equations (12a and b)

$$x' + x'' = 1, \tag{13}$$

so that the ellipses are symmetric about $x = 1/2$.

The projections of the characteristic curves onto the $v_r' = V_{sw} + V_M$ plane are hyperbolae given by equation (10b), with their endpoints determined by equations (12a) and (12b). It is evident from these hyperbolae that $r \to \infty$ as $x \to 0$, a limit which only occurs if $x' \geq 1$. Clearly from the projections in the $r = r_0$ plane the limit $x \to 0$ occurs for $v_r' \geq V_{sw} + V_M$; hence the radial velocity may approach a terminal value as $r \to \infty$. Setting $x = 0$ in equation (11) gives $v_r' = v_{r\infty}' = \sqrt{2E}$. Thus ion terminal velocities, which are governed by E, cover a range of values from $v_r' = V_{sw} + V_M$ to ∞ as is evident from the intersection points of the ellipses with the v_r' axis.

2.2.5 Boundary Condition at $v_r' = V_{sw} + V_M$

To establish the boundary condition at $v_r' = V_{sw} + V_M$ we write the first equality in equation (9) as

$$\frac{dv_r'}{dr} = \frac{2\alpha GM}{r^2 v_r'}\left(x - \frac{1}{2}\right). \tag{14}$$

Clearly $dv_r'/dr > 0$ if $x > 1/2$: the mirror force exceeds the effective gravity and ions are accelerated. Ions are extracted from the region $v_r' < V_{sw} + V_M$ and accelerated into the region $v_r' > V_{sw} + V_M$ by the mirror force. The extraction preserves the distribution function; thus for $x > 1/2$, $f_-(r, x, v_r' = V_{sw} + V_M) = f^-(r, x, v_r' = V_{sw} + V_M)$.

In contrast, $dv_r'/dr < 0$ if $x < 1/2$: the effective gravity exceeds the mirror force and ions are slowed from $v_r' > V_{sw} + V_M$ to $v_r' < V_{sw} + V_M$. These ions become a source of resonant ions, unrelated to the density of resonant ions already uniformly distributed in pitch angle on shell segments; therefore, $f_-(r, x, v_r' = V_{sw} + V_M) \neq f^-(r, x, v_r' = V_{sw} + V_M)$. Thus there is a circulation of ions with $1/2 < x < 1$ along characteristic curves as shown in Figure 2.3 from the (-) domain, through the (+) domain, and back to the (-) domain with $0 < x < 1/2$. Ions in the (-) domain with $x > 1$ can circulate into the (+) domain but they never return to the (-) domain. They escape the effective gravity and resonant interactions with the waves, and approach $v_{r\infty}' > V_{sw} + V_M$ as $r \to \infty$.

2.2.6 Solution of the Transport Equation for $f_-(r, v)$

For $r \geq r_i$, we assume that D is sufficiently large that f_- is independent of μ. Accordingly, we integrate equation (1) from $\mu = -1$ to $\mu = -(v_{ph} - V_M)/v + \delta$, where following the integration we let $\delta \to 0$. As evident from Figure 2.1, we integrate over the circular arcs. Since the upper limit of integration is a function of v, care must be exercised in integrating terms involving $\partial f/\partial v$. The purpose of introducing δ is to allow integration across the boundary between the (−) and (-) domains:

for $\mu = -(v_{ph} - V_M)/v + \delta$, $D = 0$, and $f = f_-(r, v_-, v_-' = V_{sw} + V_M)$. There results

$$\left(1 - \frac{v_{ph} - V_M}{v}\right)\frac{\partial f_-}{\partial r}\left\{U - \frac{v}{2}\left[1 - \frac{v_{ph} - V_M}{v}\right]\right\} -$$

$$-\left(1 - \frac{v_{ph} - V_M}{v}\right)\frac{\partial f_-}{\partial v}\left\{-\alpha\frac{GM}{r^2}\frac{1}{2}\left[1 + \frac{v_{ph} - V_M}{v}\right] + \frac{Uv}{r}\left[1 - \frac{1}{3}\left(1 - \frac{v_{ph} - V_M}{v}\right) + \frac{(v_{ph} - V_M)^2}{v^2}\right]\right\} -$$

$$-(f_- - f_-')\left\{-\alpha\frac{GM}{r^2}\frac{1}{v} + \frac{v}{r}\left[1 - \frac{(v_{ph} - V_M)^2}{v^2}\right]\right\} = 0. \qquad (15)$$

To obtain a semi-analytical solution to equation (15), we apply an approximation valid where the wave speed is much larger than the thermal speed and extend the formalism to radial distances where the approximation is not formally valid. We change variables to $\varepsilon = v - (v_{ph} - V_M)$ and assume $\varepsilon << V_{sw} - V_M, v_{ph} - V_M$. After expanding equation (15) in ε and keeping lead terms only, we obtain an equation that preserves the essential physics but is much simpler:

$$\varepsilon(V_{sw}+V_M)\frac{\partial f_-}{\partial r}-\varepsilon\left(-\frac{\alpha GM}{r^2}-\frac{U\varepsilon}{r}\right)\frac{\partial f_-}{\partial \varepsilon}+\left(-\frac{\alpha GM}{r^2}+\frac{2\varepsilon(v_{ph}-V_M)}{r}\right)(f_+-f_-)=0. \quad (16)$$

Terms neglected in this expansion are not essential to the structure of the equation. Thus, the solution of equation (16) appears to reveal the qualitative structure of the ion distribution even when the small ε approximation is not formally valid.

We rewrite equation (16) in a particularly simple form with the change of variables

$$x=(1-Q)v_{ph}\varepsilon r(\alpha GM)^{-1}, \quad (17a)$$

and

$$y=(r-r_0)^{q(1-Q)}(1-qQ), \quad (17b)$$

giving

$$xy\frac{\partial f_-}{\partial y}+x(1-x)\frac{\partial f_-}{\partial x}+(2x-1)(f_+-f_-)=0, \quad (18)$$

where $q=v_{ph}/V_{sw}$ and $Q=V_M/v_{ph}$. The variable y depends only on r and serves as our radial variable. The variable x, as defined by equation (17a), specifies resonant ion energy shells (x is constant on a given shell for a given r), and serves as our velocity coordinate; x is identical to x as defined by equation (7) only when $v'=V_{sw}+V_M$. However, equation (17a) incorporates the small v_- (small ε) approximation so that $(1-Q)v_{ph}\varepsilon \approx v_-^2/2$, establishing approximate equivalence of it and equation (7) for all v'. We take q to be independent of r, but the range of r considered will guide us in choosing values for q. Very close to the Sun, $q >> 1$ and at about 1 AU, $q \approx 0.1$ [*Hollweg*, 1999a, 1999b, 1999c, 2000; *Isenberg et al.*, 2000, 2001; *Isenberg* 2001a, b, c]. To evaluate Q, we write $Q=(V_M/V_A)/(v_{ph}/V_A)$ with (V_M/V_A) given by equation (5a). The dispersion relation depicted in Figure 2.2 suggests a reasonable, limited range for the wave phase

speed of $V_M < v_{ph} < V_A$, but since we take v_{ph} to be constant, we use the average of V_M and V_A to represent v_{ph}; hence, the value we use for v_{ph} depends on the ion species through V_M and represents the average phase speed sensed by an ion species over its resonant range. For protons $v_{ph} \cdot V_A = 1/2$, and for a massive ion $v_{ph} \cdot V_A \approx 1$. This choice for v_{ph} always results in $Q < 1$.

We solve equation (18) by the method of characteristics, where its characteristic curves are specified by

$$dx\, x(1-x) = dy\, xy = -df_- / (2x-1)(f_+ - f_-) \tag{19}$$

The first equality in equation (19) yields

$$A = y(1-x), \tag{20}$$

where A is a constant that specifies a particular characteristic curve. For $x > 1/2$, $f_+ = f_-$, as described in section 2.2.5, so that $f_-(y, x)$ is constant along each characteristic curve. For $x < 1/2$, $f_+ \neq f_-$; using the second equality in equation (19) we may write along a characteristic

$$\frac{dy}{xy} = \frac{df_-}{-(2x-1)(f_+ - f_-)}. \tag{21}$$

Rearranging equation (21), eliminating x with equation (20), and applying the integrating factor $(y-A)/y^2$ we obtain

$$f_-(y,x) = y^2(1-A)(y-A)^{-1} f_0(1-A) + y^2(y-A)^{-1} \int dy'' y''^{-3} (2A - y'') f_+(y'', x''), \tag{22}$$

where $x'' = 1 - A(y'')^{-1}$ from equation (20) and the integration must be performed along a characteristic curve specified by A.

We require the correspondence between f_+ and f_- to solve equation (22). At some radial distance, r', ions cross $v_r' = V_{sw} + V_{sf}$ with $x = x'$ and then return to $v_r' = V_{sw} - V_{sf}$ at a greater radial distance r'' with $x = x'' < x'$ as shown in Figure 2.3. Since f_+ is constant on characteristic curves in the (+) domain (Figure 2.3) and f is continuous for $x > 1$, we may write

$f_+(x'', r'', v_r' = V_{sw} + V_{sf}) = f_+(x', r', v_r' = V_{sw} + V_{sf}) = f_-(x', r', v_r' = V_{sw} + V_{sf})$. In terms of x and y, this continuity condition may be written as

$$f_+(y'', x'') = f_-(y', x'). \tag{23}$$

To determine the relationship between the primed and double-primed variables, we rewrite equation (10b) using equation (17b) and obtain

$$x'^{q(1-Q)/(1+qQ)} y' = x''^{q(1-Q)/(1+qQ)} y''. \tag{24}$$

Combining equations (24), (20), and (13) yields

$$y' = y''(y'' A^{-1} - 1)^{q(1-Q)/(1+qQ)}, \tag{25a}$$

and

$$x' = A y''^{-1}. \tag{25b}$$

Replacing $f_+(y'', x'')$ in equation (22) by $f_+\left[y''(y'' A^{-1} - 1)^{q(1-Q)/(1+qQ)}, A y''^{-1}\right]$ yields the integral equation

$$f_-(y, x) = y^2 (y - A)^{-1} (1 - A) f_0(1 - A) +$$

$$y^2 (y - A)^{-1} \int_1^{\cdot} dy'' y''^{-3} (2A - y'') f_+\left[y''(y'' A^{-1} - 1)^{q(1-Q)/(1+qQ)}, A y''^{-1}\right]. \tag{26}$$

Equation (26) is the implicit solution for $f\_(y, x)$ when $x < ½$. In the Appendix we discuss the structure of $f\_(y, x)$ and the method used to solve equation (26) numerically. Also in the Appendix and Chapter 2.3, we show that $f\_(y, x)$ may be determined for a large fraction of the solution space ($y > 1, x < ½$), and that much may be understood about the entire distribution function without having to solve the integral equation.

CHAPTER 2.3

RESULTS

We must specify a form for $f_0(x)$ to enable computation of $f_-(v_-,x)$. In the following subsections we consider separately the results of first taking f_0 proportional to a delta function and second letting $f_0(x)$ equal an extended function of x. The delta function form of f_0 has virtue because of its simplicity, whereas the extended f_0 is clearly more general. Either choice of f_0 provides useful insights into the evolution of ion distribution functions, ion-proton differential streaming, and the radial dependence of ion temperatures. In Chapter 2.4, we show that the sensitivity of $f_-(v_-,x)$ to the form of $f_0(x)$ diminishes as r increases.

2.3.1 Delta Function f_0

At $r = r_0$ the delta function boundary condition concentrates protons at the point $(v_r' = V_{sw}, v_- = 0)$ and each heavy ion species onto its unique energy shell in velocity space (dark arc in Figure 2.1). Shell endpoints occur at $(V_{sw}, 0)$ and $(V_{sw} + V_M, v_{-0})$, where V_M is given by equation (5), and the maximum v_- of ions on their delta function shell at r_0 is v_{-0} (see Figure 2.4). We determine v_{-0} from equation (6) with

$v_\perp' = v_{ph} - V_M$ and $v = v_{ph}$, yielding $v_{\perp 0}^2 = 2v_{ph}V_M(1 - V_M/2v_{ph})$, where $V_M = 0$ for protons. As ion mass/charge ratio increases, V_M and $v_{\perp 0}$ increase. Therefore, combining the kinetic shell model with the cold, electron-proton plasma dispersion relation builds-in at r_0 higher perpendicular temperatures and higher streaming speeds of heavy ions compared with protons. We show in following subsections that regardless of the form of $f_0(x)$ these non-thermal features persist for $r > r_0$.

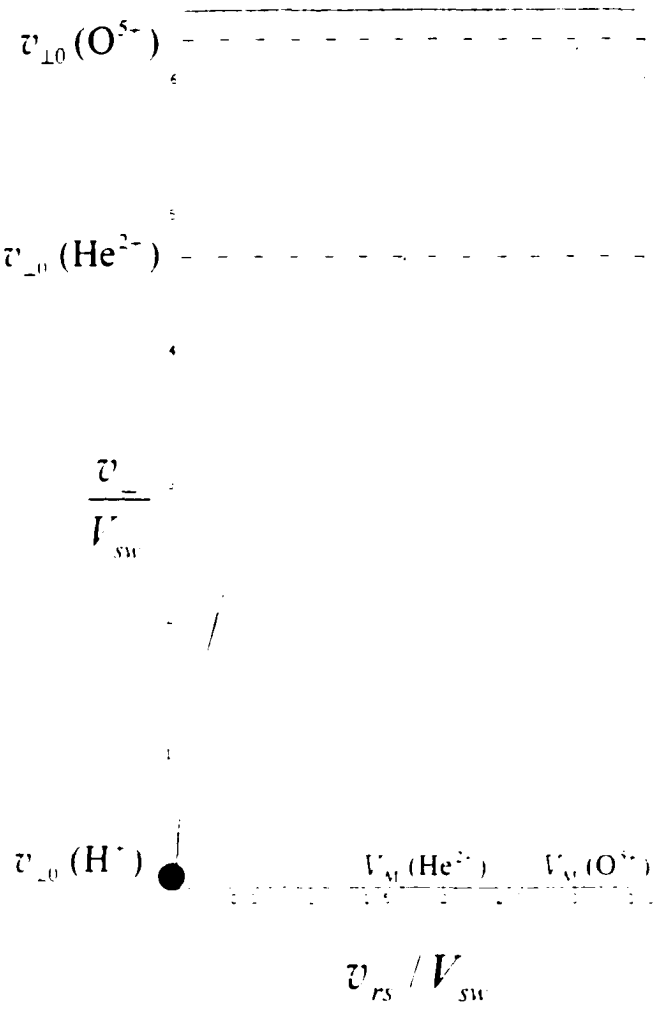

Figure 2.4 Constant energy shells at $r = r_0$ for protons, alpha particles, and O^{5+} ions. The maximum value of $v_\perp$ is $v_{\perp 0}$, which occurs when $v_{rs} = V_M$, where v_{rs} is ion radial velocity in the solar wind frame. The values of $v_{\perp 0}$ for each ion species are indicated by the dashed, horizontal lines, and the values of V_M are indicated by the dashed, vertical lines. $v_{\perp 0} = V_M = 0$ for protons. $V_4 = 1500\,\text{km/s}$ and $V_{sw} = 150\,\text{km/s}$.

A parameter related to $v_{\perp 0}$, which defines the x value of the initial energy shell unique to each species and which we use extensively to distinguish features of the solution for $f_\perp$ is x_0. Using equation (7) to transform the expression for $v_{\perp 0}^2$ to x_0 yields

$$x_0 = C_0 q^2 Q(1 - \tfrac{1}{2}Q)/\alpha , \qquad (27)$$

where $C_0 = V_{sw}^2 r_0 / GM$ is constant, but q, Q, and α are species dependent and $x_0 = 0$ for protons. The definitions of q and Q appear after equation (18). We showed in section 2.2.5, when $x \geq \frac{1}{2}$, ions must focus forward from the (-) domain into the (+) domain. From equation (20), we note that for any value of A, $x \to 1$ as $r - r_0 \to \infty$. Therefore, three cases must be considered separately: $x_0 < \frac{1}{2}$, $\frac{1}{2} < x_0 < 1$, and $x_0 > 1$.

$x_0 < \frac{1}{2}$

We depict the small-r evolution of the proton delta function shell in the (v', x) plane in Figure 2.5 by sketching the delta function shell at three values of r/r_0 for $V_A = 1500$ km/s, and $V_{sw} = 150$ km/s. The influence of the effective gravity averaged over a shell dominates magnetic mirroring for small x. The delta function shell is continually reformed at increasing v' as r increases; thus, the intersection point of this shell and the + - boundary (x_2) increases as r increases. When $r/r_0 = 1$, the shell is a point at $(V_{sw}, 0)$. Setting $x = x_2 = \frac{1}{4}$, in equation (20) and using this set of parameters gives $r/r_0 \approx 1.06$, and when $x_2 = \frac{1}{2}$, $r/r_0 \approx 1.15$. Once $x_2 = \frac{1}{2} - \delta$, ($\delta \to 0$) ions immediately circulate through the (+) domain and return to the (-) domain to scatter along the lower shell at $x_1 = \frac{1}{2} - \delta$. This process is indicated by the two closely spaced arcs in Figure 2.5. As V_A increases, the radial distance where x_2 reaches $\frac{1}{2}$ decreases. The value of x at every point on a shell is the same as the value of x at the intersection of that shell and the + - boundary and represents the energy of that shell through equation (17a).

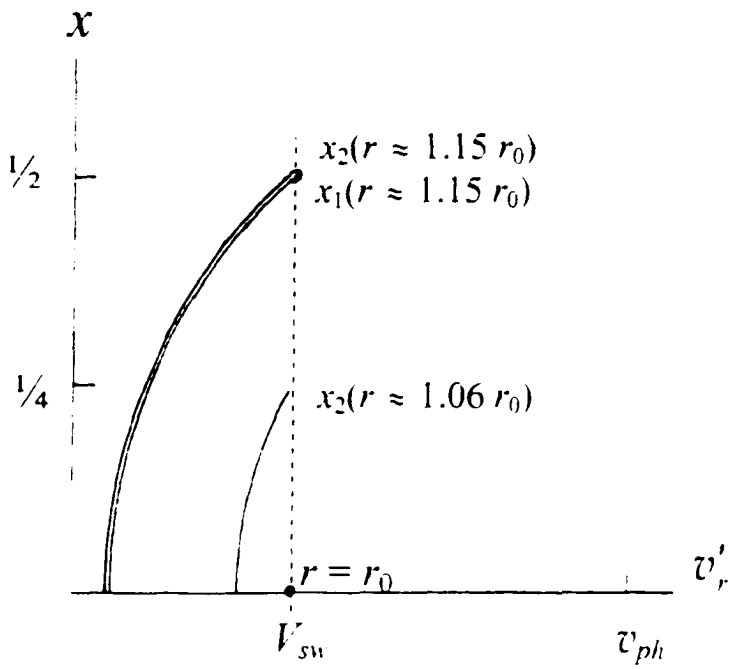

Figure 2.5 Evolution of the proton delta function shell at selected values of r/r_0. The lowest arc and the upper arc of the paired arcs represent the delta function shell at different values of r. At $r = r_0$ protons are at the point $(V_{sw}, 0)$. For the parameter set V_A = 1500 km/s and V_{sw} =150 km/s once r/r_0 = 1.15 protons achieve $x = 1/2$, which allows mirroring forward into the (+) domain. At $x = 1/2$ protons immediately circulate through the (+) domain and return to the (-) domain to scatter on the lower of the paired arcs (x_1).

The entire ion distribution is described by a delta function in v until $x = 1/2$, with r-dependent amplitude. Once x exceeds 1/2, the ion distribution will consist of a continuous part plus a delta function shell of constant amplitude. For $x < 1/2$ we determine the r-dependent amplitude of the delta function by setting $f_-(v, x)$ equal to the first term in equation (26) ($f_+ = 0$) and $n(r) = \int d^3v f_-$, where $n(r) = n_0(r_0/r)^2$ is ion number density, and n_0 is the number density at r_0. See the Appendix section A.1 where, consistent with the small ε approximation, we show that equations (8) and (18) conserve number flux, thus yielding $n(r) = n_0(r_0/r)^2$. Performing the integration subject to the small ε approximation ($v \approx v_{ph} - V_M$) gives

$f_-(v, x < 1\ 2) = [v/(x_0 - v - 1)]n_0 r_0^2 (v_{ph} - V_M)\delta[x - (x_0 - v - 1), v] \cdot 2\pi(\alpha GM)^2$. For protons $x_0 = V_M = 0$, so the factor $v/(x_0 - v - 1)$ renders $f_-(v, x)$ for protons doubly singular at $v = 1$.

We further examine the radial evolution of f in Figure 2.6. The ellipses (dashed curves) shown in Figures 2.3 and 2.6 are projections of the characteristic curves of f_- into the (v', x) plane. Curve 2 is the delta-function shell (highest energy in the wave-frame, $x = x_2$) and curve 1 is the shell populated by ions just returning to the (-) domain from the (−) domain (lowest wave-frame energy shell, $x = x_1$). At $r = r_0$, $x = x_0$, so from equation (20) $A(v = 1) = 1 - x_0$. Setting $A = 1 - x_0$, in equation (20) yields

$$x_2(r) = 1 - (1 - x_0)(r\ r_0)^{-q(1-Q)/(1+q)} \quad (28a)$$

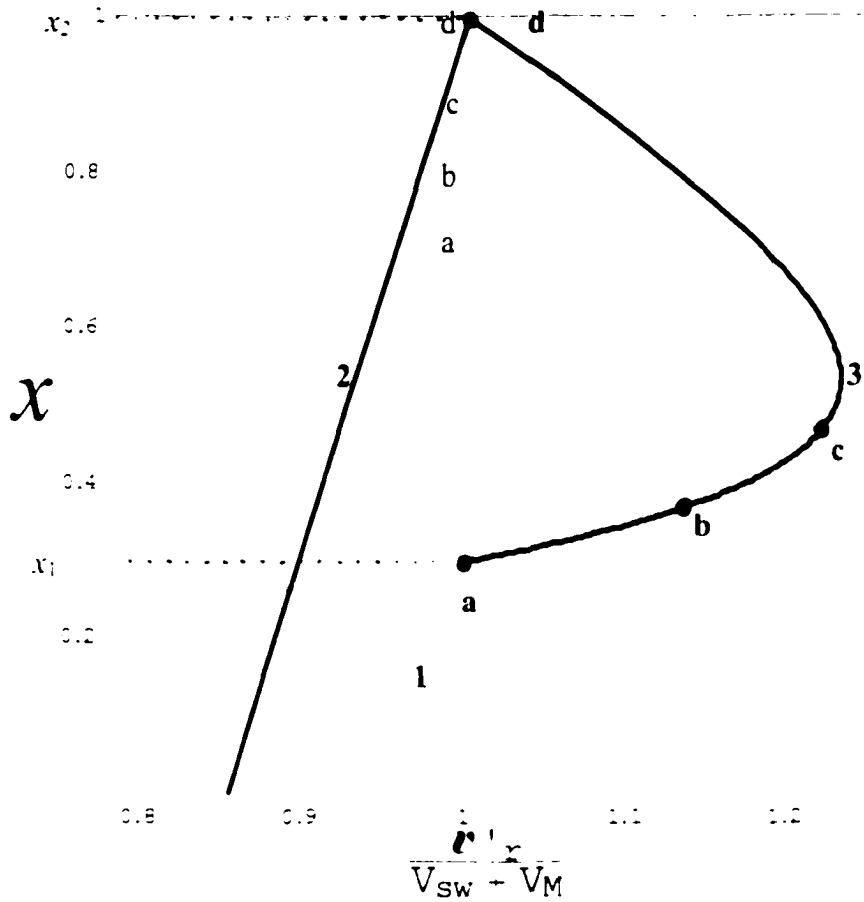

Figure 2.6 Projected characteristics of f- (ellipses) and boundary curves (1 – 3) in (v', x) space. Within the region bounded by curves 1 – 3, f is continuous, and outside the region $f = 0$. Curve 2 is the delta function shell, curve 1 is the shell formed by ions just returning to the (-) domain from the (−) domain and curve 3 is a boundary that indicates the progress of ions along the elliptical paths. Points **a** – **d** mark the progress of ions along correspondingly-labeled ellipses. V_A = 1500 km/s, V_{sw} = 150 km/s, and $r = 6R_s$. The dark curves (2 and 3) indicate the singular part of the velocity distribution.

During the time ions circulate through the (+) domain, x_2 increases; ions are continuously extracted at the +/- boundary at $(x_1 > \frac{1}{2}, r_1)$, circulate along their elliptical trajectories through the (+) domain, and return to the +/- boundary at $(1 - x_1, r > r_1)$. An ion returning to the (+/-) boundary at x_1 and r was extracted at the (+/-) boundary at $1 - x_1$ and r_1. So equation (28a) may be written as $1 - x_1 = 1 - (1 - x_0)(r_1 / r_0)^{-q(1-Q)/(1+qQ)}$. Similarly, equation

(10b) may be written as $(1-x_1)r_i = x_i r$. Combining these two equations by eliminating r_i yields the implicit equation for $x_i(r)$

$$x_i[x_i/(1-x_i)]^{q(1-Q)/(1+qQ)} = (1-x_0)(r - r_0)^{-q(1-Q)/(1+qQ)}, \qquad (28b)$$

where from equation (28a) we require $r - r_0 \geq [2(1-x_0)]^{(1+qQ)/q(1-Q)}$ to ensure $x \geq x_2$.

The equation of either curve 1 or 2 is found by combining equations (6) and (7) yielding

$$x(v_r') = -(r - 2\alpha GM)[V_{sw} + v_{pu} - v_r']^2 + rv^2 - 2\alpha GM, \qquad (29)$$

where we transformed from the wave frame to the Sun frame using $v_r = V_{sw} + v_{pu} - v_r'$. Equation (29) is a family of parabolas that represent a continuum of resonant ion energy shells, each specified by a different value of v at a given value of r r_0, where on a specific shell v is constant. The value of v for curve 1 (2) is determined by setting $x = x_1$ (x_2) and $v_r' = V_{sw} + V_M$, where x_2 and x_1 are given by equations (28a and b). Doing this yields $v_{1,2}^2 = 2\alpha GMx_{1,2}r^{-1} + (v_{pu} - V_M)^2$. Since $v_{1,2}$ is constant on a shell, $x_{1,2}$ is also constant on that same shell, as previously stated.

As r and x_2 increase, the radial distance required for an ion to completely circulate through the (+) domain increases. At a given r there will be a continuous variation of relative progress of ions along their respective ellipses, ranging from zero advancement at $(V_{sw} + V_M, x_2)$ to completed circulation at $(V_{sw} + V_M, x_1)$. The locus of points (v_r', x) that mark the extent of circulation of ions along the ellipses forms a continuous curve in the (+) domain (curve 3). Thus, curve 3 is a boundary that identifies the radial velocity of nonresonant ions at a specific r for each value of x at extraction and represents the

singular part of the nonresonant ion velocity distribution. Therefore, any point in the region to the right of curve 3 is not accessible to ions at the specified value of r. The ion distribution is continuous inside the region bounded by curves 1 - 3 and vanishes outside the region bounded by these curves.

We determine the analytical form of curve 3 from equations (10b), (17b), and (20), giving

$$x = x'[(1 - x_0)/(1 - x')]^{[1+qQ)/q(1-Q)]}(r/r_0)^{-1} \quad (30)$$

Here, x locates the intersection of curve 3 with an ellipse that intersects the +/- boundary at x' [equation (12a)], and $v'_{\perp}(x)$ is determined from equation (11). Intersection points along curve 3 labeled **a** – **d** mark the progress of ions along correspondingly-labeled ellipses, where the location of each point is determined from equation (30). In Figure 2.6 the parameters are the same as those used in Figure 2.5. An ion extracted at ellipse "a" will just complete its circulation through the (+) domain at this r; hence intersection point **a** is located at the lower ends of both ellipse "a" and curve 3 and at the +/- boundary. Ions that follow ellipses "b" and "c" have moved less "distance" along curve 3 and ions are just being extracted at ellipse "d" at this value of r. As $r \to \infty$, $x_1 \to 0$ and $x_2 \to 1$, so all ions eventually return to the (-) domain.

Contours of $f(v'_{\parallel}, v'_{\perp})$ for protons are shown in Figure 2.8, where f is plotted for $r = 3R_s$ in Figure 2.8a and $r = 5R_s$ in Figure 2.8b. To find $f(v'_{\parallel}, v'_{\perp})$, we must first solve equation (26) for $f_-(y, x)$, then transform from (x, y) to $(r, v'_{\parallel}, v'_{\perp})$ through equations (6) and (17). To determine f_-, we invoke the continuity of f at the +/- boundary and the

constancy of f_- along characteristics. All values of f are normalized to the maximum value calculated, so that the maximum value of f in a contour plot is 1 and f is dimensionless. The grayscale of the contour plots is shown in Figure 2.7. The contours are differentiated by 10 shades of gray, where if a value of f falls below 0.1, the region appears white. A detailed description of the structure of $f_-(v,x)$ and the methods used to obtain the analytical and numerical solutions for f_- appear in section A.2 of the Appendix.

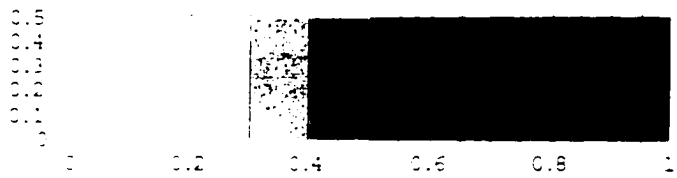

Figure 2.7 Contour plot gray scale key. Any values less than 0.1 are white.

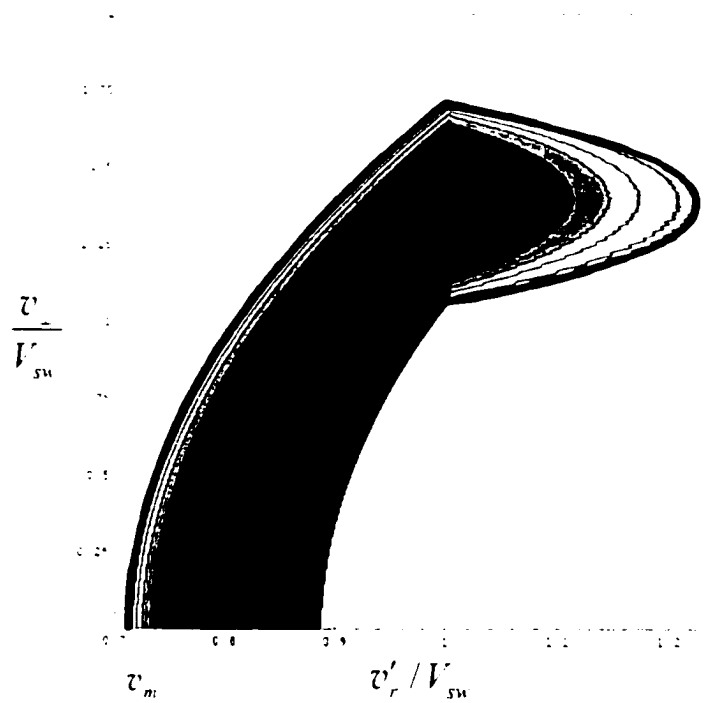

Figure 2.8a Proton distribution function contours in velocity space for $r = 3R_s$. $V_A = 1500\,\text{km/s}$, $V_{sw} = 150\,\text{km/s}$.

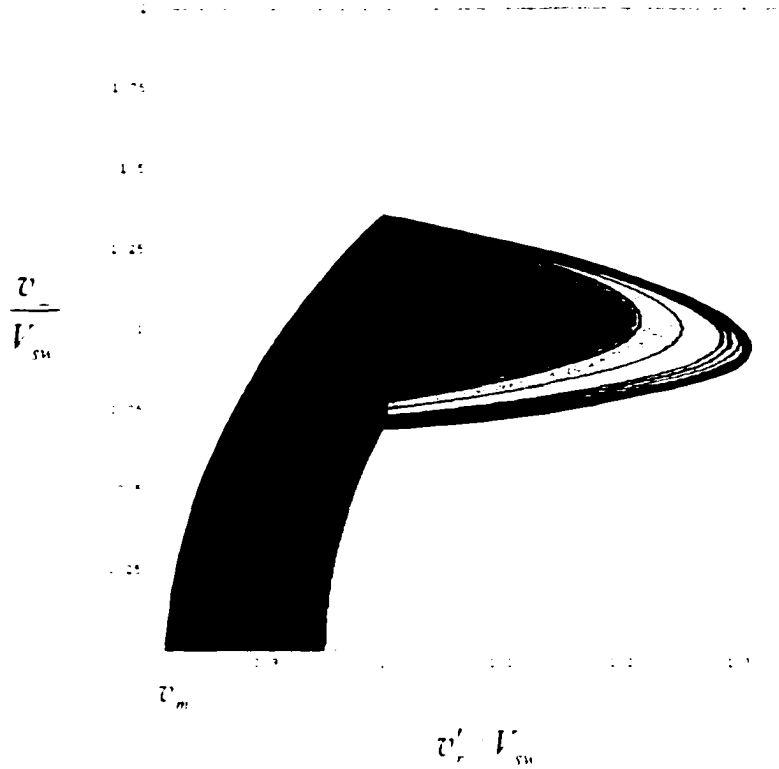

Figure 2.8b Similar to Figure 2.8a except here $r = 5R_s$. A comparison of figures a and b illustrates the shift of the contours of f_- toward V_{sw} and the reduction in perpendicular velocity due to the ongoing effect of adiabatic cooling as r increases.

In Figure 2.8c we plot contours of a bi-Maxwellian distribution with $T_- / T_+ = 5$ for comparison to the computed proton distribution functions. Comparing Figure 2.8c to either Figure 2.8a or 2.8b shows that the ion distribution function we calculate is clearly not Maxwellian. The general shape and proportions of the contours of f shown in Figures 2.8a and 2.8b are similar to those obtained by *Isenberg* [2001a] and *Isenberg et al.* [2000, 2001].

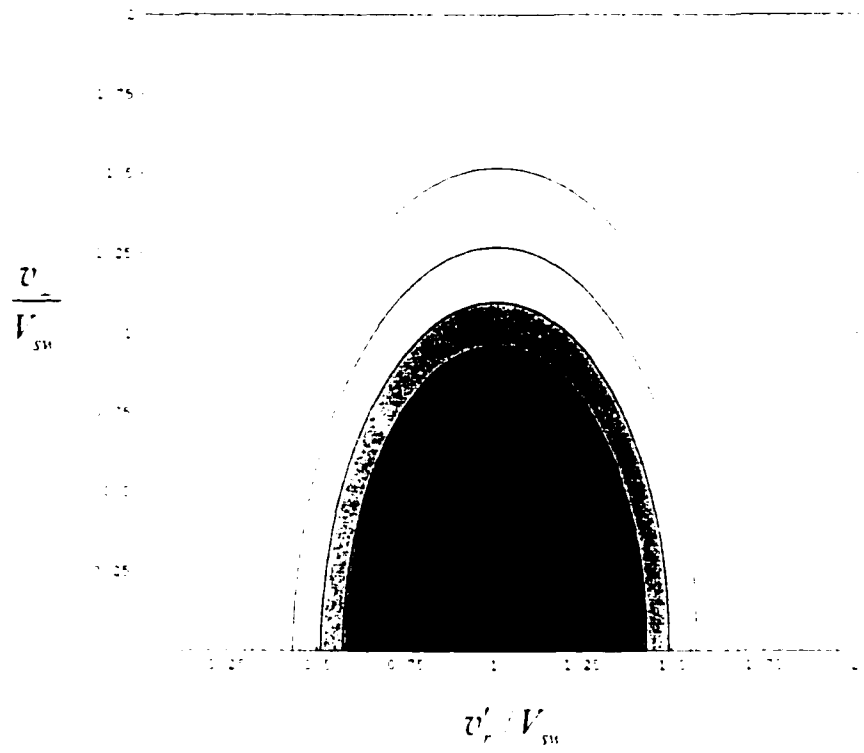

Figure 2.8c. Contour lines of a bi-Maxwellian velocity distribution with $T_{\perp} = 5T_{\parallel}$.

The dark curve outlining the distribution in Figures 2.8a and 2.8b represents the delta function shell. Since the delta function shell provides a sharp boundary between regions of zero and nonzero f, v_m labels the minimum value of v'_r for the distribution. The large value of f_- near $v'_r / V_{sw} = 1$ results from the flow of ions into the (-) domain from the (+) domain due to the dominance of the effective gravity at small $v'_{\perp}$. The rapid decrease of f_- as $v'_r \rightarrow v_m$ becomes more dramatic as r increases due to ongoing magnetic mirroring and the more-rapidly decreasing effective gravity. The effective gravity slows ions to lower v'_r while the mirror force combined with pitch-angle scattering of ions by waves

increases $v_{\perp}'$. Also, v_m increases as r increases as is evident when comparing Figure 2.8a with Figure 2.8b. This motion of extremes of energy shells in opposite directions in velocity-space causes shells to converge toward a single energy shell. This effect is analogous to the creation of the "pile up" shell described by *Isenberg* [2001a] and *Isenberg et al.* [2000, 2001].

Continuity of f at the + - boundary is apparent by the continuity of contour lines across the (+ -) boundary. The circulation point on the (+ -) boundary ($v_{\perp}$ $V_m \approx 1.25$ in 2.8a and $v_{\perp}$ $V_m \approx 0.95$ in 2.8b) moves to lower $v_{\perp}$ as r increases because of the relative decrease of the magnitude of the effective gravity compared with the mirror force. The extent in $v_{\perp}$ of the entire distribution is decreasing as r increases due to ongoing adiabatic cooling and the width in $v_{\parallel}'$ of the resonant part of the distribution decreases as r increases due to the increasingly dominant mirror force compared with the decreasing effective gravity.

We plot proton parallel and perpendicular temperatures as a function of radial distance scaled by the solar radius in Figure 2.9. The perpendicular to parallel temperature anisotropy, also given as a function of r/R_s, is plotted in Figure 2.10. Perpendicular and parallel ion temperatures as a function of r may be calculated by taking moments of $f(v_{\parallel}', v_{\perp}, r)$. By definition

$$T_{\perp} = m_i \langle v_{\perp}^2 \rangle / 2k_B \tag{31a}$$

and

$$T_{\parallel} = m_i \langle (v_{\parallel} - V_{\parallel})^2 \rangle / k_B, \tag{31b}$$

where $\langle\ \rangle$ denotes an average, V_i is average parallel flow speed, and k_B is Boltzmann's constant. The average of a generic quantity ψ is found from $n\langle\psi\rangle = \int d^3v \psi f$, where n is ion number density. Since we calculate f at discrete points in velocity space, summations replace the integrations.

The proton distribution occupies the point (0,0) in the solar wind frame in velocity space at r_0; therefore, $T_\perp(r_0) = 0$. The perpendicular temperature rises to a maximum of approximately 1.8×10^6 K by approximately $2.5R_\odot$, then slowly drops as r increases. This rapid rise in temperature is artificial due to our choice of boundary condition. Although the values of $T_\perp$ are of the correct order of magnitude, they are too small by a factor of roughly two, and the decrease of $T_\perp$ with increasing r disagrees with observations [*Kohl et al.*, 1998; *Cranmer et al.*, 1999b] that indicate that proton temperatures remain fairly constant in the range $1.5R_\odot < r < 4R_\odot$. The parallel temperatures are quite low and after an early rise, decrease as r increases, which agrees qualitatively with *Hollweg*, [1986], *Dusenbery and Hollweg*, [1981], *Li et al.*, [1999], *Isenberg et al.*, [2000, 2001], and *Hollweg and Isenberg*, [2002]; consequently, the calculated temperature anisotropy is very large. However, observations [*Kohl et al.*, 1998, *Cranmer et al.*, 1999b, *Antonucci et al.*, 2000] show the proton temperature anisotropy is of order 10 out to many $R_\odot$, but never as large as we calculate. Since V_A actually decreases as r increases, we expect that a modified theory using a reasonable $V_A(r)$ would cause the temperature anisotropy to decrease much more rapidly than we calculate here.

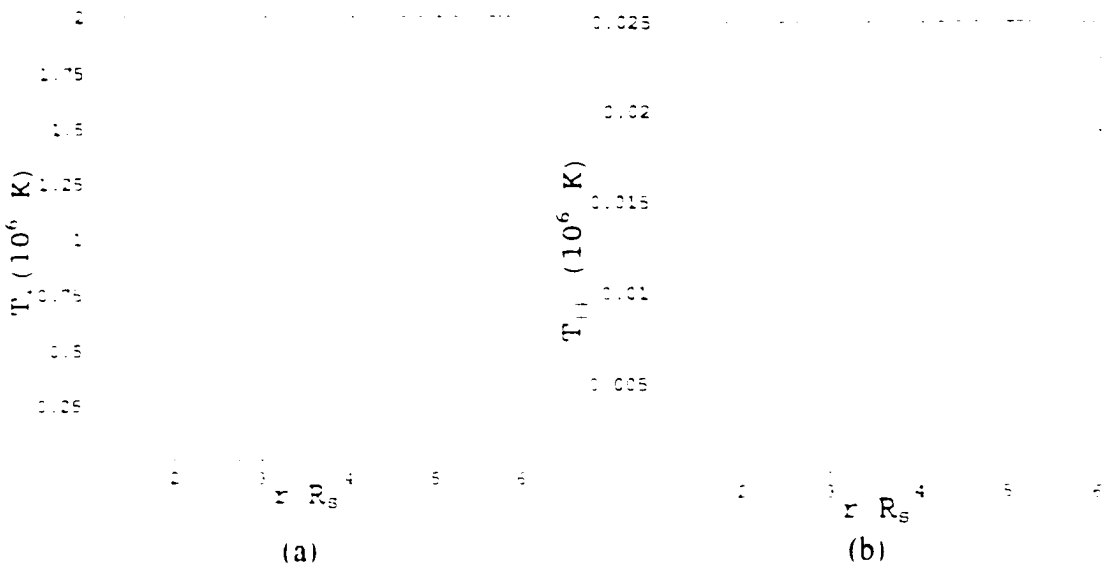

Figure 2.9. Proton perpendicular (a) and parallel (b) temperatures as a function of heliocentric radial distance scaled by R_s.

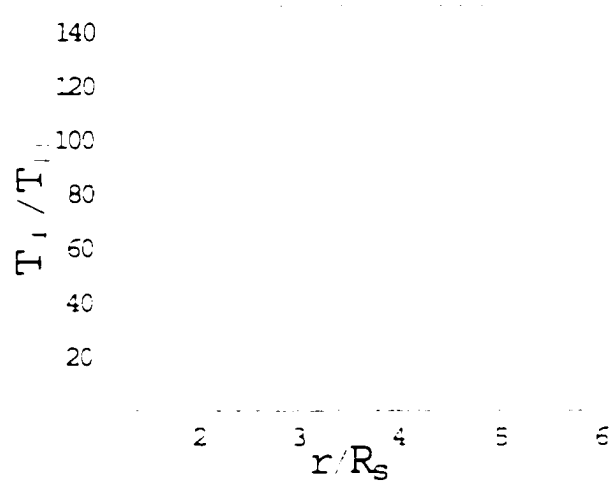

Figure 2.10. Proton temperature anisotropy as a function of r/R_s.

$\frac{1}{2} < x_0 < 1$

The condition $x_0 > \frac{1}{2}$ cannot be met for protons, since for protons $x_0 = 0$. The size of x_0 is strongly influenced by the size of V_A, so given a sufficiently large V_A, x_0 for any other ion species may easily exceed $\frac{1}{2}$. We analyze this case for He^{2+} when $V_A = 750$ km/s and $V_{sw} = 150$ km/s, yielding $x_0 \approx 0.82$. Our choice for V_A is smaller by a factor of at least 2 than typical values of V_A at $r \sim 2R_s$, but we use it since it yields $x_0 < 1$. For heavier ions, or He^{2+} with larger V_A, the condition $x_0 < 1$ may not be reasonable. From Figure 2.11, plotted for He^{2+}, we note that $x_0 > 1$ for $V_A > 850$ *km/s*. The size of V_A may easily exceed 850 *km/s* at $r = 2R_s$, and the increase of x_0 with increasing V_A is more pronounced as mass/charge increases, so obtaining a value of $x_0 < 1$ for heavy ions seems unlikely. However, the results for the case $\frac{1}{2} < x_0 < 1$ possess interesting characteristics, so we choose to discuss it.

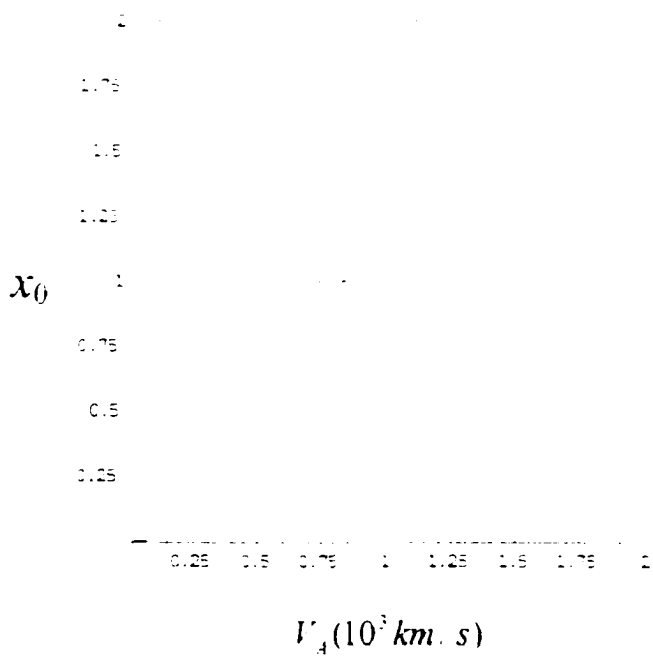

Figure 2.11 x_0 versus V_A for He^{2+}. For $V_A \geq 850$km/s, $x_0 > 1$, and for $V_A < 600$ km/s, $x_0 < \frac{1}{2}$. $x_0 = 0$ for protons for all V_A.

The behavior of the ion distribution when $\frac{1}{2} < x_0 < 1$ is substantially different from the case when $x_0 < \frac{1}{2}$, and is illustrated in Figure 2.12. In Figure 2.12a, we show the delta function shell (curve 2) and delta function boundary in the (−) domain (curve 3) at $r/r_0 = 2$. Figure 2.12b depicts the distribution at the radial distance where the lowest point of curve 3 first intersects the (+ -) boundary; here, $x = 1 - x_0$ and $x' = x_0$. Substituting these values into equation (30) gives $r/r_0 = x_0(1 - x_0) \approx 4.6$ for this case. For $r/r_0 < x_0(1 - x_0)$, f remains singular on curves 2 and 3 with identical amplitude and zero elsewhere (see the relevant discussion in the following subsection for the case $x_0 > 1$).

Once the radial position of the ion distribution exceeds $x_0 r_0(1 - x_0)$, ions will be swept back to $v' < V_{sw} - V_0$ to scatter on new shells, thus creating a continuous ion distribution indicated by the shaded region shown in Figures 2.12c and 2.12d. The lead boundary of the continuous distribution (curve 4) moves toward larger x as r increases while curve 1 moves down, thus broadening the continuous distribution. Since this energy shell (curve 4) is created when curve 3 reaches $(V_{sw} + V_0, 1 - x_0)$, we may determine the radial dependence of its intersection with the (+ -) boundary (x_4) from equation (20) and $r/r_0 = x_0/(1 - x_0)$. We obtain

$$x_4 = 1 - A'(r/r_0)^{-q(1-Q)/(1+qQ)}, \tag{32}$$

where $A' = x_0[x_0/(1-x_0)]^{q(1-Q)/(1+qQ)} \approx 8.5$, $q \approx 3.67$, and $Q \approx 0.23$ for our choice of parameters and He^{2+}. Setting $x_4 = \frac{1}{2}$ in equation (32) yields $r/r_0 = (2x_0)^{(1+qQ)/q(1-Q)} x_0/(1 - x_0) \approx 6.3$. When the continuous part of the distribution

exceeds this radial position, those ions may focus forward into the (−) domain. The delta function fronts and the continuous distribution of f at $r\ r_i \approx 6.3$ are shown in Figure 2.12c.

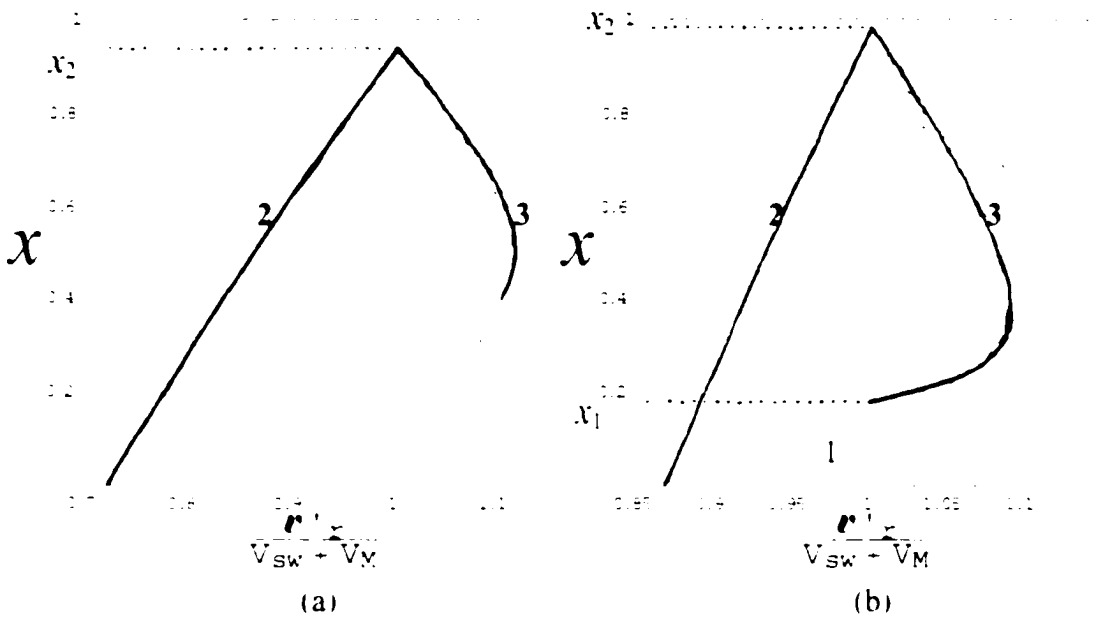

Figure 2.12 **(a)** He^{2+} distribution function boundary curves at $r\ r_i = 2$ for $x \approx 0.82$. Curve 2 is the delta function shell and curve 3 is the boundary curve for nonresonant ions. f is singular with the same amplitude on both curves. $V_{sw} - V_M \approx 276 km\ s$

(b). Similar to 2.12a except $r\ r_i \approx 4.6$. At this radial position curve 3 just returns to the + - boundary. Curve 1 is the lowest wave-frame energy shell (represented by x_1) and is populated by ions just returning to the resonant domain. $x_2 \rightarrow 1$ and $x_1 \rightarrow 0$ as $r\ r_i \rightarrow \infty$. $f \neq 0$ only on curves 1, 2, and 3 at this heliocentric distance.

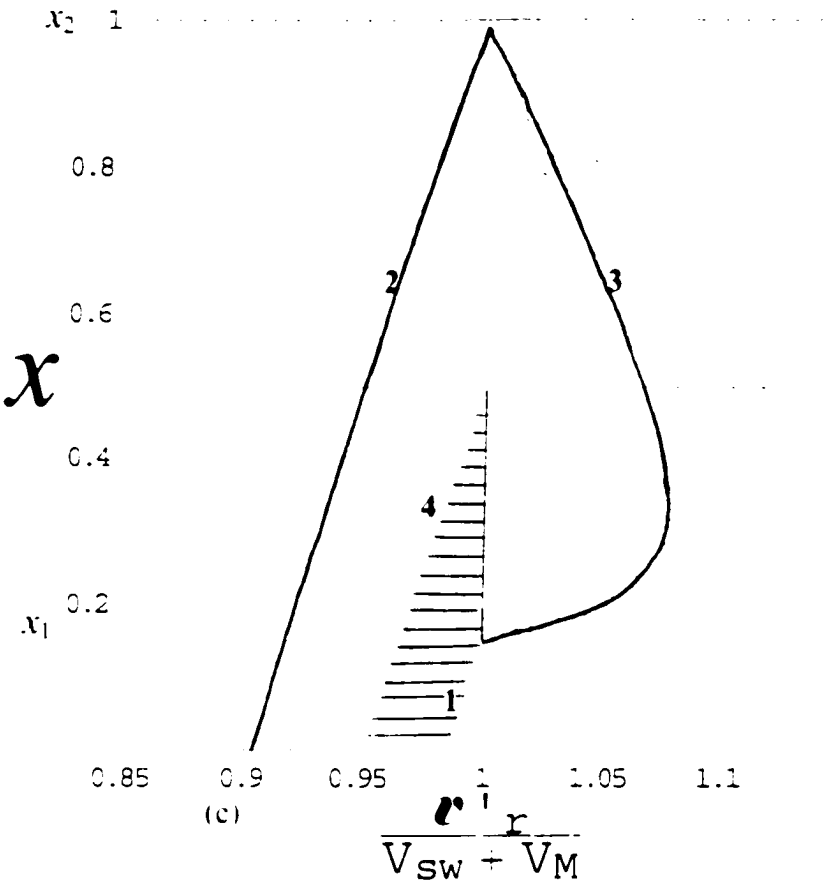

Figure 2.12(c). Similar to 2.12a and 2.12b, but now $r_1 = (2x_{e_1})^{(1-q)/(q+1-Q)} x_{e_1}^{Q/(1-Q)}(1-x_{e_1}) \approx 6.3$. The shaded region contains the continuous part of the ion distribution. Curve 4 is the lead energy shell of the continuous part of the distribution (specified by x_4) and has just reached $x = \frac{1}{2}$ at this radial distance. At this radial distance ions from the continuous part of the distribution focus into the (−) domain. In the interior region bounded by curves 2 and 3 and the shaded region, $f = 0$.

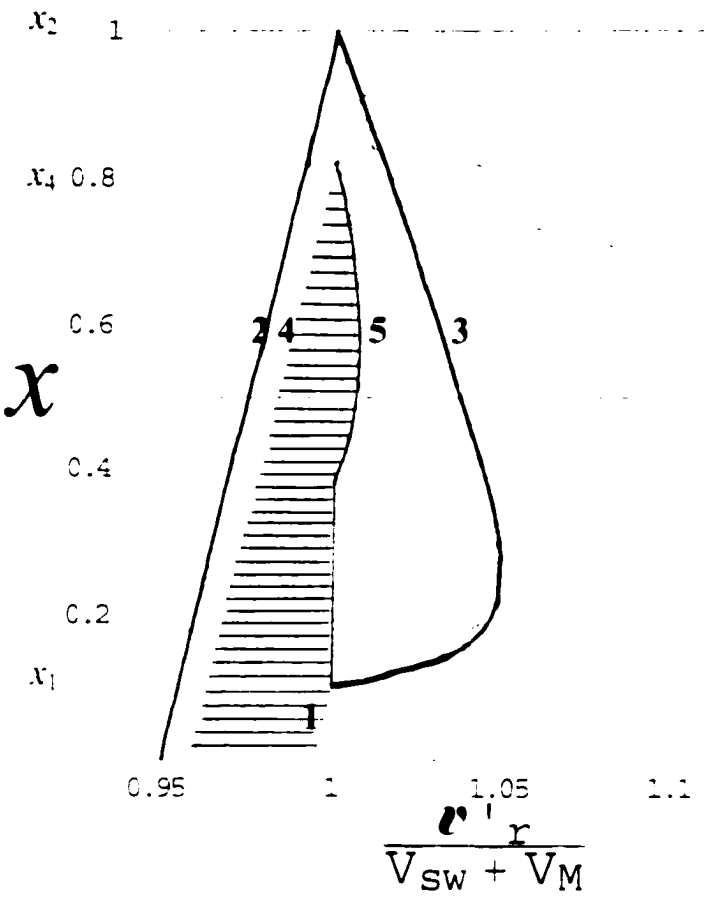

Figure 2.12(d) Here $r r_0 = 12.5$ ($r = 25R_\odot$). Curve 5 is a boundary in the (−) domain resulting from the circulation of ions from the continuous part of the distribution (shaded region). In the interior region bounded by curves 2 and 3 and the shaded region, $f = 0$.

When the radial distance exceeds $(2x_0)^{(1+qQ)/(q(1-Q))} x_0 r_0/(1-x_0)$, resonant ions in the continuous distribution will focus forward, circulate through the (+) domain, and eventually return to the (-) domain to scatter on new shells. Consequently, another boundary (curve 5 in Figure 2.12d) forms in the (−) domain. Employing a method identical to that used to create equation (30) yields the equation of curve 5

$$x = x' x_0 (1-x_0)^{-1} [x_0/(1-x')]^{(1+qQ)/(q(1-Q))} (r/r_0)^{-1}, \qquad (33)$$

where x and x' have the same meaning as before and $v'_r(x)$ is again determined from equation (11). In the gap between the shaded region and curves 1 – 3, as shown in Figure 2.12d for $r/r_0 = 12.5$ ($r = 25R_S$), $f = 0$. As r $r \to \infty$, from equations (28a) and (31), $x_2 \to 1$ and $x_3 \to 1$; thus the gap narrows as radial distance increases.

$x_0 > 1$

At $r = r_0$ a resonant ion with a large mass charge ratio, or a lighter ion scattering on waves with $V_A / V_{sw} >> 1$ may be characterized by $x_0 > 1$. We illustrate this situation in Figure 2.13 with a plot of the distribution function of He^{2+} ions for $V_A = 1000$ km s and $r_0 = 2R_S$, yielding $x_0 \approx 1.46$. The intersection point of the resonant-ion shell (curve 2) with the + - boundary is again given by equation (28a). Magnetic mirroring dominates the effective gravity for $x > 1$; hence, curve 2 will move toward smaller x as r increases. For $r > r_0$ ions will immediately accelerate to $v'_r > V_{sw} - V_M$. Again, a singular distribution forms in the (–) domain (curve 3) specified by the locus of points (v'_r, x), with x given by

$$x = x'[(x_0 - 1)/(x' - 1)]^{(1+qQ)/(1-Q)}(r/r_0)^{-2}. \qquad (34)$$

where x' has the same meaning as before [see equation (30)]. On both curves 2 and 3, f is singular with identical amplitude (see below) and $f = 0$ elsewhere. In Figure 2.13a the ion distribution is shown when $r/r_0 = 2$ and, in Figure 2.13b, $r \to \infty$. As $r \to \infty$ curve 3 approaches the v'_r axis, $v'_\perp \to 0$ and $f(r \to \infty)$ spans a continuous range of radial velocities from $V_{sw} + V_M$ up to a maximum value, V'_{rM}. Ions with radial velocity V'_{rM} were

extracted at the ellipse that intersects the (−/-) boundary at $(V_{sw} - V_M, x_0)$. From equations (10), we find $V'_{rM} = \sqrt{2\alpha GM(x_0 - 1) \quad r_0 + (V_{sw} - V_M)^2}$. For $x_0 > 1$, all ions eventually leave the (-) domain and never return.

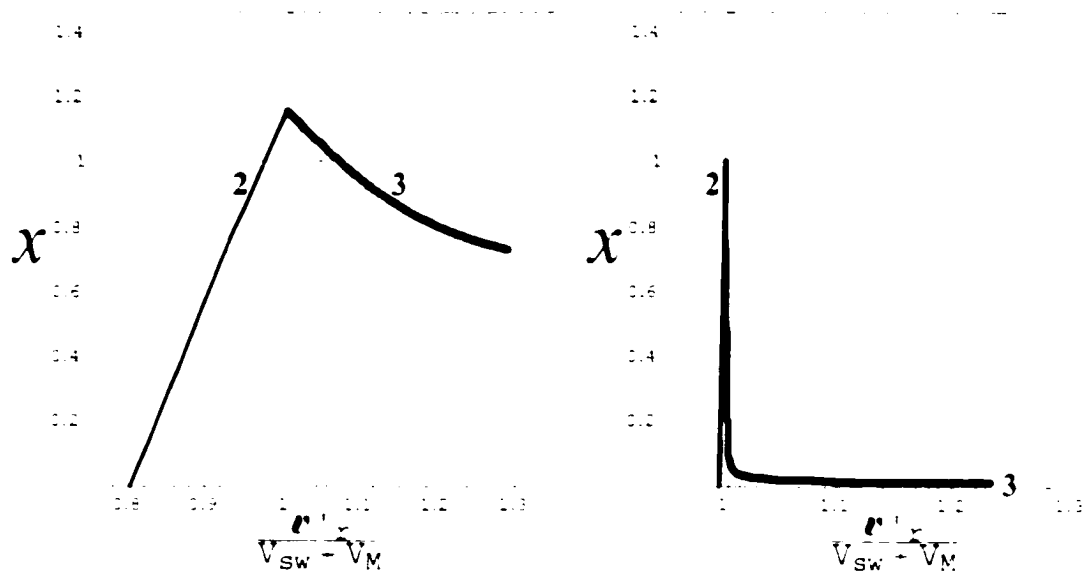

Figure 2.13 (a) He^{2+} distribution for V_A = 1000 km s, V_{sw} = 200 km s, and $r = 4R_\odot$ ($x_0 \approx 1.46$). The distribution function is singular on both curves 2 and 3. $V_{sw} - V_M \approx 368 km\ s$

(b) Similar to 2.13a, but now $r \to \infty$ (actual $r/r_0 = 100$). In velocity space, the distribution collapses to the horizontal line along the abscissa $v_- \to 0$, curve 2 and the "vertical" part of curve 3 collapse to a point at $v'_r = V_{sw} + V_M$, and all particles focus into the (−) domain as and achieve their asymptotic radial velocities.

The resonant ion distribution function for this case is given by [see equations (20) and (26)]

$$f_-(y,x) = a\delta[1 - y(1-x) - x_0]. \tag{35a}$$

Since $x_0 > \frac{1}{2}$, $f_- = f_+$ at the +/- boundary for all r, but we wish to determine $f_-(r, v_-, v'_r > V_{sw} + V_M)$ (See Figure 2.3 for a plot of curves of constant f_-). We

determine a by calculating $n(r_0) = n_0 = \int d^3v f_0$ where $f_0 = f_-(1, x) = a\delta(x - x_0)$.

Integrating and including the small ε approximation ($v \approx v_{pr} - V_M$) yields

$$a = n_0 r_0^2 (v_{pr} - V_M)\ 2\pi x_0 (\alpha GM)^2. \tag{35b}$$

In section 2.2.4 we showed that $f_- = f_-(E, C)$, where $E(r, v_-, v_t')$ and $C(v_-, r)$ are given by equations (10) and (7) and represent the total ion energy and magnetic moment, respectively. Once we know x and y in terms of E and C at the $-$ - boundary, we may determine f_- at all points in the $(-)$ domain.

We determine $x(E, C)$ at the $-$ - boundary by combining equations (7), (10a), and (10b) and setting $v_t' = V_{co} - V_M$ in equation (10a). There results

$$x(E, C) = \tfrac{1}{2}\left[1 - \sqrt{1 - 4C(E - \tfrac{1}{2}V_0^2)\ \alpha GM}\right], \tag{36}$$

where $V_0 \equiv V_{co} - V_M$. Combining equations (36), (10b), and (17b) yields

$$y(E, C) = \left[2C^2(1 - \sqrt{1 - 4C(E - \tfrac{1}{2}V_0^2)\ \alpha GM})\right]^{\sigma}, \tag{37}$$

where $\sigma \equiv q(1 - Q)\ (1 - qQ)$. Substituting the expressions for x and y from equations (36) and (37) into the argument of the delta function in equation (35a) gives $f_-(E, C)$.

The nonresonant ion distribution function is a complicated function of E and C when equations (36) and (37) for $x(E, C)$ and $y(E, C)$ are used. However, a simple, analytical expression for f_- results when we analyze the behavior of $f_-(r \to \infty)$ and let $x_0 - 1 << 1$. This case is reasonably represented by the state of the ion distribution shown in Figure 2.13b ($x_0 = 1.46$). As $r \to \infty$, $v_- \to 0$ and $\alpha GMr^{-1} \to 0$, so from equation (10a) $E \approx \tfrac{1}{2}v_t'^2$. Also for $x_0 \approx 1$, ions will reach terminal velocities only slightly greater than

V_0, so $4C(E - \frac{1}{2}V_0^2)/\alpha GM \approx 2C(v_r'^2 - V_0^2)/\alpha GM << 1$. Expanding the radicals in equations (36) and (37) and substituting the simplified expressions into the argument of the delta function in equation (35a) gives

$$f_-(r, v_-, v_r') = a\delta[1 - x_0 + (C - r_0)^{\sigma-1} r_0 (v_r'^2 - V_0^2) - 2\alpha GM]. \qquad (38)$$

Using equations (35b) and (38), we demonstrate that as $r \to \infty$ the number density of resonant ions (n_-) vanishes and that the number density of nonresonant ions (n_-) conserves number flux. Integrating equation (35a) over the velocity space of the (-) domain, applying the small ε approximation ($v \approx v_{\infty} - V_M$), and using equation (35b) yields $n_- = n_0 r_0^2 r^{-2}(v - x_0 - 1)/x_0 v^2$. For the nonresonant ions, we again calculate number density, but now use $n_- = \int 2\pi v_- dv_- dv_r' f_-$. From equations (7) and (10b) we substitute $\alpha GM r^{-2} dC$ for $v_- dv_-$, set $x_0 = 1$, and again replace a using equation (35b). First integrating the result in C, then integrating in v_r' while applying the small ε approximation ($v_r' \approx V_{\infty} - V_M$) yields $n_- = n_0 r_0^2 r^{-2}$. Clearly, as $r \to \infty$, n_- decreases faster than n_-, so that all ions are eventually focused forward into the (-) domain. See the Appendix, section A.1, for a more detailed discussion of the conservation of number flux.

Ions are not uniformly distributed along curve 3 as $r \to \infty$. The number density of ions with radial velocity in the range v_r to $v_r + \Delta v_r$ is given by $\Delta n_- = (\partial n_-/\partial v_r)\Delta v_r$. Using a procedure similar to that used to calculate n_-, we find

$\partial n_- / \partial v_r \propto (v_r^2 - V_0^2)^{-(1+qQ)/(1+q)}$, where the constant of proportionality depends on ion species. Clearly, Δn_- is a decreasing function of increasing v_r; so, for a given Δv_r, $\Delta n_-(v_r \approx V_0) >> \Delta n_-(v_r \approx V_{rM})$. This seems reasonable as we expect few ions will be accelerated to the highest asymptotic velocities.

As $r \to \infty$, $v_- \to 0$ so $T_- \to 0$, but T is nonzero and is given by equation (31b). The required average values are found by taking moments of f_- as given by equation (38). Performing the integrations and simplifying the result for the case $x_0 - 1 << 1$ yields

$$T = m V_0^2 \Gamma^2 (1 - 2\Gamma)\ k_B, \tag{39a}$$

where

$$\Gamma = [\sigma/(2\sigma + 1)](V_{rM}^2 - V_0^2)/2V_0^2. \tag{39b}$$

Evaluating equations (39) for the parameters used to create Figure 2.13 yields $T \approx 0.72 X 10^6 K$. Helium temperatures in slow solar wind ($V_{sw} \approx 440$km/s) at $r \approx 0.7$ AU may be inferred from Figure 8.2 of *Marsch* [1991], giving $T \approx 0.2 X 10^6 K$. Evaluating equations (39) at $V_A = 1000$km/s (much too large at this distance) and $V_{sw} = 440$km/s yields $T \approx 0.2 X 10^6 K$. However, at a distance of 0.7 AU $V_A \approx 60$km/s; using this value of V_A yields $T \approx 0.05 X 10^6$ K.

2.3.2 Extended $f_0(x)$

In contrast to the delta function distribution, an extended $f_0(x)$ provides a continuous range of ion speeds at $r = r_0$. As a result, a fraction of the ion distribution may extend to $x > 1$ at $r = r_0$, and never return to the (-) domain. We choose a Gaussian in x for this distribution, $f_0(x) = a\exp[-b(x - \bar{x})^2]$, subject to the condition $f(x < 0) = 0$, and where b^{-1} is proportional to the distribution temperature. We determine a by arbitrarily choosing $\bar{x} = 1.2$, $b = 5$, and setting $\int_0^\infty d^3v f_0(v) = n_0$, where in the small ε approximation the integration in velocity space may be transformed to an integration in x (see the Appendix section A.1), and $x(v)$ is defined by equation (17a).

There are in general no resonant ion boundary shells in the case of an extended f_0 since ion energies are unbounded. Our choice of boundary condition $f_0(r_0) = 0$ places an ion front along $v' = V_{sw} + V_M$ at $r = r_0$. As r increases, and ions are focused forward, the front moves into the (+) domain. For $r > r_0$ this infinite, r-dependent, front divides the (+) domain into a region accessible to ions above the front and an inaccessible region below the front (see Figure 2.14). The intersection point of the front with an ellipse that intersects the +- boundary at $(V_{sw} + V_M, x')$ determines ion radial velocities at $r > r_0$ for continuous values of x' at extraction.

To find the equation of the front, we rewrite equation (10b) as

$$x'r_0 = xr\,, \tag{40a}$$

and equation (11) as

$$4v_c^2(x' - 1/2)^2 + (V_{sw} - V_M)^2 = 4v_c^2(x - 1/2)^2 + v_r'^2, \qquad (40b)$$

where the coordinate of the intersection of the front and the ellipse intersecting $(V_{sw} + V_M, x' > 1/2)$ is (v_r', x). Using equation (40a) to eliminate x' in (40b), and $v_c^2 = \alpha GM/2xr$ (see section 2.2.4), we obtain

$$x = (1/2)C_0\alpha^{-1}(r/r_0)\left[(r/r_0)^2 - 1\right]^{-1}(1 - qQ)^2\left[v_r'^2 - (V_{sw} - V_M)^2 - 1\right] + (r/r_0 - 1)^{-1}. \qquad (41)$$

The intersection point of the front and the + - boundary is $(v_r' = V_{sw} - V_M, x_0)$, where

$$x_0 = (r/r_0 - 1)^{-1} \qquad (42)$$

follows from equation (41). Two positions of the front corresponding to the two different values of r/r_0 are indicated in Figure 2.14. Ions at the front that entered the (−) domain at comparatively large x have circulated along a smaller fraction of their elliptical trajectory than ions that entered the (−) domain with smaller x. As r/r_0 increases, the front moves in a clockwise sense along the elliptical projections of the characteristics of f_0, indicating increased radial velocity for increased x at extraction due to acceleration by the net radial force. As $r \to \infty$ in equations (41) and (42), $x \to 0$ and $x_0 \to 0$, and the front becomes a straight line along the v_r' axis; all ions extracted with $x \geq 1$ at $r = r_0$ have $v_r' \to v_{r\infty}'$, where $v_{r\infty}'$ is defined after equation (13), and those ions with $x < 1$ are swept back to $v_r' < V_{sw} + V_M$. This large-r behavior of the front is similar to the large-r behavior shown in Figure 2.13b for the delta function f_0 with $x_0 > 1$. However, for our choice of extended f_0 there is no upper limit to v_r'.

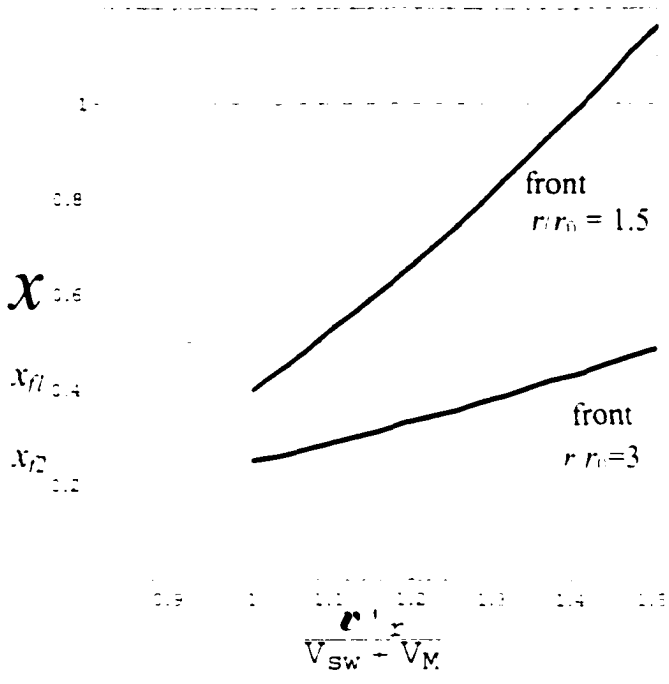

Figure 2.14. Ion fronts in the (−) domain at $r/r_0 = 1.5$ (top curve) and $r/r_0 = 3$ (bottom curve).

Contours of f for protons in velocity space are plotted in Figure 2.15. Equation (41) may be converted to velocity space using equation (7), yielding $v'_-(v'_x)$ that is a hyperbola, and equation (42) becomes $v'_- - V_M = \sqrt{2\alpha\left[C_1(r - r_1)(r - r_1 + 1)\right]}$. Comparing Figure 2.15a with 2.15b and 2.16a with 2.16b we note that $f_- = 0$ below the front, and the front flattens and v'_{-f} moves toward lower v'_- as r increases. The entire distribution moves toward $V_{SW} - V_M$ as r increases due to adiabatic deceleration. Ions extracted at the + - boundary having $x \le 1$ produce the contours of f_- that circulate through the (−) domain and return to the (+ -) boundary. Ions having $x > 1$ at extraction produce contours of f_- that terminate on the front in the (+) domain, and constitute the fraction of ions that free-escape to infinity. The distribution does not become abruptly zero in region

II. as it does in region I (see Figure 2.15), but the values of f in region II are smaller than 0.1, therefore appear as white. The region bounded by the resonant-ion contours on the left and the vertical line $v'_r = V_{sw}$ on the right in Figure 2.15 is analogous to region VI in Figure A6. No ions occupy this region of velocity space, but as can be seen by a comparison of the two figures in Figure 2.15 and Figure A6, this region decreases in size as r increases. The effective gravity creates this "hole" in the distribution at r near r_0, but ongoing mirroring and decreasing effective gravity decreases its size as r increases.

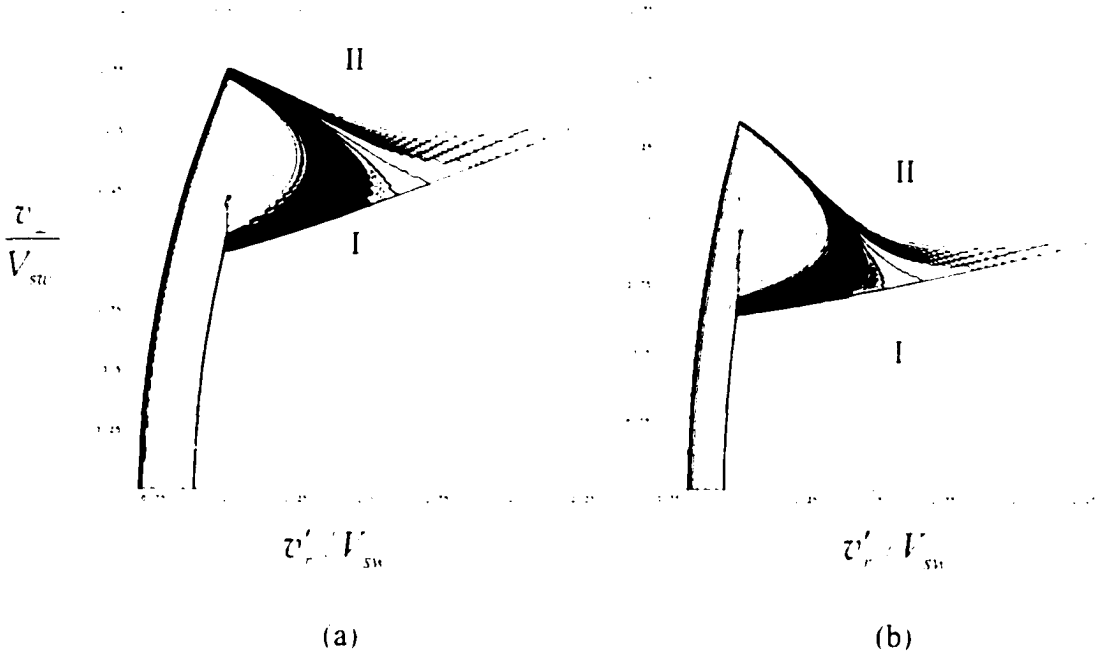

Figure 2.15. Contour plots of the proton velocity distribution function when V_A = 1500 km/s and V_{sw} = 150 km/s. Plot (a) was made for r = $3R_s$ and (b) r = $5R_s$.

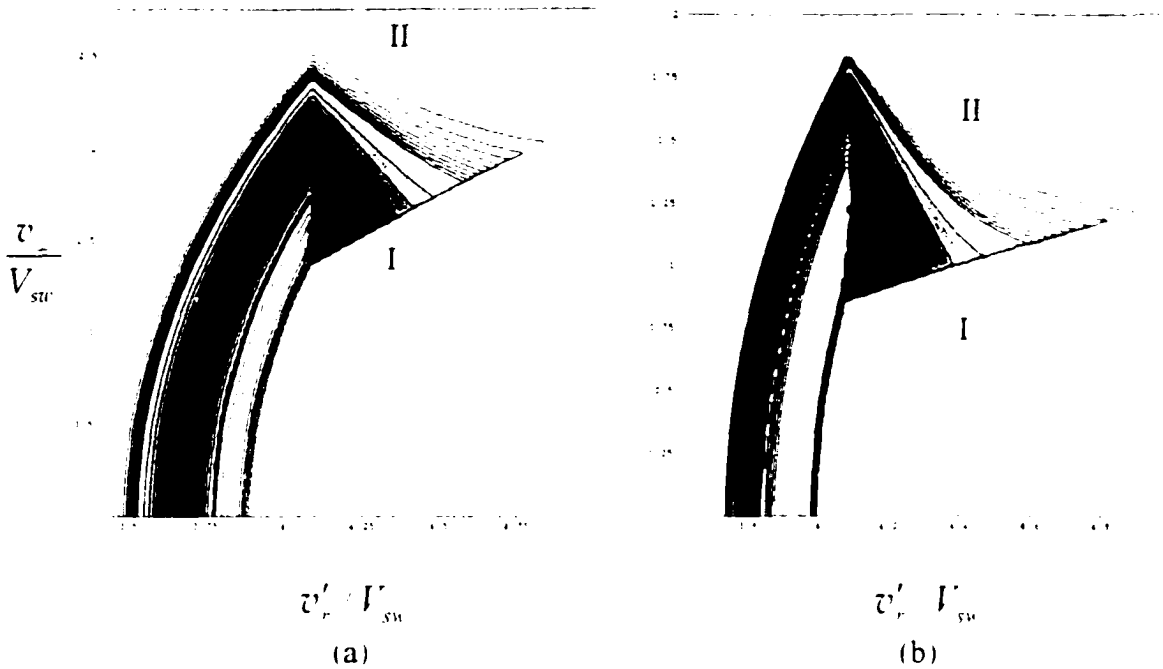

Figure 2.16. Contour plots of the O^{5+} velocity distribution function when V_A = 1500 km/s and V_{sw} = 150 km/s. **(a)** r = $3R_s$ **(b)** r = $5R_s$.

Heavy ions stream outward with a higher average radial velocity than protons and for a given r, heavy ions have a higher perpendicular velocity. These results are consistent with the conditions built in at r_0 and are similar to those obtained with the use of the delta function boundary condition.

Perpendicular and parallel proton temperatures are plotted in Figures 2.17a and 2.17b. At small r, both temperatures for the extended f_0 are larger than those calculated using the delta function f_0 (Figure 2.9) due to the greater extent in velocity space of the extended distribution. As r increases, the discrepancy between the values of $T_\perp(r)$ shown in Figures 2.9a and 2.17a decreases. In Figure 2.18 at $r \approx 2R_s$, $T_\perp / T_\parallel \approx 30$. The calculated anisotropy is less here than that resulting from the use of the delta function f_0 since the

distribution resulting from an extended f_0 has a greater extent in $v'_\perp$, yielding a larger T for a given r.

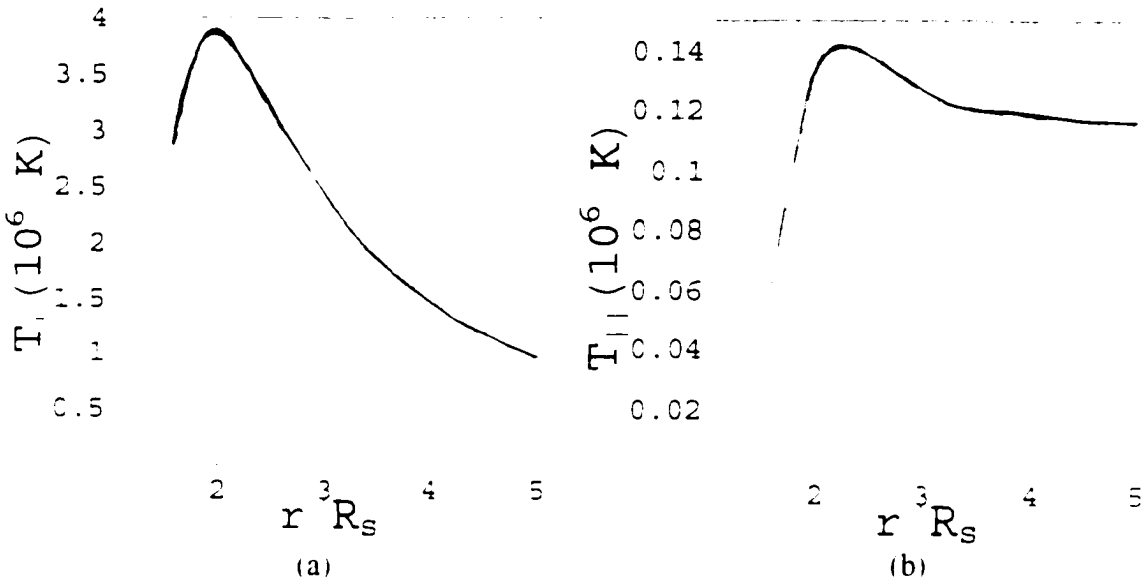

Figure 2.17. Proton perpendicular (a) and parallel (b) temperatures versus r R_S. V_A = 1500 km/s and V_{SW} = 150 km/s

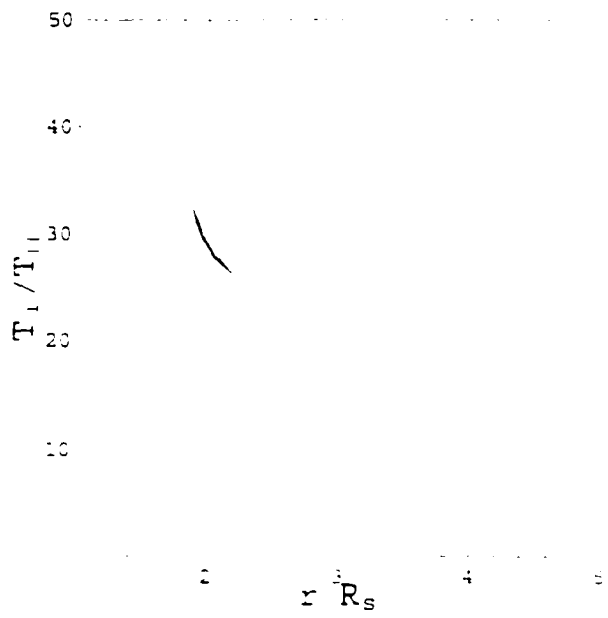

Figure 2.18 Proton temperature anisotropy versus r R_s. V_f = 1500 km/s and V_w = 150 km/s.

Parallel and perpendicular temperatures of O^{5+} are plotted in Figure 2.19. The perpendicular temperatures are slightly lower than observed temperatures at $r = 2R_s$ and decrease as r increases in contradiction to observations [*Kohl et al.*, 1998, *Antonucci et al.*, 2000]. The parallel temperatures are low compared with observations by about a factor of 5 and decrease instead of remaining constant as r increases. Due to the low parallel temperatures, the calculated O^{5+} temperature anisotropy (Figure 2.20) is about 30 and is higher than the value of approximately 10 estimated by *Kohl et al.*, [1998], and *Antonucci et al.*, [2000].

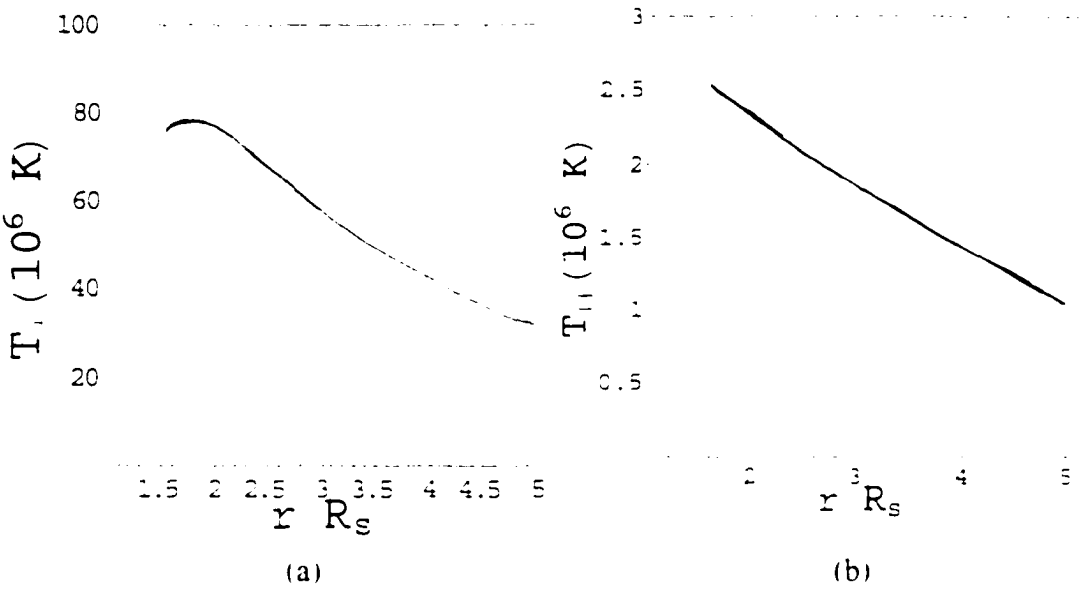

Figure 2.19. O^{5+} perpendicular (a) and parallel (b) temperatures versus r/R_s. V_f = 1500 km/s and V_{sw} = 150 km/s.

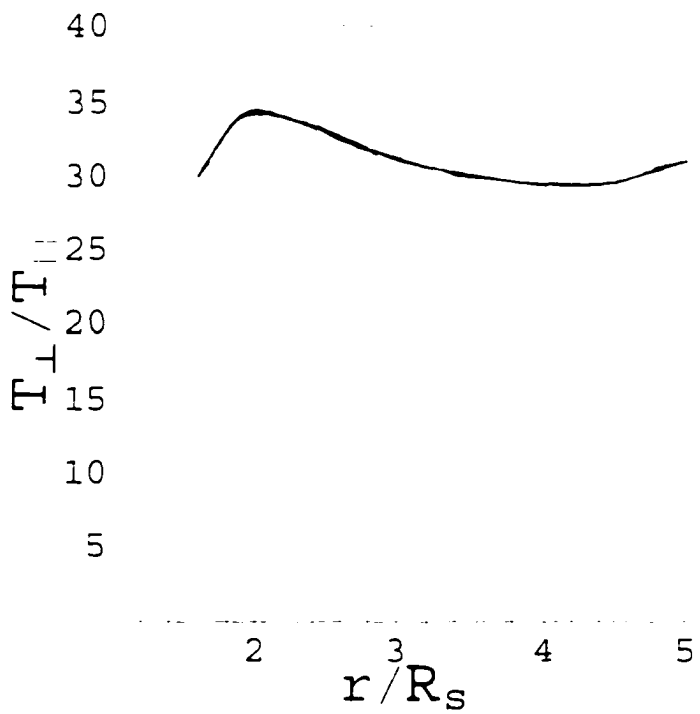

Figure 2.20 O^{5+} temperature anisotropy versus r/R_s.

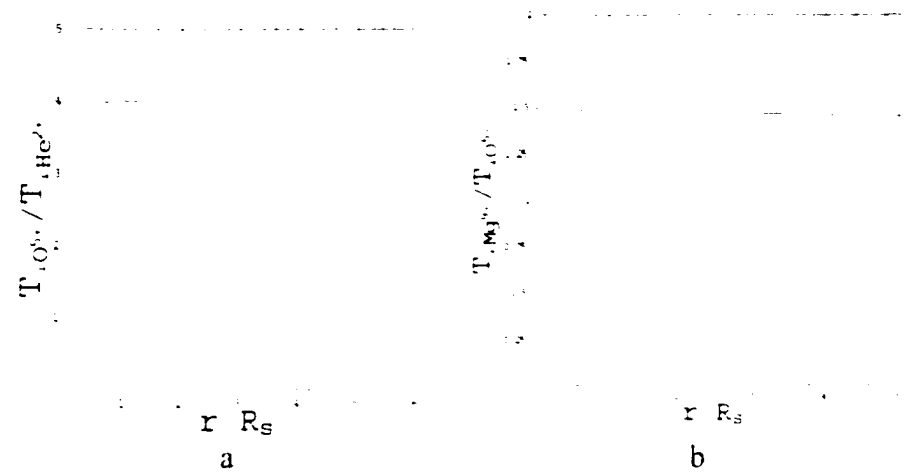

Figure 2.21a. Ratio of $T_{\perp O^{+}} / T_{\perp He^{+}}$ versus r/R_s. Oxygen (mass = 16 u) to helium temperature ratios are at least mass-proportional and tend to be slightly more than mass proportional as r increases.

Figure 2.21b. Ratio of $T_{\perp Mg^{+}} / T_{\perp O^{+}}$ versus r/R_s. Magnesium (mass = 24 u) to oxygen temperatures are mass-proportionally at all r considered.

Figure 2.21 shows that the ratio of perpendicular temperatures of heavy ions is equal to the ion mass ratio. However, heavy ion perpendicular temperature ratios exceed mass ratios when compared with protons, which is obvious from the comparison of Figure 2.17a with Figure 2.19a.

CHAPTER 2.4

DISCUSSION AND CONCLUSIONS

To provide insights into the heating and acceleration of solar wind protons and heavy ion species by proton-cyclotron waves, we have obtained predominantly analytical solutions of equation (1) for the ion distribution function. We take the distribution function to be comprised of cyclotron resonant (f_-) and nonresonant (f_+) parts with the division in velocity space specified by the radial velocity V_0 determined from the cold, electron-proton dispersion relation. Here, V_0 is the maximum velocity in the average proton frame of ions resonant with LHP waves, and we take the wave phase speed to be constant. We adopted the essential features of the Kinetic Shell Model [*Isenberg* 1997, 2001a, b; *Isenberg et al.*, 2000, 2001] to represent the resonant portion of the ion distribution. This model includes the assumption that wave-ion interactions take place on a time scale short compared with times required for large-scale processes to modify the distribution; thus, for $r > r_0$ we assume that ions will always be distributed uniformly in pitch-angle along shells of constant kinetic energy in the wave frame. At the radial position r_0, we specify the boundary condition $f_-(r_0, v) = f_0(v)$ and $f_-(r_0) = 0$.

Equation (1) was solved analytically for f_-, yielding solutions dependent on ion total energy and magnetic moment, where each is conserved. The characteristics of equation (1) yielded the conditions $x > \frac{1}{2}$ for radial acceleration of ions into the (−) domain and

$x > 1$ for free escape of ions from the effective gravity, where x is given by equation (7). To find an approximate, analytical solution for f_-, we changed variables in equation (1) to $\varepsilon = v - (v_{ph} - V_d) << v_{ph} - V_d$, which is valid where the wave phase speed is much greater than the ion thermal speed, and extended the analysis to radial distances where the approximation is not formally valid. We may easily check the validity of the small ε approximation by comparing ε / V_i to $(v_{ph} - V_d) / V_i$. As ion mass/charge grows without bound, $(v_{ph} - V_d) / V_i$ approaches zero. However, for ions typically found in the solar wind and corona (protons, alpha particles, O^{5+}, O^{6+}, Mg^{9+}, Fe^{11+}), $(v_{ph} - V_d) / V_i \sim 1/2$. The small ε approximation is not valid for very massive ions, but for most ion species present in the solar corona, where $V_i \sim 10^3$ km s, $\varepsilon / V_i << 1/2$ is easily satisfied.

Transforming equation (1) to (x, y) space, where x and y are given by equations (17), greatly facilitates its solution. Much of the structure of $f_-(y, x)$ can be determined analytically and the remaining region is described by an integral equation solved by a method described in section A.4 of the Appendix. The velocity distribution $f(v_r, v_\perp, r)$ is obtained from $f_-(y, x)$ by using the definition of x in equation (17) and the continuity of f at the +/- boundary allows determination of f_+.

To solve equation (26) for f_- we must specify f_0, but there is no a priori rationale to choose a particular function for f_0. We analyzed in detail the two cases: $f_0(x) \propto \delta(x - x_0)$ and an extended $f_0(x) = a \exp[-b(x - \bar{x})^2]$, where we require $\int_0^\infty d^3v f_0(v) = n_0$. Despite the

obvious differences in the forms of f_0, f_- is less sensitive to the form of f_0 as r r_0 increases. Consider Figures 2.8 and 2.15, where, in Figure 2.8, f_0 is given by the delta function, and, in Figure 2.15, f_0 is the extended function. At $r = 3R_1$ (Figures 2.8a and 2.15a) we note some agreement between the plots made for the two forms of f_0. The maximum values of v_- and the extent in v_z' of the resonant distributions are approximately equal. A comparison of Figures 2.8b and 2.15b ($r = 5R_1$) shows improved agreement between the plots. The extended f_0 always provides some ions at $x > 1$, but here we restrict the delta function f_0 to $x < 1$. Since the analytical form of the boundary in the $(-)$ domain depends on whether f_0 is the delta function or extended function, the ion distributions created from different forms of f_0 for $v_z' > V_{sc} - V_0$ will only approximately agree at any $r > r_0$.

Velocity space contours of the proton distribution function using $f_0(x) = a\exp(-ax)$, which is different from the form used in section 2.3.2, are plotted in Figure 2.22 at $r = 5R_1$. Again, we set $\int_0^r d^3v f_0(v) = n_0$, which matches the conditions imposed on the previous choice of extended $f_0(x)$.

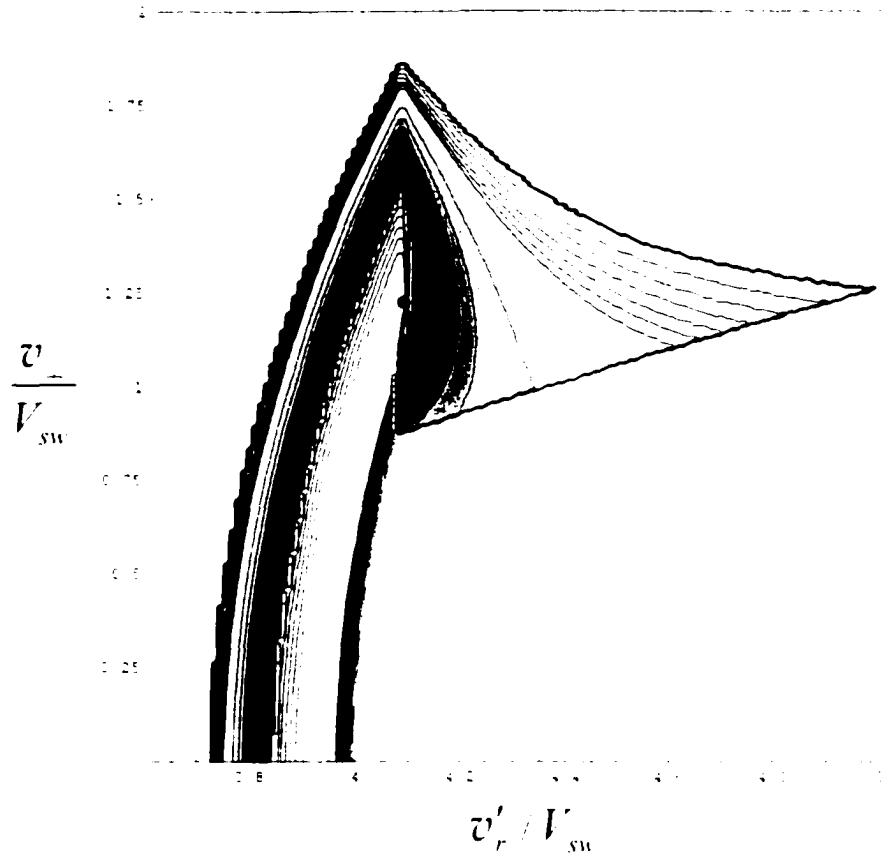

Figure 2.22 O^{5+} velocity distribution at $r = 5\ R_s$ for $f_0(x) = a\exp(-ax)$. This distribution is similar to that shown in Figure 2.16b for $f_0(x) \propto \exp[-b(x-\bar{x})^2]$. The form of f_0 has little effect on the large-r behavior of the velocity distribution.

Figure 2.22 compares very well with Figure 2.16b despite the use of different functions for $f_0(x)$, further substantiating our assertion that the form of $f_0(x)$ is less important as r increases. Also, consider Figure 2.23 which shows $T_-(r\ \ R_s)$ for O^{5+} calculated using both the Gaussian f_0 (top curve) and the exponentially decaying f_0 (bottom curve). At small r, the two curves do not match, but become indistinguishable for $r \geq 3.5R_s$.

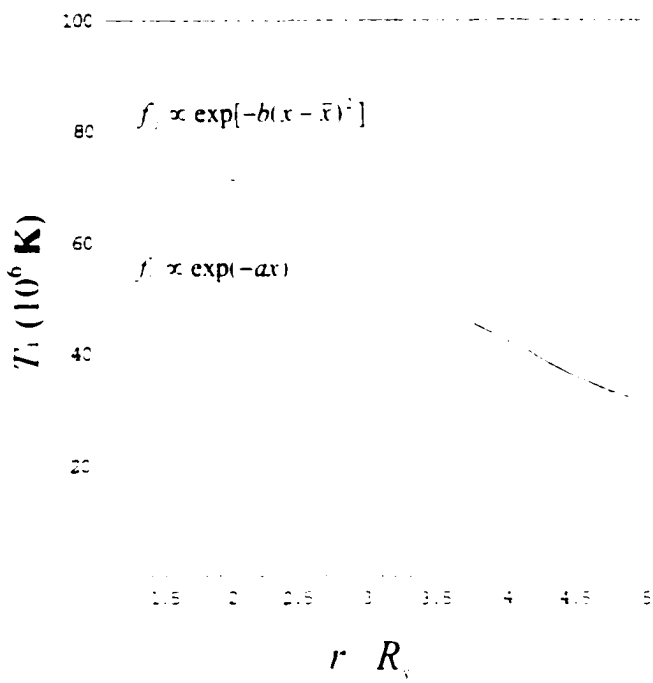

Figure 2.23 Comparison of perpendicular temperatures as a function of r R_s for $f_0 \propto \exp(-ax)$ (lower curve) and $f_0 \propto \exp[-b(x-\bar{x})^2]$ (upper curve). At small r, the two curves diverge, but as r increases past approximately $3.5R_s$, the two curves coincide.

We took $f_s(r_0) = 0$, but if we had assumed $f_s(r_0) > 0$, we would have obtained similar ion velocity distributions for $r > r_0$. Non-resonant ions moving too slowly to escape the effective gravity at r_0 would have quickly been swept back to the (-) domain by the effective gravity. These ions would add to the distribution of resonant ions already on energy shells. The basic shape of the resulting distributions and the magnitude of the gradients of f would not be changed in important ways. *Isenberg et al.* [2001] used an initial distribution symmetric about $v_r' = V_{ra}$. They began the calculations at $r_0 = 2R_s$ and by $r = 2.55R_s$ a velocity distribution was generated that closely resembles our result (Figure 2.8a) for the delta function f_0 at a similar radial distance.

The gradient in f_- at large v in Figures 2.15 and 2.16 corresponds to the "pile up" shell as described in *Isenberg et al.* [2000, 2001]. Energy shells at high v ($x > 1$) contain ions having high $v_\perp$ which can be accelerated to higher radial velocities by the mirror force. Continuous, rapid, wave-ion interaction maintains uniformity along the shell; effecting acceleration of the entire shell to higher v'_r. Similarly, low-v ($x < 1$) shells are slowed to lower v'_r by the dominant effective gravity. Thus, this convergence of ions in velocity space creates a ridge in f_- corresponding to $x = 1$. A similar situation happens for the delta function f_0, Figure 2.8. There are no ions in the domain $x > 1$, but ions on low-v shells are continually slowed to lower v'_r by the effective gravity, and the entire distribution is focused forward to higher v'_r by mirroring. Thus, a large gradient in f_- at high v results, although it is not as dramatic as in the case of the extended f_0, since ions converge on $x = 1$ from only one direction.

A comparison of Figures 2.15 and 2.16 shows the higher radial velocity of O^{5+} ions compared with protons at a given radial distance, which agrees qualitatively with observations that indicate heavy ions stream outward from the Sun faster than protons [*Neugebauer et al.*, 1994, 1996; *Goldstein et al.*, 1995; *Goldstein*, 1996; *Kohl et al.*, 1998; *Cranmer et al.*, 1999a, 1999b; *Goldstein and Neugebauer*, 2001]. This differential ion-proton streaming is to be expected as we build it in at r_0 through use of the cold electron-proton plasma dispersion relation. The + - boundary occurs at V_{sw} for protons ($V_A/10$ for our choice of V_A and V_{sw}), $\sim 4V_{sw}$ ($0.4V_A$) for O^{5+}, and at $(1-qQ)V_{sw}$ ($(1-qQ)V_A/10$) for an arbitrary ion species characterized by q and Q, which are controlled

by V_A. Clearly, the bulk speed of all heavy ion species must exceed the bulk proton speed.

Central to our theoretical formalism is the cold, electron-proton dispersion relation, where its use is justified since we primarily devote our attention to regions close to the Sun where the plasma β is low. However, since helium constitutes a significant fraction of the solar wind number density, we discuss its effect on the dispersion relation if it is included. Figure 2.24 depicts the cold plasma dispersion relation for LCP ion-cyclotron waves [*Gomberoff and Elgueta*, 1991, *Hollweg*, 2000] given by

$$kV_A = \omega \left[\Omega_p (1 - \omega \Omega_p) + 4(n_{He^{2+}} \Omega_{He^{2+}})(1 - 2\omega \Omega_{He^{2+}})\right]^{-1}. \quad (43)$$

The thick lines give the dispersion relation when a 5% number concentration of He^{2+} ions is included, and the thin line results when the plasma consists of only electrons and protons, and is identical to the LCP part of the dispersion curve shown in Figure 2.2. When He^{2+} is included, the dispersion relation splits into two branches separated by the resonance gap at the He^{2+} cyclotron frequency. Still, only protons with negative velocities in the solar wind frame are cyclotron resonant, but when He^{2+} is included in the dispersion relation, heavy ions traveling with radial velocities much higher than V_M may also resonate with waves. However, despite the possibility that heavy ions with essentially unlimited radial velocity may be cyclotron resonant, we expect that such high-velocity ions will be few in number since resonant waves with extremely high v_{ph} are unlikely.

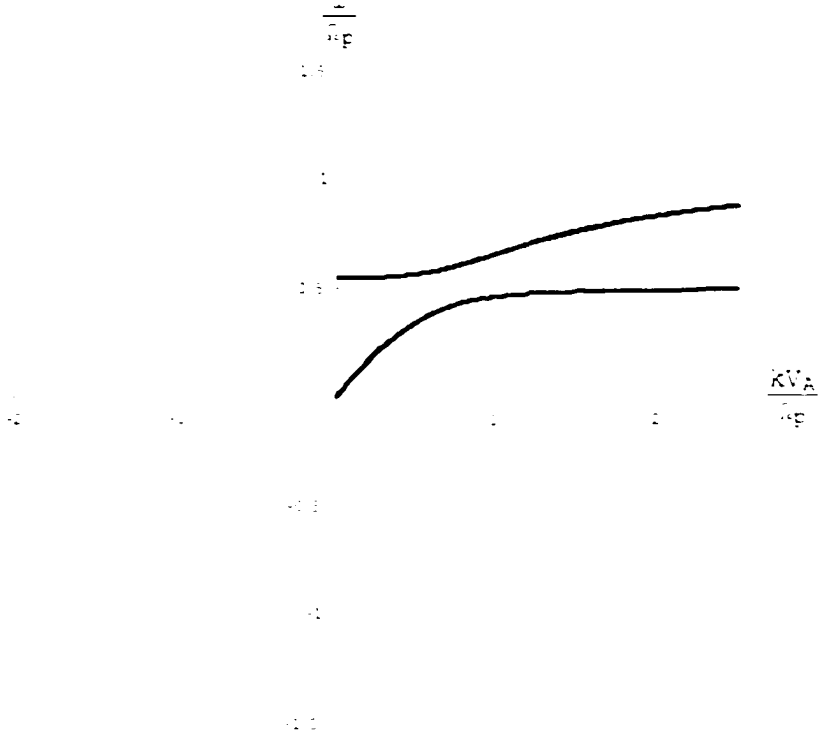

Figure 2.24 Cold plasma dispersion relation. Plasma is composed of electrons, protons, and 5% He^{2+} by number. The thin curve is the dispersion relation when no helium is present and the thick curves result when helium is included. The resonance gap occurs at $\omega = 0.5\ \Omega_p$

Rigorously including wave dispersion (see *Gendrin and Roux*, 1980; and *Isenberg and Lee* [1996] for a discussion of dispersion in an electron-proton plasma) would result in the reduction of the $v_\perp - v_\parallel$ anisotropy and consequently a reduction of the maximum attainable value of $v_\perp$.

The most serious simplification we make in this analysis is taking V_A and V_{sw} constant. Allowing both speeds to vary with r would require the addition of the term $-(U + v\mu)\partial U / \partial r[\mu \partial f / \partial v + (1-\mu^2)\, v\partial f / \partial \mu]$ to the left side of equation (1). The factor $-(U + v\mu)\partial U / \partial r$ combines with $-\alpha GMr^{-2}$ to produce an overall effective gravity with the nature of its contribution dependent upon the sign of $\partial U / \partial r$. Near the Sun where the solar wind speed is rapidly increasing and the Alfvén speed is decreasing, but not as rapidly, we expect $\partial U / \partial r > 0$. Thus, for $\partial U / \partial r > 0$ and $r \approx r_0$, where the ε approximation is most valid, the effective gravity is still radially inward and stronger than that actually used in the calculations. Qualitatively, a stronger effective gravity should produce a more rapid circulation of ions through the (-) domain, and a more rapid increase of ε with r. Consequently, the validity of the small ε approximation is commensurately reduced.

The condition $x > 1/2$, required for resonant ions to be focused forward from the (-) domain into the (+) domain, may also be determined by elementary means through $-(v^2 - 2B)\partial B / \partial r - \alpha GMr^{-2} = V_{sw}\partial v / \partial r$, where if ions are to be focused forward we require $V_{sw}\partial v / \partial r > 0$. When $\partial U / \partial r \neq 0$ this inequality is modified to $-(v^2 - 2B)\partial B / \partial r - [\alpha GMr^{-2} - g(U, v)\partial U / \partial r] > 0$, where $g(U, v)$ is a positive function of U and v that would result from the integration in μ of equation (1) modified for $\partial U / \partial r \neq 0$. The condition on x for an ion to focus forward into the (+) domain then becomes $x > \frac{1}{2}[1 + g / (\alpha GM / r^2)\partial U / \partial r] > \frac{1}{2}$ for $\partial U / \partial r > 0$. Thus, a qualitative effect of including $U(r)$ and $V_A(r)$ ($\partial V_A / \partial r < 0$) in equation (1) is the increase of the x-dependent

circulation point to a variable value greater than ½ at small r/r_0; this circulation point approaches ½ as r/r_0 increases and $\partial U'/\partial r$ decreases. Thus, including radially dependent U' and V_4 changes the circulation point from a fixed value of $x = ½$ to a radially dependent function. This concept of a variable circulation point is analogous to the critical value of v_- given by *Isenberg et al.* [2001].

Isenberg et al. [2001] calculated velocity space distributions numerically that are unstable to the generation of inward propagating waves because of the steep gradients in the antisunward part of the ion distribution. We also predict steep gradients in f_- as shown in Figures 2.8, 2.15 and 2.16. Therefore, the distributions resulting from our analysis will also be unstable to the generation of inward propagating waves. Modifying the derivation of equation (18) to include both inward and outward propagating waves results in two equations

$$xv\frac{\partial f_-}{\partial v} - x(1-x)\frac{\partial f_-}{\partial x} + (2x-1)(f_- - f_+) = 0 \qquad (44a)$$

$$xv\frac{\partial f_-}{\partial v} + x(1-x)\frac{\partial f_-}{\partial x} + (2x-1)(f_- - f_-) = 0, \qquad (44b)$$

where $f_+ = H(x-½)f_- + H(½-x)f_+$, and $H(\theta)$ is the Heaviside step function. Clearly, equation (44b) is equivalent to equation (18). Equations (44a) and (44b) are a coupled set of equations that require simultaneous solutions for both f_- and f_+. We leave the solution of equations (44) to future work, but note that the inclusion of inward propagating waves appears necessary for a complete treatment of this problem.

Several recent works [*Tam and Chang*, 1999; *Dmitruk*, 2001; *Isenberg* 2001c; *Tu and Marsch*, 2001] have investigated the effects on the heating of ions and acceleration of the fast solar wind when both inward and outward propagating waves are present. These and our theoretical models assume that sufficient wave power is always present at the high resonant frequencies [*Harmon and Coles*, 2001], but inward propagating waves near the Sun have not been observed.

We showed that ion velocity distributions must deviate significantly from Maxwellian distributions when resonant wave-ion interactions are prevalent and ion-ion interactions are neglected. The cold, electron-proton dispersion relation provided the resonance condition. We obtained ion-proton differential streaming with ions maintaining outflow velocities exceeding that of protons, regardless of the form of f_0, and the velocity difference is ordered by the Alfvén speed. The calculated velocity distributions yielded $T_\perp > T_\parallel$ temperature anisotropies, which is reasonable since the assumption of effective pitch-angle scattering is integral in transforming equation (1) into equation (15). For a given r, a comparison of heavy ions yields mass-proportional perpendicular temperature ratios, but when comparing heavy ions to protons we find that the temperature ratios are more than mass proportional.

Observations [*Kohl et al.*, 1998; *Cranmer et al.*, 1999b] indicate that O^{5+} temperatures increase by more than an order of magnitude and proton temperatures [*Suleiman et al.*, 1999] are approximately constant between roughly $1.5R_\odot$ and $3.5R_\odot$. However, the model presented in this work predicts decreasing temperatures with increasing radial distance

for all ion species considered. Increasing (decreasing) V_A increases (decreases) $T_\perp - T_\parallel$ at all r, but $T_\perp$ remains a decreasing function of increasing r.

We find that Mg^{9+} is mass proportionally hotter than O^{5+} (Figure 2.21b) and more than mass proportionally hotter than protons, which contradicts observations [*Esser et al.* 1999]. Since Mg^{9+}, O^{5+}, and O^{6+} have similar charge to mass ratios, we would expect these ions to exhibit similar heating. *Cranmer* [2000] suggests that since Mg^{9+} and O^{6+} have the same charge to mass ratio, O^{6+} might absorb wave energy that could otherwise be available to heat Mg^{9+}; hence, Magnesium's lower observed temperature.

Despite these failures, we believe the basic formalism described in chapter 2.2 is valuable and should be applied to equation (1) modified to included radially varying wave and solar wind speeds and eventually bi-directional wave propagation.

APPENDIX TO PART II

APPENDIX TO PART II

A.1 Conservation of Number Flux

The steady state equation of continuity for radial flow yields the condition of conservation of number flux, $\mathcal{F} = n\,v_r\,r^2 = \text{constant}$, where $\overline{}$ indicates an average quantity, and $n = \int d^3v f$ is ion number density. We take the bulk flow speed to be constant, $v_r = \text{constant}$, so in the small ε approximation, nr^2 is also constant. When considering resonant ions we use $d^3v = 2\pi v^2 dv d\mu$ for the volume element in velocity space and for nonresonant ions $d^3v = 2\pi v_r\, dv_r\, dv_t'$. These choices help facilitate calculations due to the different definitions of x, equations (7) and (17a). Next, we show that the basic differential equations for both the resonant and nonresonant parts of the ion distribution function also yield $\mathcal{F} = \text{constant}$.

We first show that $\mathcal{F}$ is conserved for nonresonant ions by operating on equation (8) with $\int_0^x\int_0^r dx dv_t'\, 2\pi\alpha GMr^{-1}$, where we used equation (7) to replace $v_r\, dv_r$ by $\alpha GMr^{-1}dx$. The middle term in equation (8) may be integrated in v_t' and vanishes at both limits of integration. Integrating the third term by parts yields $\int_0^x\int_0^r dx dv_t'\, 2\pi\alpha GMr^{-1}v_t' rf$, which is

equivalent to $\partial^2 r^{-1}$. The first term, $\int_0^{\infty}\int_0^{\infty} dx dv' 2\pi\alpha GMr^{-1}v' r^2 \partial f / \partial r$, is equivalent to

$\partial/\partial r - \partial^2 r^{-1}$. Combining these terms immediately yields $\partial/\partial r = 0$.

We now consider resonant ions and note that the limits of integration in μ are -1 and $-(v_{ph} - V_M)/v$. Employing the small ε approximation, $v \approx v_{ph}$, and transforming to x through equation (17a) yields $nr^2 = 2\pi v_{ph}(\alpha GM)^2 (\int dx x f_0)(v_{ph} - V_M)^2$. We rewrite equation (18) as

$$v\frac{\partial(xf_0)}{\partial v} + \frac{\partial[(1-x)xf_0]}{\partial x} = 0, \qquad \text{(A1)}$$

where we set $f_1 = 0$ for simplicity and modified the equation slightly to facilitate its integration. Operating on equation (A1) with $\int dx$

yields: $v\frac{\partial}{\partial v}\int dx x f_0 + \int dx \frac{\partial}{\partial x}[(1-x)xf_0] = 0$. The second term may be integrated immediately and the result vanishes at both limits of integration. The integral in the first term is proportional to nr^2, which gives $\partial(nr^2)/\partial v = 0$.

In Figure A1 we plot nr^2 versus r for He^{2+} ions (a) and O^{5+} ions (b) based on an extended f_0. Clearly, this quantity is approximately constant over the radial distance considered. Thus, the numerical calculation also yields conservation of number flux.

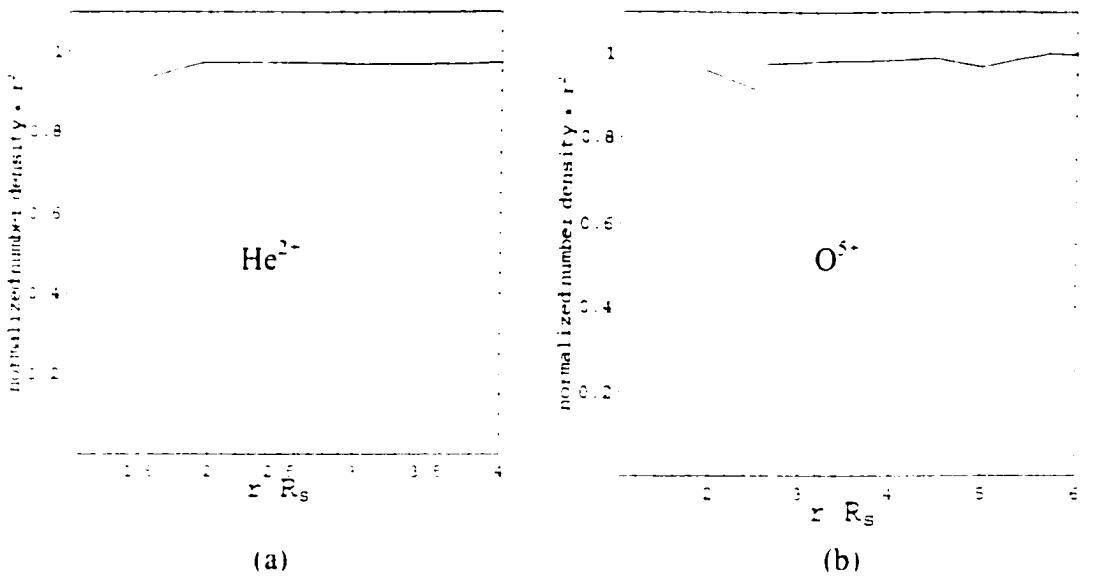

Figure A1. Depiction of approximately constant number density flux versus r. (a) He^{2+}, (b) O^{5+}

A.2 Structure of $f_0(v, x)$ for a Delta Function f_0

$$x_0 < \tfrac{1}{2}$$

The structure of $f_0(v, x)$ for protons is shown in Figure A2 for V_{sw} = 200 km/s and V_A = 500 km/s. This value of V_A is lower than a realistic value of V_A near $2R_s$ by a factor of at least 3, but this set of parameters allows clear differentiation of the various regions of the (x, v) solution space for reasons discussed below.

In the (x, v) solution space, the delta function shell is represented by a single characteristic curve specified by $A_0 = 1 - x_0$ and labeled as line 2 in Figure A2 (for protons $A_0 = 1$). Equation (20) yields the equation of line 2:

$$v_2(x) = A_0(1 - x)^{-1}. \qquad \text{(A2)}$$

For $x_0 < \frac{1}{2}$, the ion distribution is singular until the large-scale forces increase the wave frame energy of that shell to a value corresponding to $x = \frac{1}{2}$. Thereafter, ions are continually extracted at the − - boundary at $(x' > \frac{1}{2}, r_2)$, circulate through the (+) domain, return to the − - boundary at $(x'' < \frac{1}{2}, r_1 > r_2)$, and pitch-angle scatter along a continuous distribution of shells represented by regions I and II in Figure A2. Region I is bounded on the left by line 1, region II is bounded on the right by line 2, and the line $x = \frac{1}{2}$ separates the two regions. Equations (10b), (13), (17b), and (20) combine to yield the equation of line 1:

$$y_1(x) = A_1 (1 - x)^{q(1-Q)/(1+qQ)} x^{-(1+q)/(1+qQ)} . \qquad \text{(A3)}$$

As U_4 increases, the slope of line 1 at a given point increases; and for a given range of y, the width of Region I decreases. Therefore, to create a clearly discernible Region I, we plot Figure A2 with a relatively low value of U_4. Based on the definition of x in equation (17a) the lowest (highest) wave-frame energy of the distribution at a particular y is represented by x_1 (x_2), where x_2 and x_1 are given by equations (28a) and (28b). Thus, $f_-(y, x < x_1) = 0$ and $f_-(y, x > x_2) = 0$.

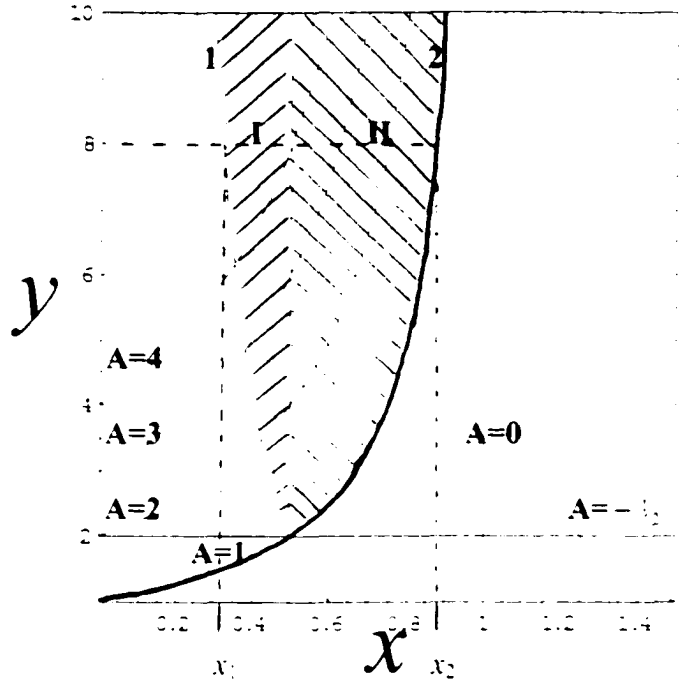

Figure A2. Structure of $f_{-}(y, x)$ for protons for a delta function f_0. V_M = 500 km s, and V_{sw} = 200 km s.

The radial distance at which the delta function shell achieves $x = \frac{1}{2}$ is determined from equation (28a) and given by $r_{x=1/2} = [2(1 - x_0)]^{2/(\gamma-2)} r_0$. As ion mass/charge increases, x_0 increases and the radial distance where ions first focus forward into the (+) domain decreases. Hence, heavy ion bulk speeds exceed proton bulk speeds at radial positions that decrease as ion mass/charge increases. Clearly, along line 2 as $y \to \infty, x_2 \to 1$; therefore, for $x_0 < \frac{1}{2}$, ions cannot free-escape the effective gravity.

In region I, not on line 1, $f_{-}(y, x)$ is obtained by solving equation (26) numerically, where the numerical method is described below. In region II, f_{-} is constant on characteristics, so $f_{-}(y, x > \frac{1}{2}) = f_{-}(y = 2A, x = \frac{1}{2})$. On line 2 we may write $f_{-} = N y^2 (y - A'')^{-1} \delta(A'' - A_0)$, where $N = n_0 r_0^2 (v_{ph} - V_M)^2 / 2\pi v_{ph} (\alpha GM)^2$ is

constant and has units $s^3 cm^{-6}$. We require $f_-(v,x)$ on line 1. Since $f_-(v,x)$ is finite at all other x and v, we may set the first term in equation (26) to zero. With f_- set to a delta function within the integrand in equation (26), $f_-(A)$ is then a step function at the intersection of line 1 and the characteristic curve specified by A. From the argument of f_- within the integrand in equation (26) and using equation (20) we find $A'' = A(v'' A^{-1} - 1)^{-(q+1)/(1+q)}$. Transforming the delta function from A to v and performing the integration yields

$$f_-(A(v,x)) = A_1^{-1}(1+qQ)(1+q)^{-1}[1-(A_1 A)^{(1+q)Q/(1+qQ)}][1+(A_1 A)^{(1+q)Q/(1+qQ)}]^{-1}, \quad \text{(A4)}$$

where, since we eventually normalize all values of f_- to the maximum value calculated, we drop the constant N. Equation (A4) determines the value of $f_-(v,x)$ on line 1 at the intersection point of line 1 and the characteristic curve specified by A.

Characteristic curves asymptotically approach $x = 1$; therefore, $x = 1$ is analogous to the pileup shell in velocity space described in chapter 2.3 and in *Isenberg* [2001a] and *Isenberg et al.* [2000, 2001].

Figures A2 and A3 show the connection between the structure of the ion velocity distribution in (x,v) space and in (v',x) space. Figure A2 shows the structure of only f_-, but over a range of r, whereas Figure A3 shows the entire distribution at only one value of r. In both figures, V_A = 500 km/s and V_{sw} = 200 km/s. Figure A3 is plotted when $r \approx 5.28 r_0$, which, for this set of parameters corresponds to $v = 8$ in Figure A2. The values of x_1 in both figures are equal as are the values of x_2. Curve 2 in Figure A2 corresponds to curve 2 in Figure A3; likewise for curve 1.

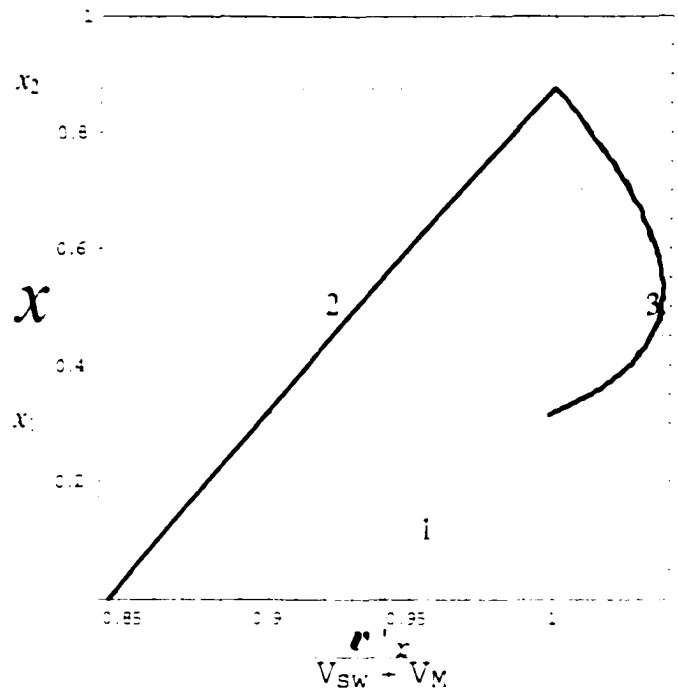

Figure A3 The connection between the structure of f in (x, v) space and the structure of f in (v', x) space may be made by comparing this figure with Figure A2. This figure is similar to Figure 2.6, but uses the same parameters as Figure A2. Here, $r = 5.28r_0$, which corresponds to $y = 8$ for this set of parameters.

$$\tfrac{1}{2} < x_0 < 1$$

The structure of $f_(v, x)$ for He^{2+} and $x_0 \approx 0.82$ is shown in Figure A4 (same parameters as Figure 2.12). Again, for all (x, v) to the left of line 1 and to the right of line 2, $f_(v, x) = 0$. Now, $f_(v, x) = 0$ in the interior region bounded by line 1, line 2 and the characteristic curve specified by A', but $f_$ is a step function at line 1 and A', and singular on line 2. The continuous distribution of $f_(v, x)$ is nonzero only in the shaded region bounded by line 1 on the left and the characteristic curve specified by A' on the right. The gap between the continuous distribution and the delta function shell (curve 2) decreases as y increases. This gap corresponds to the gap between curves 2 and 4 shown

in Figures 2.12c and d. In Figure 2.12c, for curve 4, $x = 1/2$ when $r/r_0 = 6.3$, which corresponds to $y = 16.9$ for these parameters and He^{2+}. The curve labeled by A' crosses $x = 1/2$ at $y \approx 16.9$.

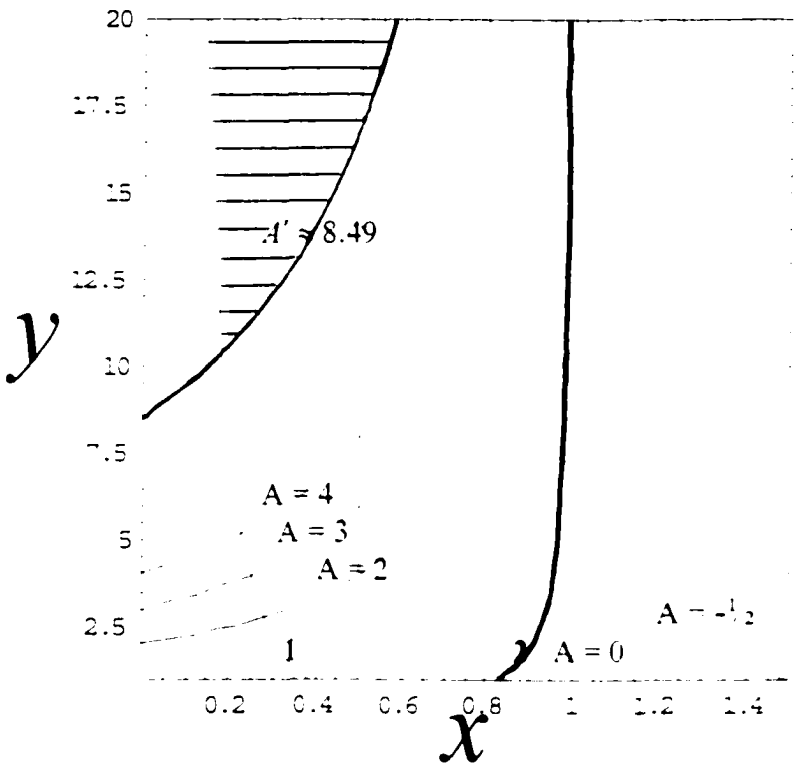

Figure A4. Structure of $f_-(v, x)$ for He^{2+}, $x_0 \approx 0.82$. f_- is singular on line 2, continuous in the shaded region and zero elsewhere.

$$x_0 > 1$$

The structure of $f_-(v, x)$ for He^{2+} and $x_0 \approx 3.28$ is shown in Figure A5 ($V_A = 1500\,km/s$ and $V_m = 150\,km/s$). Now, f_- is singular on line 2 and zero elsewhere. There is no line 1 in this case because ions do not return to the (-) domain, they freely escape the effective gravity. Line 2 asymptotically approaches $x = 1$ as $r \to \infty$, as does curve 2 in Figure 2.13.

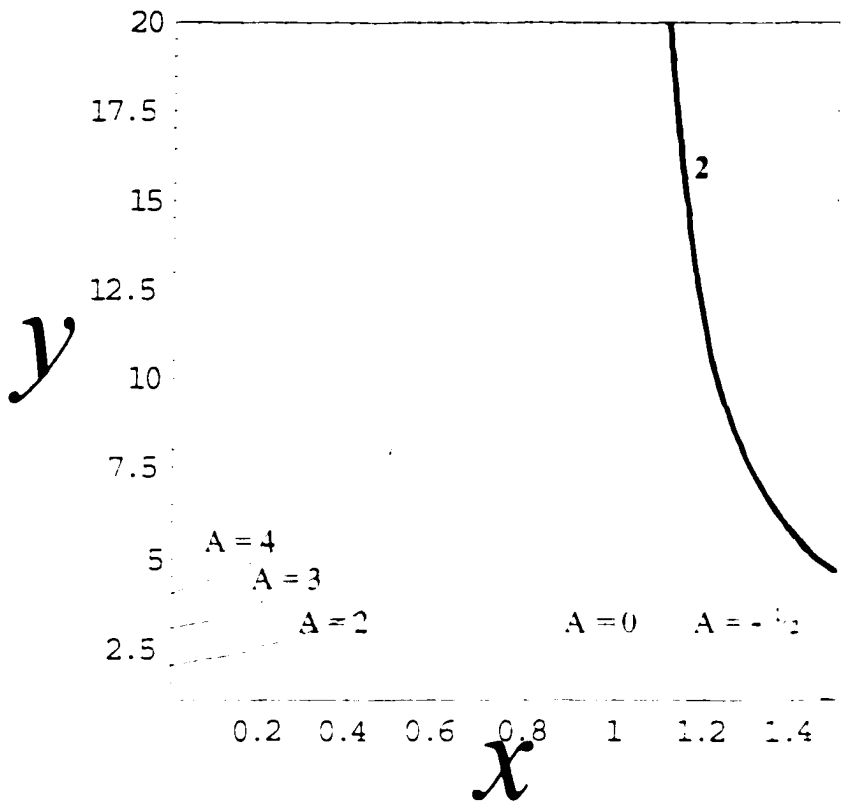

Figure A5. Structure of $f_{-}(y, x)$ for He^{2+}, $x_s \approx 3.28$. f_{-} is singular on line 2 and zero elsewhere.

A.3 Structure of $f_{-}(y, x)$ for an Extended f_0

The structure of $f_{-}(y, x)$ resulting from the use of an extended f_0 is quantitatively different from that of the delta function f_0. We show in Figure A6 the structure of $f_{-}(y, x)$ for protons with V_{SW} = 200 km/s, and V_A = 500 km/s. The characteristic curve specified by $A = \frac{1}{2}$ forms the left boundary of region III, in which $x > \frac{1}{2}$ at all y, therefore the solution for f_{-} in region III along characteristic curves specified by A is the function of A that satisfies the boundary condition. At $y = 1$, from equation (20) $A = 1 - x$, so $f_{-}(1, x)$

$= f_0(x) = f_0(1 - A)$; therefore, for any y in region III, $f\_(y, x) = f_0[1 - y(1 - x)]$. Hence, $f\_(y, x)$ is completely specified in region III.

Line 0 forms the right boundary of region VI and maps from the axis $y = 1$ according to equation (25a). We set $y' = 1$ and $y'' = y$ in equation (25a) and eliminate A with equation (20) to yield

$$y_0(x) = \left((1-x)\ \ x\right)^{q(1-Q)/(1-qQ)}. \tag{A5}$$

All points in region VI map according to equation (25a) for $y' < 1$. Hence, in region VI, $f\_$ within the integrand in equation (26) is always evaluated at $y' < 1$, and is thus equal to zero; therefore, the only contribution to $f\_(y, x)$ left of line 0 comes from the first term in equation (26), which is proportional to $f_0(1 - A)$. Since necessarily $x \geq 0$, $f_0(1 - A) = 0$ if $A > 1$. Therefore, in region VI, $f\_(y, x) = 0$, and in region IV $f\_(y, x)$ is determined solely by the first term in equation (26).

Region V is bounded by curves 0 and 1, where now line 1 is given by equation (A3) with $A_0 = \frac{1}{2}$. Since line 0 maps from the axis $y = 1$ and line 1 maps from the characteristic curve specified by $A = \frac{1}{2}$, region V is the analytical mapping from region III for $x < 1$. Therefore, $f\_$ in the integrand of equation (26) for region V is given by $f_0\left(y = y''\left(y''A^{-1} - 1\right)^{\frac{q(1-Q)}{1-qQ}}, x = Ay''^{-1}\right)$, where, in the argument of f_0, the expressions for y and x follow from equations (25a) and (25b). Since the functional form of f_0 is specified, the integral in equation (26) for region V may be evaluated. In region I, equation (26) is an integral equation for $f\_(y, x)$ which may be solved with the numerical solution method

described below. In region II, $f\_$ is constant along characteristic curves specified by A and is equal to $f\_(y = 2A, x = ½)$; thus, the solution for $f\_$ requires a numerical computation only in region I.

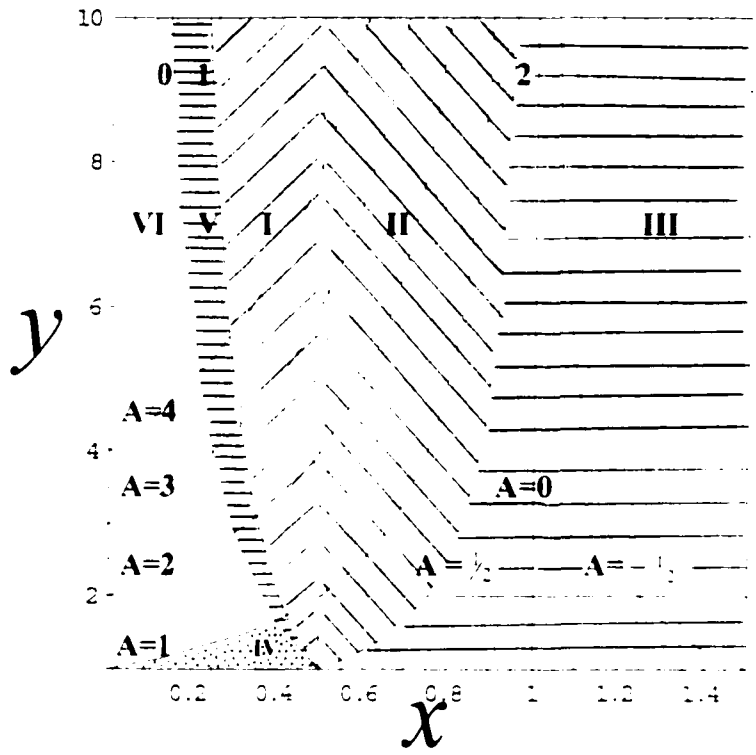

Figure A6. Structure of $f\_(y, x)$ for protons for an extended f_0.

A.4 Numerical Solution Method

We determine $f\_$ at discrete values of y and x in region I of Figure A2, A4 or A6 by approximating the integral in equation (26) by a finite sum. Inspection of the argument of $f\_$ within the integrand of equation (26) reveals that $f\_(y, x)$ depends on values of $f\_(y' < y, x' = 1 - x)$. This fact will be exploited to construct the solution for $f\_(y, x)$ from a small, initial set of values of $f\_$ determined as described below. The

calculation of this initial set begins near the intersection of lines 1 and 2 and is executed along an initial characteristic curve specified by A_1. The value of A_1 is chosen to be very close to A_0; thus, the initial integration path in region I (which ends when $x = x_2$) is vanishingly small as $A_1 \rightarrow A_0$. The initial value of f_- on characteristic curve A_1 is given by equation (A4), and is used to begin the calculation. Once this initial set is known, values of f_- along an adjacent characteristic $A > A_1$ may be calculated from the discrete version of equation (26). If values of $f_-(v', x')$ are required but not known precisely, an interpolation is performed to provide the best number for the summation. This process is repeated at continually increasing values of A, with the first value on each characteristic computed from equation (A4), until a preset value of v is reached.

A similar method is used to calculate $f_-(v, x)$ when $f_0(x)$ is an extended function of x. A numerical solution for $f_-(v, x)$ is required only in region I of Figure A6 since $f_-(v, x)$ may be calculated exactly in region V; therefore, $f_-(v, x)$ on line 1 is known exactly. The solution process then proceeds as previously described. Once a complete data set of values of $f_-(v, x)$ is known, $f_-(v', v_-)$ may be determined using the definition of x given in equation (17a).

LIST OF REFERENCES FOR PART I

Armstrong, T. P., S. M. Krimigis, K. H. Behannon, Proton fluxes at 300 keV associated with propagating interplanetary shock waves, *J. Geophys., Res.*, 75, 5980, 1970.

Asbridge, J. R., S. J. Bame, I. B. Strong, Outward flow of protons from the Earth's bow shock, *J. Geophys. Res.*, 73, 5777, 1968.

Axford, W. I., E. Leer, G. Skadron, The acceleration of cosmic rays by shock waves, *Proc. Int. Conf. Cosmic Rays 15th*, 11, 132, 1977.

Bame, S. J., J. R. Asbridge, W. C. Feldman, J. T. Gosling, G. Paschmann, N. Sckopke, Deceleration of the solar wind upstream from the Earth's bow shock and the origin of diffuse upstream ions, *J. Geophys. Res.*, 85, 2981, 1980.

Barnes, A., Collisionless damping of hydromagnetic waves, *Phys. Fluids*, 9, 1483, 1966.

Barnes, A., Theory of generation of bow-shock-associated hydromagnetic waves in the upstream interplanetary medium, *Cosmic Electrodyn*, 1, 90, 1970.

Bell, A. R., The acceleration of cosmic rays in shock fronts, *Mon. Not. R. Astron. Soc.*, 182, 147, 1978.

Blandford, R. D., and J. P. Ostriker, Particle acceleration by astrophysical shocks, *Astrophys. J.*, 221, L29, 1978.

Claßen, H.-T., G. Mann, Motion of ions reflected off quasi-parallel shock waves in the presence of large-amplitude magnetic field fluctuations, *Astronomy and Astrophysics*, 330, 381, 1998.

Dubouloz, N., and M. Scholer, On the origin of short large-amplitude magnetic structures upstream of quasi-parallel collisionless shocks, *Geophys. Res. Lett.*, 20, 547, 1993.

Earl, J. A., The diffusive idealization of charged particle transport in random magnetic fields, *Astrophys. J.*, 193, 231, 1974.

Fairfield, D. H., Bowshock associated waves observed in the far upstream interplanetary medium, *J. Geophys., Res.*, 74, 14, 3541, 1969.

Fairfield, D. H., Average locations of the Earth's magnetopause and bowshock, *J. Geophys. Res.*, 76, 6700, 1971.

Fisk, L., Increases in the low-energy cosmic ray intensity at the front of propagating interplanetary shocks, *J. Geophys. Res.*, 76, 7, 1662, 1971.

Fisk, L., and M. A. Lee, Shock acceleration of energetic particles in corotating interaction regions in the solar wind, *Astrophys. J.*, 237, 620, 1980.

Gary, S. P., J. T. Gosling, and D. W. Forslund, The electromagnetic ion beam instability upstream of the Earth's bow shock, *J. Geophys. Res.*, 86, 6691, 1981.

Goldstein, M. L., A non-linear theory of cosmic-ray pitch-angle diffusion in homogeneous magnetostatic turbulence, *Astrophys. J.*, 204, 900, 1976.

Gosling, J. T., J. R. Asbridge, S. J. Bame, W. C. Feldman, R. D. Zwickl, G. Paschmann, N. Sckopke, R. J. Hynds, Interplanetary ions during an energetic storm particle event: The distribution function from solar wind thermal energies to 1.6 MeV, *J. Geophys. Res.*, 86, 547, 1981.

Greenstadt, E. W., I. M. Green, G. T. Inouye, A. J. Hundhausen, S. J. Bame, I. B. Strong, Correlated magnetic field and plasma observations of the Earth's bow shock, *J. Geophys. Res.*, 73, 1, 1968.

Hada, T., C. F. Kennel, T. Terasawa, Excitation of compressible waves and the formation of shocklets in the Earth's foreshock, *J. Geophys. Res.*, 92, 4423, 1987.

Hoppe, M. et al. Upstream hydromagnetic waves and their association with backstreaming ion populations: ISEE 1 and 2 observations, *J. Geophys. Res.*, 86, 4471, 1981.

Ipavich, F. M., G. Gloeckler, C. Y. Fan, L. A. Fisk, D. Hovestadet, B. Klecker, J. J. O'Gallagher, and M. Scholer, Initial observation of low energy charged particles near the Earth's bow shock on ISEE 1, *Space Sci. Rev.*, 23, 93, 1979.

Ipavich, F. M., A. B. Galvin, G. Gloeckler, M. Scholer, and D. Hovestadt, A statistical survey of ions observed upstream of the Earth's bow shock: Energy spectra, composition, and spatial variation, *J. Geophys. Res.*, 86, 4337, 1981.

Jokipii, J. R., Propagation of cosmic rays in the solar wind, *Rev. Geophys. Space Phys.*, 9, 27, 1971.

Jones, F. C., T. B. Kaiser, T. J. Birmingham, New approach to cosmic ray diffusion theory, *Phys. Rev. Lett.*, 31, 485, 1973.

Jones, F. C., and D. C. Ellison, The plasma physics of shock acceleration, *Space Sci. Reviews*, 58, 259, 1991.

Kennel, C. F., et al., Plasma and energetic particle structure upstream of a quasi-parallel interplanetary shock, *J. Geophys. Res.*, 89, 5419, 1984.

Kennel, C. F., F. W. Coroniti, F. L. Scarf, W. A. Livesey, C. T. Russell, E. J. Smith, K. P. Wentzel, M. Scholer, A test of Lee's quasi-linear theory of Ion acceleration by interplanetary traveling shocks, *J. Geophys. Res.*, 91, 11917, 1986.

Krymsky, G. F., *Dokl. Akad. Nauk, SSSR*, 243, 1306, 1977.

Lee, M. A., Self-consistent kinetic equations and the evolution of a relativistic plasma in an ambient magnetic field, *Plasma Phys.*, 13, 1079, 1971.

Lee, M. A., H. J. Völk, Damping and non-linear wave-particle interactions of Alfvén waves in the solar wind, *Astro. and Space Sci.*, 24, 31, 1973.

Lee, M. A., Coupled hydromagnetic wave excitation and ion acceleration upstream of the Earth's bow shock, *J. Geophys. Res.*, 87, 5063, 1982.

Lee, M. A., Coupled hydromagnetic wave excitation and ion acceleration at interplanetary traveling shocks, *J. Geophys. Res.*, 88, 6109, 1983.

Lee, M. A., and H. J. Völk, Damping and non-linear wave-particle interactions of Alfvén waves in the solar wind, *Astron. Space Sci.*, 24, 31, 1973.

Lühr, H., N. Klöcker, W. Oelschlägel, B. Häusler, M. Acuna, The IRM fluxgate magnetometer, *IEEE Trans. Geosci. Remote Sens.*, GE-23(3), 259, 1985.

Mann, G., and H. Luhr, On short large amplitude magnetic structures in the vicinity of the quasi-parallel region of the Earth's bow shock, in *Sudy of the Solar-Terrestrial System*, compiled by J. J. Hunt, pp. 12-90, 91, Eur. Space Agency, Paris, 1992.

Matthaeus, W. H. and M. L. Goldstein, Measurement of the rugged invariants of MHD turbulence in the solar wind, *J. Geophys. Res.*, 87, 6011, 1982.

McKenzie and Völk, Nonlinear theory of cosmic ray shocks including self-generated Alfvén waves, *Astronomy and Astrophysics*, 116, 191, 1982.

Möbius, E., et al., The distribution function of diffuse ions and the magnetic field power spectrum upstream of Earth's bow shock, *Geophys. Res. Lett.*, 14, 681, 1987.

Parker, E. N., The passage of energetic charged particles through interplanetary space, *Planet. Space Sci.*, 13, 9, 1965.

Priest, E. R., Solar magnetohydrodynamics, *D. Reidel Pub. Co.*, 1982.

Sanderson, T. R., R. Reinhard, K. P., Wenzel, E. C. Roelof, E. J. Smith, Observations of upstream ions and low frequency waves on ISEE 3, *J. Geophys. Res.*, 88, 85, 1983.

Sarris, E. T. and J. A. Van Allen, Effects of interplanetary shock waves on energetic charged particles, *J. Geophys. Res.*, 79, 4157, 1974.

Scholer, M., and D. Burgess, The role of upstream waves in supercritical quasi-parallel shock re-formation, *J. Geophys. Res.*, 97, 8319, 1992.

Scholer, M. and G. Morfill, Simulation of solar flare particle interaction with interplanetary shock waves, *Sol. Phys.*, 45, 227, 1975.

Scholer, M., F. M. Ipavich, G. Gloeckler, D. Hovestadt, Acceleration of low-energy protons and alpha particles at interplanetary shock waves, *J. Geophys. Res.*, 88, 1977, 1983.

Scholer, M., K. J. Trattner, and H. Kucharek, Ion injection and Fermi acceleration at Earth's bow shock-The 1984 September 12 event revisited, *Astrophys. J.*, 395, 675, 1992.

Scholer, M., M. Fujimoto, H. Kucharek, Two-dimensional simulations of supercritical quasi-parallel shocks: upstream waves, downstream waves, and shock re-formation, *J. Geophys. Res.*, 98, 18971, 1993.

Schwartz, S. J., D. Burgess, W. P. Wilkinson, R. L. Kessel, M. Dunlop, H. Lühr, *J. Geophys. Res.*, 97, 4209, 1992.

Skilling, J., Cosmic ray streaming, III, *Mon. Not. R. Astron. Soc.*, 173, 255, 1975.

Smith, C. and M. A. Lee, Coupled hydromagnetic wave excitation and ion acceleration upstream of the Jovian bow shock, *J. Geophys. Res.*, 91, 81, 1986.

Sonnerup, B. U. Ö., Acceleration of particles reflected at a shock front, *J. Geophys. Res.*, 74, 1301, 1969.

Spangler, S., S. Fuselier, A. Fey, G. Anderson, An observational study of mhd wave-induced density fluctuations upstream of the Earth's bow shock, *J. Geophys. Res.*, 93, 845, 1988.

Tan, L. C., G. M. Mason, F. M. Ipavich, G. Gloeckler, R. D. Zwickl, S. J. Bame, Energetic proton and helium fluxes associated with interplanetary shocks and their relation to the solar wind composition, *J. Geophys. Res.*, 91, 11009, 1986.

Tan, L. C., G. M. Mason, G. Gloeckler, F. M. Ipavich, Energetic particle diffusion coefficients upstream of quasi-parallel interplanetary shocks, *J. Geophys. Res.*, 94, 6552, 1989.

Trattner, K. J., E. Möbius, M. Scholer, B. Klecker, M. Hilchenbach, H. Lühr, Statistical analysis of diffuse ion events upstream of Earth's bow shock, *J. Geophys. Res.*, 99, 13389, 1994.

Tsurutani, B. T., E. J. Smith, K. R. Pyle, J. A. Simpson, Energetic protons accelerated at corotating shocks: pioneer 10 and 11 observations fro 1 to 6 AU., *J. Geophys. Res.*, 87, 7389, 1982.

Tsurutani, B. T., E. J. Smith, D. E. Jones, Waves observed upstream of interplanetary shocks, *J. Geophys. Res.*, 88, 5645, 1983.

Tu, C. Y., E. Marsch, A case-study of very low cross-helicity fluctuations in the solar wind, *Ann. Geophys.*, 9, 5, 319, 1991

Völk, H. J. Non-linear perturbation theory for cosmic ray propagation in random magnetic fields, *Astrophys. Space Sci.*, 25, 471, 1973.

LIST OF REFERENCES FOR PART II

Antonucci, E., M. A. Dodero, and S. Giordano, Fast solar wind velocity in a polar coronal hole during solar minimum, *Solar Phys.*, 197, 115, 2000.

Astudillo, H. F., S. Livi, E. Marsch, and H. Rosenbauer, Evidence for nongyrotropic alpha particle and proton distribution functions: TAUS solar wind measurements, *J. Geophys. Res.* 101, 24423, 1996.

Axford, W. I., and J. F. McKenzie, The origin of high speed solar wind streams, in *Solar Wind Seven*, edited by E. Marsch, and R. Schwenn, pp. 1, Pergamon Press, Oxford, 1992.

Axford, W. I., and J. F. McKenzie, The acceleration of the solar wind, in *Solar Wind Eight*, edited by D. Winterhalter, D. McComas, J. Phillips, and N. Murphy, pp. 72, AIP, New York, 1996.

Bird, M. K., H. Volland, A. I. Efimov, G. S. Levy, B. L. Seidel, and C. T. Stelzried, Coronal Alfvén waves detected by radio sounding during the solar occultations of the Helios spacecraft, *SW 7: Proceedings of the 3rd COSPAR Colloquium*, 47, 1991.

Bochsler, P., J. Geiss, and R. Joos, Kinetic temperatures of heavy ions in the solar wind, *J. Geophys. Res.*, 90, 10779, 1985.

Cranmer, S. R., Ion cyclotron wave dissipation in the solar corona: the summed effect of more than 2000 ion species, *Astrophys J.*, 532, 1197, 2000.

Cranmer, S. R., Ion cyclotron diffusion of velocity distributions in the extended solar corona, *J. Geophys. Res.*, 106, 24937, 2001.

Cranmer, S. R.; G. R. Field; G. Noci; and J. L. Kohl., The impact of ion-cyclotron wave dissipation on minor ion velocity distributions in the solar corona, *AAS*, 191, 7411, 1997.

Cranmer, S.R., G. B. Field, G. Noci, and J. L. Kohl, Acceleration and heating of the fast solar wind: diagnostics and theory, *EOS trans. AGU*, 79(17) *Spring meeting suppl.*, S278, 1998.

Cranmer, S. R., G. B. Field, and J. L. Kohl, The impact of ion-cyclotron wave dissipation on heating and accelerating the fast solar wind, *CP471 solar wind nine*, 35, 1999a.

Cranmer, S. R., G. B. Field, and J. L. Kohl, Spectroscopic constraints on models of ion cyclotron resonance heating in the polar solar corona and high-speed solar wind, *Astrophys J.*, 518, 937, 1999b.

Cranmer, S. R. et al., New diagnostics of coronal heating and solar wind acceleration processes achievable with the advanced solar coronal explorer (ASCE), *Amer. Astron. Soc. SPD meeting* #32, #02.97 2000SPD....23.0297C, 2000a.

Cranmer, S. R. and J. L. Kohl, Surf's still up: UVCS/SOHO observations as strong constraints on coronal heating theories, *Amer. Astron. Soc. SPD meeting* #32, #15.02 2000SPD..... 23, 1502, 2000b.

Cranmer, S. R., S. R. Spangler, R. Esser, and J. L. Kohl, Coronal holes and the high-speed solar wind, *Space Sci. Rev.*, in press, 2002.

Czechowski, A.; R. Ratkiewicz, J. F. McKenzie, and W. I. Axford, Heating and acceleration of minor ions in the solar wind, *Astron. and Astrophys.*, 335, 303, 1998.

Demars, H. G., and R. W. Schunk, Solar wind proton velocity distributions: comparison of the bi-maxwellian based 16-moment expansion with observations, *Planet. Space Sci.*, 38, 1091, 1990.

Dmitruk, P., L. J. Milano, and W. H. Matthaeus, Wave-driven turbulent coronal heating in open field line regions: nonlinear phenomenological model, *Astrophys. J.*, 548, 482, 2001.

Dodero, M. A., E. Antonucci, S. Giordano, and R. Martin, Solar wind velocity and anisotropic coronal kinetic temperature measured with the O VI doublet ratio, *Solar Phys.*, 183, 77, 1998.

Dusenbery, P. B. and J. V. Hollweg, Ion-cyclotron heating and acceleration of solar wind minor ions, *J. Geophys., Res.*, 86, 153, 1981.

Esser, R., T. E. Holzer, and E. Leer, Drawing inferences about solar wind acceleration from coronal minor ion observations, *J. Geophys. Res.*, 92, 13377, 1987.

Esser, R., R. J. Edgar, and N. S. Brickhouse, High minor ion outflow speeds in the inner corona and observed ion charge states in interplanetary space, *Astrophys. J.*, 498, 448, 1998.

Esser, R., et al., Plasma properties in coronal holes derived from measurements of minor ion spectral lines and polarized white light intensity, *Astrophys. J.*, 510, L63, 1999.

Esser, R. and R. J. Edgar, Non-Maxwellian electron distributions and differential flow speeds between same element ions: effects on solar wind ion fractions *AGU SM*, SH41B-20, 2001.

Feldman, W. C., J. R. Asbridge, S. J. Bame, and M. D. Montgomery, Double ion streams in the solar wind, *J. Geophys. Res.*, 78, 2017, 1973.

Feldman, W. C., J. T. Gosling, D. J. McComas, and J. L. Phillips, Evidence for ion jets in the high speed solar wind, *J. Geophys. Res.*, 98, 5593, 1993.

Feldman, W. C., S. R. Habbal, G. Hoogeveen, and Y.-M. Wang, Experimental constraints on pulsed and steady-state models of the solar wind near the sun, *J. Geophys. Res.*, 102, 26905, 1997.

Gendrin, R. A. Roux, Energization of helium ions by proton-induced hydromagnetic waves, *J. Geophys. Res.*, 85, 4577, 1980.

Goldstein, B. E., A review of solar wind ion and electron plasma distributions: present understanding and Ulysses results, CP382, *solar wind 8*, 204, 1996.

Goldstein, B. E., M. Neugebauer, and E. J. Smith, Alfvén waves, alpha particles, and pickup ions in the solar wind, *Geophys. Res. Let.*, 22, 3389, 1995.

Goldstein, B. E. and M. Neugebauer, Velocity space distributions of protons and alpha particles in high speed solar wind, *AGU SM*, *SH42B*-09, 2001.

Gomberoff, L. and R. Elgueta, Resonant acceleration of alpha particles by ion cyclotron waves in the solar wind, *J. Geophys. Res.*, 96, 9801, 1991.

Gomberoff, L. and R. Hernandez, On the acceleration of alpha particles in the fast solar wind, *J. Geophys. Res.*, 97, 12113, 1992.

Gomberoff, L., R. Hernandez, and S. Livi, High energy tail formation due to right-hand polarized ion cyclotron waves, *P&SS*, 43, 1101, 1995.

Gomberoff, L., F. T. Gratton, and G. Gnavi, Acceleration and heating of heavy ions by circularly polarized Alfvén waves, *J. Geophys. Res.*, 1011, 5661, 1996.

Hammond, C. M., W. C. Feldman, J. L. Phillips, B. E. Goldstein, and A. Balogh , Solar wind double ion beams and the heliospheric current sheet, *J. Geophys. Res.*, 100, 7881, 1995.

Harmon, J. K., W. A. Coles, Radio scattering signature of high-frequency Alfvén (ion cyclotron) waves in the inner solar wind, *AGU FM*, *SH*21A-0722, 2001.

Hollweg, J., V., Transition region, corona, and solar wind in coronal holes, *J. Geophys. Res.*, 91, 4111, 1986.

Hollweg, J. V., Potential wells, the cyclotron resonance, and ion heating in coronal holes, *J. Geophys. Res.*, 104, 505, 1999a.

Hollweg, J. V., The cyclotron resonance in coronal holes: 1. heating and acceleration of protons, O^{5+} and Mg^{9+}, J. Geophys. Res., 104, 24781, 1999b.

Hollweg, J. V., Cyclotron resonance in coronal holes 2. A two-proton description, *J. Geophys. Res.*, 104, 24793, 1999c.

Hollweg, J. V., The cyclotron resonance in coronal holes 3. A five-beam turbulence-driven model, *J. Geophys. Res.*, 1051, 5699, 2000.

Hollweg, J. V. and J. M. Turner, Effects of resonant and nonresonant interactions with transverse waves, *J. Geophys., Res.*, 83, 97, 1978.

Hollweg, J. V. and W. Johnson, Transition region, corona, and solar wind in coronal holes: some two-fluid models, *J. Geophys. Res.*, 93, 9547, 1988.

Hollweg, J. V. and S. A. Markovskii, Cyclotron resonances of ions with obliquely-propagating waves in coronal holes and the fast solar wind, *2001AGUSM SH22E05H*, 2001.

Hollweg, J. V., and P. A. Isenberg, Generation of the fast solar wind: A review with emphasis on the resonant cyclotron interaction, *J. Geophys. Res.*, in press, 2002.

Hu, Y. Q., S. R. Habbal, and X. Li, On the cascade processes of Alfvén waves in the fast solar wind, *J. Geophys. Res.*, 104, 24819, 1999.

Hu, Y. Q. and S. R. Habbal, Resonant acceleration and heating of solar wind ions by dispersive ion-cyclotron waves, *J. Geophys. Res.*, 104, 17045, 1999.

Hu, Y. Q., R. Esser, and S. R. Habbal, A four-fluid turbulence driven solar wind model for preferential acceleration and heating of heavy ions, *J. Geophys. Res.*, 105, 5093, 2000.

Isenberg, P. A., Resonant acceleration and heating of solar wind ions: anisotropy and dispersion, *J. Geophys. Res.*, 89, 6613, 1984.

Isenberg, P. A., Investigations of a turbulence-driven solar wind model, *J. Geophys. Res.*, 95, 6437, 1990.

Isenberg, P. A., A hemispherical model of anisotropic interstellar pickup ions, *J. Geophys. Res.*, 102, 4719, 1997.

Isenberg, P. A., Heating of coronal holes and generation of the solar wind by ion-cyclotron resonance, *space science reviews*, 95, 119, 2001a.

Isenberg, P.A., The kinetic shell model of coronal heating and acceleration by ion cyclotron waves: dispersive waves, *AGUFM SH42B-06*, 2001b.

Isenberg, P. A., The kinetic shell model of coronal heating and acceleration by ion cyclotron waves 2. Inward and outward propagating waves, *J. Geophys. Res.*, 106, 29249, 2001c.

Isenberg, P. A. and J. V. Hollweg, On the preferential acceleration and heating of solar wind heavy ions, *J. Geophys. Res.*, 88, 3923, 1983.

Isenberg, P. A. and M. A. Lee, A dispersive analysis of bi-spherical pickup ion distributions, *J. Geophys. Res.*, 101, 11055, 1996.

Isenberg, P. A., M. A. Lee, and J. V. Hollweg, A kinetic model of coronal heating and acceleration by ion-cyclotron waves: preliminary results, *solar physics*, 193, 247, 2000.

Isenberg, P. A., M. A. Lee, and J. V. Hollweg, The kinetic shell model of coronal heating and acceleration by ion-cyclotron waves. 1. Outward-propagating waves, *J. Geophys. Res.*, 106, 5649, 2001.

Kaghashvili, E. Kh., Ion-cyclotron wave dissipation channel for Alfvén waves, *Geo. Res. Let.*, 26, 1817, 1999.

Kennel, C. F. and F. Englemann, Velocity space diffusion from weak plasma turbulence in a magnetic field, *The Physics of Fluids*, 9, 2377, 1966.

Kohl, J. L., et al., Measurements of H I and O VI velocity distributions in the extended solar corona UVCS/SOHO and UVCS/Spartan 201, *AdSpR*, 20, 3, 1997.

Kohl, J. L., et al., UVCS/SOHO Empirical determinations of anisotropic velocity distributions in the solar corona, *Astrophys. J.*, 501, L127, 1998.

Kohl, J. L, et al., UVCS/SOHO observations of spectral line profiles in polar coronal holes, *Space Sci. Rev.*, 87, 233, 1999.

Kulsrud, R. M., MHD description of plasma, in *Basic Plasma Physics I*, edited by A. A. Galeev, and R. N. Sudan, p. 115 – 145, North-Holland, New Your, 1983.

Leamon, R. J., W. H. Matthaeus, C. W. Smith, and H. K. Wong, Contribution of cyclotron-resonant damping to kinetic dissipation of interplanetary turbulence. *Astrophys. J.*, 507, L181, 1998.

Livi, S., and E. Marsch, Generation of solar wind protons tails and double beams by coulomb collisions, *J. Geophys. Res.*, 92, 7255, 1987.

Li, X., S. R. Habbal, J. V. Hollweg, and R. Esser, Heating and cooling of protons by turbulence driven ion-cyclotron waves in the fast solar wind, *J. Geophys. Res.*, 104, 2521, 1999.

Li, X. and S. R. Habbal, Ion-cyclotron waves, instabilities and solar wind heating, *solar physics*, 190, 485, 1999.

Markovskii, S. A., Generation of ion-cyclotron waves in coronal holes by a global resonant MHD mode, *Astrophys. J.*, 557, 337, 2001.

Marsch, E., Radial evolution of ion distribution functions, *JPL solar wind 5 sowi.conf..355M (see N84-13067 03-92)*, 355, 1983.

Marsch, E., Velocity distributions of solar wind ions and electrons, *ESA Plasma Astrophysics (SEE N85-22270 12-90)*, 33, 1984.

Marsch, E., Cyclotron heating of the solar corona, *Astrophysics and Space Science*, 264, 63, 1998.

Marsch, E., Kinetic physics of the solar wind plasma, *Physics and Chemistry in space-space and solar physics. Physics of the inner heliosphere II Editors: R. Schwenn, E. Marsch*, 21,1991.

Marsch, E., H. Rosenbauer, R. Schwenn, K.-H. Muehlhaeuser, and K.U. Denskat, Pronounced proton core temperature anisotropy, ion differential speed, and simultaneous Alfvén wave activity in slow solar wind at 0.3 AU, *J. Geophys. Res.*, 86, 9199, 1981.

Marsch, K.-H. Mühlhäuser, R. Schwenn, H. Rosenbauer, W. Pilipp, and F. M. Neugebauer, Solar wind protons: Three-dimensional velocity distributions and derived plasma parameters measured between 0.3 and 1 AU, *J. Geophys. Res.*, 87, 52, 1982a.

Marsch, E., C. K. Goertz, and K. Richter, Wave heating and acceleration of solar wind ions by cyclotron resonance, *J. Geophys. Res.*, 87, 5030, 1982b.

Marsch, E. and H. Goldstein, The effects of coulomb collisions on solar wind ion velocity distributions, *J. Geophys. Res.*, 88, 9933, 1983.

Marsch, E. and S. Livi, Observational evidence for marginal stability of solar wind ion beams, *J. Geophys. Res.*, 92, 7263, 1987.

Marsch, E. and C.-Y. Tu, The effects of high-frequency Alfvén waves on coronal heating and solar wind acceleration, *Astron. and Astrophys.*, 319, L17, 1997.

Marsch, E. and C.-Y. Tu, Evidence for pitch angle diffusion of solar wind protons in resonance with cyclotron waves, *J. Geophys. Res.*, 106, 8357, 2001.

McKenzie, J. F., and W. I. Axford, The origin of the fast solar wind, *2001AGUSM SH22E04*, 2001.

McKenzie, J. F., and E. Marsch, Resonant wave acceleration of minor ions in the solar wind, *Astrophys. Space Sci.*, 81, 295, 1982.

Neugebauer, M., Observations of solar wind helium, *Fundam. Cosmic Phys.*, 7, 131, 1981.

Neugebauer, M., Knowledge of coronal heating and solar wind acceleration obtained from observations of the solar wind near 1 AU, in *Solar Wind Seven*, edited by E. Marsch, and R. Schwenn, pp69, Pergamon, Oxford, 1992.

Neugebauer, M., B. E. Goldstein, S. J. Bame, and W. C. Feldman, ULYSSES near-ecliptic observations of differential flow between protons and alphas in the solar wind, *J. Geophys. Res.*, 99, 2505, 1994.

Neugebauer, M., et al., Ulysses Observations of differential alpha-proton streaming in the solar wind, *J. Geophys. Res.*, 101, 17047, 1996.

Neugebauer, M., B. E. Goldstein, D. Winterhalter, E. J. Smith, R. J. MacDowall, and S. P. Gary, Ion distributions in large magnetic holes in the fast solar wind, *J. Geophys. Res.*, 106, 5635, 2001.

Ofman, L., A. Vinas, and S. P. Gary, Constraints on the O^{5+} anisotropy in the solar corona, *Astrophys. J.*, 547, L175, 2001.

Ogilvie, K. W., P. Bochsler, and J. Geiss, Observations of the velocity distributions of solar wind ions, *J. Geophys. Res.*, 85, 6069, 1980.

Ogilvie, K. W., J. Geiss, G. Gloeckler, D. Berdichevsky, and B. Wilken, High-Velocity tails on the velocity distribution of solar wind ions, *J. Geophys. Res.*, 98, 3605, 1993.

Reisenfeld, D. B., S. P. Gary, J. T. Gosling, J. T. Steinberg, D. J. McComas, B. E. Goldstein, and M. Neugebauer, Helium energetics in the high-latitude solar wind: Ulysses observations, *J. Geophys. Res.*, 106, 5693, 2001.

Rosenbauer, H., E. Marsch, K. H. Mohlhauser, W. Pilipp, and R. Schwenn, Helios-indications of resonant wave-particle interaction in fast stream solar wind ion distributions, *solar wind 4*, 353, 1981.

Skilling, J., Cosmic rays in the galaxy: Convection or diffusion?, *Astrophys. J.*, 170, 265, 1971.

Ryan, J. M. and W. I. Axford, The behaviour of minor species in the solar wind, *J. Geophys.*, 41, 221, 1975.

Stix, T. H., *Waves in Plasmas*, p. 32, American Institute of Physics, New York, 1992.

Suleiman, R. M., et al., UVCS/SOHO observations of H I Lyman alpha line profiles in coronal holes at heliocentric heights about 3.0 solar radii, *Space Sci. Rev.*, 87, 327, 1999.

Tam, W. Y. and T. Chang, Global evolution of particle distributions in the solar wind including the effects of wave-particle interactions, *Comments of Modern Physics*, 1, 141, 1999.

Tanabe, J. T., J. C. Kasper, and A. J. Lazarus, Proton and alpha particle temperature anisotropies in the solar wind with the WIND/SWE Faraday cup, *AGU SM*, *SH*31*A*-11, 2001.

Tanaka, M., Simulations of heavy ion heating by electromagnetic ion cyclotron waves driven by proton temperature anisotropies, *J. Geophys. Res.*, 90, 6459, 1985.

Tu, C.-Y. and E. Marsch, Two-fluid model for heating of the solar corona and acceleration of the solar wind by high-frequency Alfvén waves, *solar physics*, 171, 363, 1997.

Tu, C.-Y. and E. Marsch, On cyclotron wave heating and acceleration of solar wind ions in the outer corona, *J. Geophys. Res.*, 106, 8233, 2001.

Ventura, R., S. Orlando, G. Peres, and D. Spadaro, Fast solar wind acceleration by Alfvén waves: observable effects on the EUV lines detected by SOHO/UVCS, *Astron. Astrophys.*, 352, 670, 1999.

Verma, M. K., D. A. Roberts, M. L. Goldstein, S. Ghosh, and W. T. Stribling, A numerical study of the nonlinear cascade of energy in magnetohydrodynamic turbulence, *J. Geophys. Res.*, 101, 21619, 1996.

Yoon, P. H. and L. F. Zibell, Development of Pitch angle anisotropy and velocity diffusion of pickup ion shell distribution by solar wind turbulence, *J. Geophys. Res.*, 95, 17085, 1990.